1 **Petrogenesis of Fe-Ti-P mineral deposits associated with Proterozoic anorthosite massifs**
2 **in the Grenville Province: insights from oxide and apatite trace-element geochemistry at**
3 **Lac à l'Orignal, Quebec, Canada**

7
8 **Pedro Miloski****

9 Département de Sciences Appliquées, Université du Québec à Chicoutimi (UQAC), 555 Boulevard de
10 l'Université, Chicoutimi, Québec, Canada, G7H 2B1

11 Corresponding author - E-mail: miloski.geo@gmail.com

12
13 Sarah Dare

14 Département de Sciences Appliquées, Université du Québec à Chicoutimi (UQAC), 555 Boulevard de
15 l'Université, Chicoutimi, Québec, Canada, G7H 2B1

16
17 Caroline-Emmanuelle Morisset

18 Agence spatiale canadienne, 6767 Rte de l'Aéroport, Saint-Hubert, Québec, Canada, J3Y 8Y9

19
20 Joshua H.F.L. Davies

21 Département des sciences de la Terre et de l'atmosphère/GEOTOP, Université du Québec à Montréal (UQAM),
22 405 Rue Sainte-Catherine Est, Montréal, Québec, Canada, H2L 2C4

23
24 Morgann G. Perrot

25 Département des sciences de la Terre et de l'atmosphère/GEOTOP, Université du Québec à Montréal (UQAM),
26 405 Rue Sainte-Catherine Est, Montréal, Québec, Canada, H2L 2C4

27
28 Dany Savard

29 Département de Sciences Appliquées/LabMaTer, Université du Québec à Chicoutimi (UQAC), 555 Boulevard de
30 l'Université, Chicoutimi, Québec, Canada, G7H 2B1

31
32 **Abstract**

33 Proterozoic anorthosite massifs can host significant amounts of critical and strategic metals, such as Ti, V and P,

34 associated with magmatic Fe-Ti oxides and apatite. Yet their petrogenesis is much less understood than Fe-Ti-V-

35 P deposits hosted in layered intrusions within large igneous provinces. Several mineralized lenses of Fe-Ti-P

36 outcrop near the border of the 1080 (±2) Ma Vanel and the 1016 (±2) Ma Mattawa anorthosite massifs, in the

37 Central Grenville Province, Quebec, Canada. For example, the Lac à l'Orignal Fe-Ti-P deposit, hosted in the

38 Vanel anorthosite near the northern border of the Mattawa anorthosite, comprises a lenticular structure of oxide

39 apatite norite (OAN) with thin layers of apatite-bearing anorthosite and minor amounts of nelsonite (massive Fe-

40 Ti oxides and apatite), indicating accumulation by density differences. Oxide settling generated the melanocratic

41 OAN cumulates and nelsonite. Plagioclase flotation generated the leucocratic apatite-bearing anorthosite layers.

42 The mineralization is dominated by hemo-ilmenite, accompanied by apatite and a minor amount of magnetite at

43 the borders, whereas the core is dominated by ilmenite, magnetite, and apatite. In-situ U-Pb dating of magmatic

44 zircon indicates that the Lac à l'Orignal deposit is a multi-stage intrusion with two different crystallization ages

45 between the younger core (993 ± 13 Ma) and the older upper border (1069 ± 12 Ma) of the intrusion. These ages

46 are similar to those of nearby anorthosite-massifs (Mattawa and Vanel anorthosites, respectively). In-situ trace

47 element analysis of plagioclase, apatite and oxides, by laser ablation ICP-MS, reveals subtle variations in certain

48 trace elements (e.g., Cr, Ni, V) related to differentiation under relatively high-fO_2 conditions (FMQ = +0.9 to

49 +1.7). Calculated melt compositions from apatite indicates a similar parental magma for both the border and core

50 that matches the composition of high-Fe-Ti-P ferrodiorite dykes at Lac à l'Original. This high-Ti-P ferrodiorite

51 magma was probably residual after anorthosite formation. Sub-solidus inter-oxide equilibration modified the

52 original composition of the different cumulates in the intrusion. The absence of extensive massive oxide cumulates

53 and the presence of higher amounts of cumulus magnetite and apatite, supported by mineral chemistry, denotes a

54 more evolved character for the Lac à l'Orignal deposit compared with other Fe-Ti-(P) deposits in the Grenville

55 Province (e.g., Lac Tio Fe-Ti and Grader intrusion Fe-Ti-P deposits in the Havre St. Pierre Anorthosite, eastern

56 Quebec). Petrogenetically, the Lac à l'Orignal Fe-Ti-P deposit corresponds to an evolved part of a low-Ti/Fe

57 system in the Grenville Province in the late stages of differentiation of ferrodiorite/jotunite magmas.

58 **Keywords:** Fe-Ti-P deposit; Massif-type Anorthosites; Grenville Province; Oxide-apatite geochemistry.

59 **Introduction**

60 Magmatic oxide-apatite (Fe-Ti-V-P) mineralization/deposits are spatially and temporally associated with

61 Proterozoic AMCG (Anorthosite – Mangerite – Charnockite - Granite) suites (Ashwal, 1993; Charlier et al. 2015).

62 They provide important resources for several critical and strategic elements, in particular Ti (from hemo-ilmenite:

63 Fe_2O_3-$FeTiO_3$), but also V (from magnetite: Fe_3O_4) and P (from apatite: $Ca_5(PO_4)_3(OH,F,Cl)$). For example, there

64 are only two currently active magmatic Ti mines in the world, both associated with massif-type anorthosites and

65 hemo-ilmenite-dominated mineralization: Lac Tio (Havre Saint Pierre Anorthosite, Quebec (Charlier et al. 2010)),

66 the world's largest producer of TiO_2; and Tellnes (Rogaland Anorthosite Province, Norway (Charlier et al. 2006)).

67 However, the origin of oxide-apatite mineralization and its genetic relationship to the anorthosite-host rocks are

68 still debated (Owens & Dymek, 1992; Dymek & Owens, 2001; Charlier et al. 2008). Oxide-apatite minerals can

69 form stratiform layers in layered mafic intrusions at the margins of massif-type anorthosites, such as the Bjerkrein

70 Sokndal Layered Intrusion, Norway (Wilson et al. 1996); Grader intrusion, Quebec (Charlier et al. 2008) and

71 Fedorivka Layered Intrusion, Ukraine (Duchesne et al. 2006). However, mineralized zones can also take the form

72 of lenses of massive oxides, such as Lac Tio, Quebec (Charlier et al. 2010), Saint Urbain, Quebec (Morisset et al.

73 2009) or nelsonite (oxide and apatite), such as at Damiao, China (Chen et al. 2013) within anorthosite. In some

74 cases, the lenses of oxides may have formed in a magma conduit cross cutting the anorthosite (Charlier et al.

75 2010). Finally, some deposits form by emplacement of sills containing ilmenite-plagioclase-(orthopyroxene)

76 cumulates, such as the Tellnes Ti deposit, Norway (Charlier et al. 2006, 2007) or as dykes/layers along or near

77 the outer boundaries of anorthosite massifs.

78 Anorthosite massifs were emplaced as diapiric intrusions of plagioclase-rich mushes into the middle-

79 crust, along major crustal shear zones, that formed after crystallization and sinking of ultramafic cumulates in

deep-seated magma chambers at or near the base of the continental crust (Ashwal, 1993; Bybee & Ashwal, 2015; Slagstad et al. 2022). Oxide-apatite mineralization is commonly interpreted as crystallizing from residual Fe-Ti-V-P rich melts (ferrodiorite/jotunite composition), after extensive polybaric crystallization of plagioclase and mafic silicates (e.g., olivine, orthopyroxene, clinopyroxene) during the formation of anorthosite massifs (Vander Auwera et al. 2006; Charlier et al. 2008; Ashwal 2010). However, a number of mechanisms have been proposed to concentrate the oxides (± apatite) into Fe-Ti(±P) deposits, such as fractional crystallization with oxide settling and plagioclase flotation (Charlier et al. 2006; 2007; 2008; 2015), filter pressing or draining of jotunite/ferrodiorite residual melts into tension fractures of margins of the massifs (Dymek & Owens, 2001 Vander Auwera et al. 2006; Scoates et al. 2010), magma mixing (Charlier et al. 2006; 2010; Namur et al. 2010) and/or liquid immiscibility (Philpotts, 1967; 1982; Charlier & Grove, 2012; Hou et al. 2018; Coint et al. 2020).

Previous studies on Fe-Ti-(P) mineral deposits worldwide, such as in the Bjerkrein-Sokndal in Norway (Charlier et al. 2005), Lac Tio (Charlier et al. 2010) and Grader (Charlier et al. 2008) in Canada, Fedorivka in Ukraine (Duchesne et al. 2006) and Damiao (Chen et al. 2013) in China, have successfully used the trace element composition of Fe-Ti oxides, apatite and silicates (where present) to investigate the role of magmatic processes (e.g. fractional crystallization, magma replenishments, parental magma composition) involved in the formation of these oxide-apatite deposits. Numerous Fe-Ti-P showings occur in the Central Province of the Grenville, including the world-class phosphate deposit of Lac à Paul. However, only a few publications have focused on the petrological aspects of oxide-apatite cumulate rocks for the Central Grenville Province (e.g., Owens & Dymek, 1992; Dymek & Owens, 2001; Morisset et al. 2010). In this paper, we present a detailed whole-rock and in-situ trace-element stratigraphical study of plagioclase, oxides, and apatite, as well as in-situ U-Pb dating of zircon, from oxide-apatite norite cumulates associated with the Lac à l'Orignal Fe-Ti-P deposit, in the Central Grenville Province, Quebec.

Based on drilling by Glen Eagle resources, the Lac à l'Orignal Fe-Ti-P mineralized zone has a E-W lenticular structure, approximately 10-100 m thick and 1.5 km in length (Fig.1e), with an average grade of 5.1 wt.% P_2O_5 (Fig.1d), locally up to 7 wt.% P_2O_5 (Laverdière, 2013; 2016). The deposit has recently been claimed by First Phosphate Corp., with a Mineral Resources Estimate (MRE) indicating 15.8 Mt at 5.18% P_2O_5, 4.23% TiO_2 and 23.90% Fe_2O_3, with inferred values of 33.2 Mt at 5.06% P_2O_5, 4.16% TiO_2 and 22.55% Fe_2O_3. (Yassa, 2022). Similar to the two hard-rock deposits in anorthosites presently exploited, the Lac Tio mine, Quebec (Charlier et al. 2008) and the Tellnes deposit, Norway (Charlier et al. 2006; 2007), the Lac à l'Orignal deposit is ilmenite-dominated with geochemical and mineralogical variation related to magma differentiation within a multi-stage mineralized body. The oxide-apatite rich rocks at Lac à l'Orignal thus constitute an important opportunity to study the Fe-Ti-P ore-forming processes and the controlling factors on ore composition (i.e., processes e.g., fractional crystallization; fO_2 conditions, subsolidus re-equilibration) in the Central Grenville Province.

Regional Geological Setting

The Grenville Province in Eastern Canada (Fig.1a) is a Mesoproterozoic orogenic belt that represents the southeastern margin of the Paleocontinent of Laurentia (Corriveau et al. 2007). The Paleo to Late Mesoproterozoic rocks of the Grenville Province represent an active continental margin with more than 400 m.y. of tectonic activity and extensive episodes of subduction-accretion and arc formation (Rivers, 1997). Subsequent stages of continent-

continent collision (Shawinigan, 1190 – 1140Ma; Ottawan, 1080 – 1020Ma and Rigolet, 1000 – 850Ma) took place during the Grenvillian Orogeny, separated by periods of crustal extension and several occurrences of within-plate magmatism. During this Himalayan-type event, crustal thickening and tectonic extrusion led to widespread high-grade metamorphism (Ludden and Hynes, 2000b) and reactivation of deep-level shear zones in the Grenville Province, such as the Saint Fulgence and Pipmuacan Deformation Zones in the Central Grenville (Fig.1b) (Corriveau et al. 2007).

The Grenville Province experienced numerous episodes of AMCG magmatism with coeval Fe-Ti-P mineralization, that occurred over 300 m.y. (1327 – 1000 Ma), recording a complex petrogenetic, tectonic and temporal evolution (Emslie, 1985; Higgins & Van Breemen, 1996; Gobeil et al. 2002; Hebert et al. 2005; 2009). The emplacement of most of the AMCG suites and other mafic magmas described in the Central Grenville Province are coeval with periods of either crustal shortening or crustal extension during the Grenvillian Orogeny and associated with the presence of deep-level shear zones (Higgins & Van Breemen, 1996; Gobeil et al. 2002). In the Central-South Grenville (Fig.1b), Hebert et al. (2009) summarized four distinct pulses of magmatism, with major occurrences in the region of Saguenay-Lac Saint Jean, Quebec: I) the 1327 ± 16 Ma labradorite-type De La Blache Mafic Suite (Gobeil et al. 2002); II) the 1160-1135 Ma labradorite- and andesine-type Lac St. Jean Anorthosite Suite (Higgins & Van Breemen, 1992; 1996; Higgins et al. 2002), which is the largest anorthosite suite in the world (Ashwal, 1993); III) the 1082-1045 Ma Pipmuacan Anorthosite Suite, including the andesine-type Vanel Anorthosite, the Poulin de Courval Mangerite and the coeval Saint-Urbain anorthosite (Higgins & Van Breemen, 1996; Morisset et al. 2009); IV) the 1020-1008 Ma andesine-type Valin Anorthosite Suite, including the Mattawa Anorthosite (Hebert et al. 2005; Owens & Dymek, 2005), the Labrieville Alkalic Anorthosite Massif (Owens & Dymek, 1992; 1995; Owens et al. 1993; 1994), the Gouin Charnockite (Hebert et al. 2005) and the La Hache Mangerite (Hebert et al. 2005).

Among the AMCG suites observed in the Central Grenville Province, a variation in the assemblage of oxide (from magnetite to hemo-ilmenite), mafic silicates (olivine to orthopyroxene) and plagioclase composition (from labradorite to andesine) (Dymek & Owens, 2002; Hebert et al. 2005; 2009; Grant, 2020) seems to be directly related to the age of the anorthosite suite: I) labradorite-type anorthosites are exclusively older than 1130 Ma, can be olivine-bearing or orthopyroxene-bearing and host Fe-Ti-V mineralization, dominated by magnetite; II) anorthosites younger than 1130 Ma are exclusively andesine in composition and dominated by orthopyroxene (olivine is absent) and host Fe-Ti mineralization; and III) the presence of hemo-ilmenite is also exclusive to anorthosite suites younger than 1130 Ma. Phosphate mineralization is spatially associated with anorthosites of all ages.

Local geology of the Lac à l'Orignal Fe-Ti-P deposit

The Lac à l'Orignal deposit is one of a number of Fe-Ti-P mineralized lenses located approximately 100km northeast of Chicoutimi (Quebec, Canada), within the Central part of the Grenville Province. It outcrops near the border of two anorthosite intrusions (Vanel and Mattawa), both of which were emplaced near lower-crustal shear zones of the Saint Fulgence and the Pipmuacan Deformation Zone in the northeast margin of the Lac Saint Jean Anorthosite Suite (Fig.1c). Lac à l'Orignal is located within the 1080 (±2) Ma Vanel Anorthosite (Hebert & Van Breemen, 2004; Hebert et al. 2009) near the northern margin of the younger, dome-shaped 1016 (±2) Ma Mattawa Anorthosite (Owens & Dymek, 2005; Hebert et al. 2009). The limit of the two anorthosites was

160 drawn on the geological map with the aid of geophysics (Mattawa has distinctive low magnetitic response
161 compared to Vanel). However, based on the An content of plagioclase Owens & Dymek (2005) showed that the
162 core of Mattawa (with the low magnetite response) has much lower An contents (29-37) than the border zone
163 (An39 – 45) which hosts several lenses of leuconorite and Fe-Ti-P-rich rocks (Fig.1c); the latter was used to date
164 the Mattawa anorthosite (Hebert et al. 2005). However, the 'border zone' is designated as the Vanel Anorthosite
165 on the geological map. Indeed, the plagioclase composition of the Vanel Anorthosite away from Mattawa has
166 similar compositions (Miloski et al. 2023 *in review*). This illustrates how complex it can be to distinguish different
167 types of anorthosite massifs in the field.

168 Observations from surface outcrops and drillcore in this study (Fig.2) indicate that the deposit is
169 comprised of oxide apatite norite (OAN) with approximate mineral proportions of Fe-oxides (15 - 25%), apatite
170 (8 - 20%) and orthopyroxene surrounding coarser plagioclase (Figs.2a-b). Locally there are patches (20-30cm) of
171 pegmatitic-OAN (Fig.2c). Layering occurs between OAN and thin (10 – 20 cm thick) anorthosite layers (Fig.2d),
172 which are sometimes apatite-bearing. These anorthosite levels within the mineralization contain similar to even
173 higher amounts of apatite in comparison with the OAN cumulates. One portion of the analyzed drillcore contains
174 a 40cm-thick anorthosite layer with a 20 cm-thick massive apatite portion (Fig.2e). Finally, several 30 cm thick
175 fine-grained OAN dykes crosscut the mineralization. The mineralization is hosted by pink anorthosite and
176 leuconorite, the latter containing up to 3 wt.% P_2O_5 (Fig.1d). Small massive oxides (20-40 cm) occur as lenses or
177 together with blocks of anorthosite (Fig.2f) near the contact with the main mineralized zone, both on outcrop and
178 in drill core.

179
180 **Sampling and analytical methods**

181
182 Fifty-eight samples spanning the entire sequence of one of the thickest portions (around 100m) of the
183 mineralized zone (drillcore LO-14-21, Fig. 3) were selected for detailed lithological description. In addition, three
184 samples from surface outcrops (Fe-Ti-P zones, massive oxides and host-anorthosite) were included. From these,
185 thirty-eight samples were selected for petrographic descriptions and modal mineral abundances estimates from
186 polished thin sections using an optical microscope. A subset of eleven samples covering the entire drillcore
187 stratigraphy were selected for chemical mapping using the Bruker - Tornado M4 micro-X-Ray fluorescence
188 (µXRF) analysis at Université Laval, Quebec.

189 Thirty-eight samples were selected for major and trace elements determinations by whole rock and by
190 in-situ analysis of the rock-forming minerals. Details of the following analytical methods, instrumentation and
191 evaluation of the data quality are discussed in ESM2. The samples were cut, crushed, and further reduced to
192 powder (~10 g) in an alumina mill at LabMaTer, Université du Québec à Chicoutimi (UQAC). Whole-rock
193 analysis was carried out by fusion of rock powder to form a lithium-borate glass bead that was then analyzed for
194 major and trace elements, in situ, by laser ablation inductively coupled plasma mass spectrometry (LA-ICP-MS)
195 at LabMaTer, UQAC, following the protocol of Barnes & Mansur (2020). The major and trace element
196 geochemistry of plagioclase (n=168), apatite (n=132), ilmenite (n=108) and magnetite (n=88), in-situ by LA-ICP-
197 MS at LabMaTer, UQAC was also carried out on polished thin sections from the same 38 samples. In addition,
198 one sample was selected for detailed LA-ICP-MS 2D mapping of the oxides using a time of flight (TOF) ICP-MS
199 at LabMaTer, UQAC

200   Fifteen samples were selected for the analysis of major and minor elements of plagioclase (n=57),
201   orthopyroxene (n=59), magnetite (n=41), ilmenite (n=81), apatite (n=54) and biotite (n=27) by electronprobe
202   microanalysis (EPMA) at Université Laval, Quebec. This was done to verify the value for the internal standard
203   necessary for some minerals during the LA-ICP-MS data reduction, as well as to compare with major element
204   results obtained by LA-ICP-MS (ESM2, Fig.2). Thirteen samples containing hemo-ilmenite were also analyzed
205   by EDX analysis, using a scanning electron microscope (SEM) at Université Laval, of a 500 x 500μm area
206   covering exsolutions of hematite in ilmenite. This was carried out in order to determine the major element
207   composition of hemo-ilmenite that better approximates the results from the LA-ICP-MS raster lines, due to the
208   presence of abundant hematite exsolutions in ilmenite. Whole-rock CIPW norm was done using standard
209   calculations. Recalculation of An*/Or* contents following Owens & Dymek (2005). The calculated cationic
210   proportions, the recalculation of Fe^{+2}/Fe^{+3} ratios and the An content of plagioclase were done using mass balance
211   equations/spreadsheets (ESM2).

212   Two samples of mineralized rocks, one from each of the core and border of the intrusion, were selected
213   for U-Pb dating of zircon (see samples location on Fig.3). Zircon separation, preparation and U-Pb analysis,
214   determined by LA-High Resolution-ICP-MS, following the protocol of Perrot et al. (2017), were conducted at the
215   GEOTOP labs in the Université du Québec à Montréal (UQAM).

216   **Results**
217   **Petrography and cumulate stratigraphy**
218
219   The stratigraphic variation of the mineralized zone (from drillcore LO-14-21) is displayed in Figure 3,
220   based on petrographic (both macro and microscale, Electronic Supplementary Material 1, ESM1; Figs.4 & 5)
221   observations, whole rock data, μXRF maps and the An content of plagioclase. The presence of layering within
222   the Lac à l'Orignal mineralized zone (Fig.2d) suggests a cumulate origin. Thus, the nomenclature of Irvine (1982)
223   is used whereby the first letter of their cumulus phases are followed by -C, meaning 'cumulus'.

224   The Lac à l'Orignal deposit is dominated by medium to coarse-grained oxide-apatite-norite (OAN)
225   cumulates (phiam-C, Fig.4a), comprising plagioclase (30-40%), orthopyroxene (15-35%), Fe-oxides (15-25%)
226   and apatite (5-20%) as major phases. Accessory minerals include fine-grained exsolutions of Al-spinel from oxide
227   phases (Fig.5h) and sulfides (Fig.5e-g). Apatite is homogeneously present throughout the entire cumulate
228   succession, from the bottom to the top of the mineralized interval, being most commonly associated with oxide
229   phases (Fig.3). Samples are fresh and well-preserved without hydrothermal alteration.

230   Overall, the cumulus phases (plagioclase, orthopyroxene, apatite, magnetite (hemo)-ilmenite) are present
231   throughout the mineralized zone, but with varying modal proportions (Fig.3 & Electronic Supplementary Material
232   2, ESM2). In particular, the oxide mineralogy reveals a distinct zonation (discussed in more detail below): hemo-
233   ilmenite (ilmenite with hematite exsolutions) is restricted to the borders whereas ilmenite, free of hematite-
234   exsolutions, occurs in the core. In general, the lower part of the intrusion (50-90m depth) is characterized by
235   higher amounts of orthopyroxene (melanocratic) than the upper part (above 40m depth), where plagioclase is the
236   predominant mineral phase, forming leucocratic oxide-apatite-norite (Fig.3). In a few places (between 12-25m
237   and around 70m depth), the OAN gradually coarsens towards a pocket (10-20cm thick) of pegmatitic coarse-

grained OAN (phiam-C, Figs.2c & 4b), with centimetric-scale orthopyroxene containing rutile exsolutions (Fig.4c). Massive nelsonite (oxide and apatite) is uncommon in the studied drillcore: one small (10cm-thick) nelsonite layer (55%: hemo-ilmenite + ilmenite + magnetite and 35% apatite) (iamph-C) was observed in the upper border (at 20.9m, Fig.4d). Several medium-grained anorthosite layers (10-50cm) occur throughout the mineralized zone, most of them containing high-amounts (7-20%) of apatite (pa-C) within plagioclase but low proportions of Fe-Ti oxides and orthopyroxene (Figs.4e-f). A massive apatite (ap-C) layer (20cm thick) that lacks oxides, with euhedral/medium-grained apatite crystals, occurs at the top of the stratigraphy (4.6m, Fig.4g) in sharp contact with an apatite-bearing anorthosite layer. Apatite crystals are euhedral. This is unexpected because massive apatite without oxides has never been reported. Plagioclase throughout the mineralized zone, in both OAN and ap-bearing anorthosite layers, is andesine in composition (An 40–50: Fig.4) with exsolutions of K-rich phase (Fig.4e).

Two fine-grained oxide-apatite-norite (phiam-C, Fig.4h) dykes/sills (30cm thick each) occur in sharp contact within the upper 10m of the upper border of the intrusion. They share similar mineralogy, and plagioclase composition, with the coarser-grained OAN mineralization and represent rapidly cooled, thin injections of ferrodiorite/jotunite magma. Hemo-ilmenite is the main oxide phase in these fine-grained dykes, whereby magnetite is nearly or completely absent.

The lower contact of the mineralized zone comprises the host pink anorthosite (Fig.4i), which is distinct in composition from the apatite-bearing anorthosite layers (andesine) within the mineralized zone. The host anorthosite is labradorite (An > 50) in composition and contains anti-perthite textures with no apatite. Surface outcrops adjacent to the mineralized zone, contain irregular lenses of massive oxides (magnetite + ilmenite; hemo-ilmenite with no apatite) hosting andesine-anorthosite blocks (sample 20PM03, An 50-51, Fig.2f). Grant (2020) previously described similar massive oxides within the anorthosite-host at the lower contact of drill core LO-12-13 (sample MG-LO-04).

Oxide petrography

The Lac à l'Orignal deposit is (hemo)-ilmenite-dominated, similar to other Fe-Ti-(P) occurrences associated with the younger anorthosites in the Grenville province (e.g., Grader intrusion (Charlier et al. 2008); Lac Tio (Charlier et al. 2010)). However, the oxide mineralogy changes from the borders to the core (Figs.3 & 5). Both the top (0-30m, Figs.5a & 5e) and bottom (30-105m, Fig.5d) borders of the mineralized zone are dominated by cumulus hemo-ilmenite, hosting large hematite exsolution lamellae. In contrast, the core (30 - 90m, Figs.5c & 5g) contains Fe-poor ilmenite that is devoid of hematite exsolutions. Magnetite is also present as a cumulus oxide throughout the OAN mineralized zone, commonly as a minor cumulus phase at the borders (ilm/mt ratios = 6.0 to 0.7, decreasing towards the core) or in similar proportions to ilmenite in the core of the intrusion (ilm/mt ratios = 2.4 -0.4).

At the transition between the border and the core (20 – 30m, Fig. 5f), ilmenite and hemo-ilmenite coexist, the latter typically contains finer hematite lamellae. In this case, hemo-ilmenite also presents a depletion in hematite exsolutions (size and quantity) towards the contact with adjacent magnetite (Figs.5f & 5h). Al-spinel is an accessory oxide phase. Re-equilibration between magnetite and ilmenite produces fine-grained irregular Al-spinel exsolutions at the contact of magnetite and ilmenite (Figs.5g-h). Fine-grained Al-spinel exsolution lamellae,

276 following preferential crystallographic directions, also occur in magnetite and Al-spinel commonly forms external
277 granules in ilmenite.

278
279 **U-Pb dating**

280
281   The U–Pb results for zircon analyzed from the upper border and core of the mineralized zone are
282 presented in Table 6. The Concordia diagrams for these 2 samples are shown in Figure 6a, where all the ages are
283 presented with the calculated 2σ uncertainties. Representative cathode luminescence photomicrographs of the
284 zircon grains selected for dating are also displayed in Figure 6b. The complete cathode luminescence
285 photomicrographs (ESM3) show that they comprise single grains of subhedral prismatic to anhedral igneous
286 zircons with simple, magmatic zoning. Although some show darker cores (e.g., in LOR1) their ages are similar to
287 those of the paler borders. Weighted mean diagrams (ESM3) show a normal distribution of a single population
288 of zircons for each sample.
289   Sample LOR-1 is a leucocratic oxide-apatite norite (OAN) located at the upper border of the intrusion
290 (14m - 16m depth), dominated by hemo-ilmenite ($\pm$ magnetite). The calculated concordia age, based on all the
291 zircon grains (n=14) is 1069 $\pm$ 13 Ma, which is within the range of crystallization ages of the Pipmuacan
292 Anorthosite Suite (1080 – 1060Ma) and the nearby Vanel Anorthosite (1080.0 $\pm$ 2.0 Ma, Hebert et al. 2009).
293 Sample LOR-2 is a melanocratic oxide-apatite norite from the core of the intrusion (41m and 43m depth),
294 dominated by ilmenite + magnetite. The calculated Concordia age for all the concordant zircon grains (n=16) is
295 993 $\pm$ 13 Ma, which is significantly younger than the age of the border, and closer to the crystallization age of the
296 nearby Mattawa Anorthosite (1016 $\pm$ 2 Ma, Hebert et al. 2005). These new dates indicate that the Lac à l'Orignal
297 intrusion is multi-phase with an older border and a younger core.

298
299 **Whole-rock geochemistry**

300   The whole rock geochemistry of mineralized samples (n = 33), fine-grained dykes (n = 2) and host
301 anorthosite (n = 4), containing massive oxides (n = 2), is presented in Table 1 (complete data and CIPW norm
302 calculations are presented in ESM 1; Table 4) and confirms our petrographic observations. The stratigraphic
303 variation in whole-rock composition is presented in Figure 3 & Electronic Supplementary Material 3 (ESM3) and
304 binary variation diagrams in Figure 7. As expected, the oxide-apatite norite cumulates from the mineralized zone
305 are characterized by relatively high-Fe_2O_{3t} (14.2 - 47.1%), TiO_2 (2.8 - 7.7%), V (181 – 722ppm), P_2O_5 (3.1 - 8.1%)
306 and MgO (2.8 – 10.8%) contents and low-SiO_2 (20.2 – 42.5%), Al_2O_3 (7.1 – 16.7%) and Na_2O (0.1 – 3.4%),
307 reflecting much higher proportions of Fe-Ti oxides, apatite (CIPW norm: 7.4 -19.3 wt.% ap.) and orthopyroxene,
308 and lower proportions of plagioclase in the mineralized cumulates when compared to the host anorthosites. The
309 CIPW norm confirms a K-rich andesine-type plagioclase (An* = 45.60, Or* = 7.78) for the OAN mineralization
310 on average. The ilmenite-bearing OAN in the core tends to have higher Fe_2O_{3t}, TiO_2, V, MgO and lower SiO_2,
311 CaO, Na_2O and K_2O confirming that this part of the mineralization is more melanocratic, with higher proportions
312 of oxides and orthopyroxene and lower plagioclase, respectively, than the hemo-ilmenite bearing border zones
313 which tend to me more leucocratic.

314   The apatite-bearing anorthosite layers (pa-C) have similar P_2O_5 contents (4.5 – 5.6 wt.%) as the OAN
315 zone, but much lower Fe_2O_{3t} (6.5 -7.3 wt.%), MgO (1.6 – 1.7 wt.%) and TiO_2 (0.9 – 1.3 wt.%), confirming the

316 low proportions of orthopyroxene and oxides. The plagioclase is also K-rich andesine-type (CIPW norm: An* 42,

317 Or* 7.8). The fine-grained OAN dykes (phiam-C) are chemically very similar to the leuco-OAN border group for

318 all elements (Fig.7). There are two types of host anorthosite (p-C) based on An and K contents, determined by

319 CIPW-norm (ESM1): 1) a K-poor (0.36 to 0.46 wt.% K_2O), labradorite-type (An > 50) anorthosite (CIPW norm:

320 An* = 57.1 – 59.1, Or* = 2.3 – 2.8) with higher CaO (10.8 – 11.0%) and Al_2O_3 (28.0 – 28.1%), sampled below

321 the mineralized zone; 2) a K-rich (1.4 – 1.5% K_2O), andesine-type (An < 50) anorthosite (CIPW norm: An* =

322 40.9 – 43.3, Or* = 10.0 – 10.7) with lower CaO (7.1 – 8.4%) and Al_2O_3 (22.7 – 23.2%), sampled above the

323 mineralized zone on surface. Both host anorthosites are P-poor (< 0.1 wt.% P_2O_5) in comparison to apatite-bearing

324 anorthosite layers within the mineralized zone.

325   The massive oxides in the host anorthosite (andesine-type) have the highest Fe_2O_{3t} (54.5 - 71.4 wt.%),

326 TiO_2 (9.5 - 12.1 wt.%) and V (1769 ppm) contents and lowest CaO and P_2O_5 values among all mineralized

327 samples, due to a much higher proportion of magnetite to ilmenite (Fig.2) and the lack of plagioclase and apatite,

328 respectively. In Figure.7, massive oxides plot on the same trends for Fe_2O_{3t} and TiO_2 as OAN cumulates, but not

329 for V, for example, due to their higher concentration of ilmenite and magnetite.

330   Chondrite-normalized REE diagrams (Fig.8) show similar patterns between the OAN cumulates from

331 the border (leucocratic, Hm-ilm + mt) and core (melanocratic, Ilm + mt), suggesting that they formed from similar

332 magma compositions. These mineralized rocks are enriched in LREE (80 – 300x chondrite) relative to HREE (10

333 – 30x chondrite), presenting a smooth pattern with weak, negative Eu-anomalies (Eu* between 0.7 and 0.8).

334 Moreover, leucocratic OAN tend to have a slightly higher abundance of REE in comparison with melanocratic

335 OAN. The apatite-bearing anorthosite layers also have the same REE patterns as that of the OAN mineralization

336 (Fig.8b), indicating that cumulus apatite controls the distribution of REE and also formed from a similar magma

337 as the mineralization. Finally, the fine-grained OAN dykes have very similar patterns to that of the OAN and have

338 the highest REE abundance.

339   The host-anorthosite samples have distinct REE patterns (Fig.8b) compared to the OAN mineralization,

340 presenting enrichment in LREE and positive Eu-anomalies, typical of plagioclase accumulation, and lower overall

341 REE concentrations. The labradorite-type anorthosite below the mineralization has lower REE values in

342 comparison to the andesine-type anorthosite (associated with massive oxides) above the mineralization, which

343 has a flatter distribution between light and heavy-REE due to the slightly higher amounts of apatite in relation to

344 the other host-anorthosite samples (P_2O_5 < 0.1 wt.%). Massive oxide samples, absent of apatite, have much lower

345 REE abundances compared to the other cumulates (Fig.8a).

346 **Mineral chemistry**

347
348   The mineral compositions of plagioclase, apatite, ilmenite and magnetite determined by LA-ICP-MS, for

349 mineralized rocks and host rocks of Lac à l'Orignal, are presented in Tables 2 - 5 (with full results in ESM1 and

350 ESM3). The stratigraphic variation of selected elements is presented in Figure 9.

351   Plagioclase from the OAN mineralization (both coarse-grained and pegmatitic pockets) are K-rich

352 andesine in composition (Fig.9a), varying from $An_{39.4}$ to $An_{50.1}$ and from $Or_{0.7}$ to $Or_{7.9}$. They have Sr (1501 to 2337

353 ppm) and Ba (193 to 1016 ppm) compositions that are higher compared to plagioclase (An_{58}, $Or_{1.3}$ to $Or_{2.9}$) in the

354 host labradorite-type anorthosite below the mineralization (Sr contents of 631 -644 ppm and Ba of 90 – 93 ppm).

Plagioclase from the apatite-bearing anorthosite layers within the mineralized zone ($An_{44.7}$ to $An_{45.3}$, $Or_{3.2}$ to $Or_{3.4}$, Sr = 2005 -2154 ppm and Ba = 322 – 343 ppm) are similar in composition to plagioclase from the OAN. However, at the same stratigraphic level, the Sr and Ba content of plagioclase from the apatite-bearing anorthosite layers are significantly lower than those from the adjacent OAN. Comparing the borders (dominated by hm-ilmenite + magnetite) with the core of the intrusion (dominated by Fe-poor ilmenite + magnetite) relatively constant An, Or and Sr values are observed, whereas Ba is relatively enriched in the core of the intrusion (Fig.9a). However, Or contents are erratically higher (< 10) in the lower-border of the intrusion, due to the presence of K-rich exsolutions.

Apatite trace element concentrations (Fig.9b) are overall fairly similar for the coarse-grained OAN, pegmatitic OAN and apatite-bearing anorthosite levels within the mineralized zone. The Sr values in apatite varies from 679 to 1501 ppm, with the lowest values at the outer borders of the intrusion and relatively higher Sr values (1300 ppm) in the core of the intrusion (around 65 – 78m). This subtle variation for Sr in apatite matches that for Sr in plagioclase, which has higher Sr content than that of apatite. The massive nelsonite layer has apatite with an exceptionally high Sr content within the upper border (1501 ppm) but contains no plagioclase to compare with. The REE content of apatite slightly increases up-section from the bottom (1407 ppm: sample LO-57) to the upper border (2769 ppm: LO-01). Moreover, Eu/Eu* values are constant throughout the core and reaches lower values in the borders, particularly where overall abundance in REE is higher.

The REE contents of apatite, normalized to chondrite (Fig.10a), show very similar shaped patterns for the OAN samples from the border (hm-ilm + mt) and core (ilm + mt) indicating that they probably formed from a similar magma composition. Both are characterized by weak negative Eu anomalies (Eu/Eu* = 0.63 – 0.83) and LREE enrichment (La/Yb_N = 12.7 - 17.7), typical of igneous apatite. The apatite REE patterns from the fine-grained OAN dykes are similar to apatite REE patterns from the mineralization (Fig.10a). In particular, the dyke with the lower abundance of REE (sample LO-06) has identical REE and Sr composition as the most REE-enriched apatite from the border zone, indicating that this is similar to the parental melt of the mineralization. However, the dyke (sample LO-08) that is most enriched in REE, has a larger negative Eu anomaly (Eu/Eu* = 0.51 and La/Yb_N = 9.5) and lower Sr (680 ppm), typical of a more evolved melt. The similarity of the chondrite-normalized REE patterns of whole-rock analyses with the apatite analyzes (Fig.10b) indicates that the REE content of the Lac a l'Orignal deposit is controlled by apatite crystallization.

The fraction of hematite in ilmenite (Xhm) varies from 0.07 to 0.60, with the lower values in the core of the intrusion (31-92m depth), where hematite exsolutions are almost absent in ilmenite (Fig.9c). Higher Xhm contents are observed in the lower and upper borders of the intrusion, where coarse hematite exsolutions in hemo-ilmenite are common (Fig 5). The V (384 to 2603 ppm) concentrations of ilmenite follow an identical behaviour to that of the Xhm values, with higher V contents corresponding to higher hematite contents at the borders. In general, Ni (0.8 to 20.7 ppm) and Cr (3.7 to 157 ppm) are also higher in hemo-ilmenite from the borders, whereas MgO (0.2 to 2.8 wt.%) and MnO (0.12 to 1.0 wt.%) are typically lower in the borders than the core. Therefore, the trace-element variation for (hemo)-ilmenite in the Lac à l'Orignal intrusion appears to be directly related with the presence or absence of hematite exsolutions, marking distinct geochemical patterns between the borders and the center of the intrusion. In the core some grains of hm-ilm (e.g., from 35 – 58m) have relatively high Ni, V and Cr contents that are similar to those observed at the borders, although lacking elevated Xhm. Relatively higher MgO, MnO, Ni and Cr values are observed above the nelsonite (iap-C) layer, at the top border of the intrusion. Such irregular patterns with reversals to more primitive compositions within the intrusion may indicate the

395 presence of magma reinjections. Ilmenite in the massive oxide within the host-anorthosite has the lowest Xhm
396 (0.07-0.10) and V contents (859-937 ppm) of all and are almost absent of hematite exsolutions. However, their
397 Cr (167-180 ppm) and Ni (50-60 ppm) contents are much higher in comparison with the values for ilmenite in the
398 OAN mineralization.

399   Similar to ilmenite, magnetite shows cryptic variation for Cr (14 - 1244 ppm) and Ni (9.3 – 197.9 ppm)
400 (Fig.9d). This includes higher values of Cr (1961-2544 ppm) and Ni (470 – 507 ppm) in the oxide minerals from
401 the massive oxides. In contrast to ilmenite, V in magnetite behaves more similarly to Ni and Cr with higher V
402 (3041 – 3536 ppm) concentrations in magnetite from the massive oxides compared to that from the OAN
403 mineralized zone (9.3 – 197.9 ppm V).

Discussions
404

405

406   Our study reveals that the Lac à l'Orignal Fe-Ti-P deposit is a multi-phase lenticular intrusion comprising
407 cumulates of oxide-apatite norite (OAN). The older border (1069 ± 12 Ma) is dominated by hemo-ilmenite (±
408 magnetite) and is more leucocratic whereas the younger core (993 ± 13 Ma) is dominated by ilmenite and
409 magnetite and more melanocratic. Weighted mean diagrams (ESM3) show a normal distribution of a single
410 population of zircons, precluding the occurrence of inheritance. This is confirmed with the CL images of zircons
411 which although some show darker cores (e.g., in LOR1) their ages are similar to those from the paler borders.
412 Also zircon is most likely undersaturated in magmas of ferrodiorite composition until it reaches a high degree of
413 crystallinity therefore not preserving a lot of inherited zircon (e.g. Watson & Harrison, 1983). Therefore, the
414 difference in ages of the border and core is unlikely due to inheritance of zircons. However, chondrite-normalized
415 REE compositions (of whole rock and apatite) present similar patterns between the border and core of the
416 mineralized OAN-body, indicating that at least two magma injections of similar composition, formed the Lac à
417 l'Orignal mineralized intrusion over a period of 80 Ma. Exceptionally, the older intrusion is preserved at the
418 border of the younger intrusion. Furthermore, the Lac à l'Orignal intrusion is layered, with thin horizons of apatite-
419 bearing anorthosite and, less commonly, massive nelsonite of similar plagioclase and apatite chemistry as that of
420 the OAN mineralization. This suggests that it formed as cumulate segregation from the magmas. The border is
421 crosscut by fine-grained OAN dykes of similar mineralogy and apatite chemistry to the mineralization, suggesting
422 a co-genetic link which is demonstrated below.

423   According to Dymek & Owens (2001), OAGN (oxide-apatite-gabbro-norite) in the Grenville Province,
424 Canada, occurs as 1) discordant to concordant sill-like bodies within anorthosite massifs, 2) as layers along or
425 near the outer boundaries of anorthosite massifs, or 3) as layers within associated jotunite or mangerite. The Lac
426 à l'Orignal mineralized intrusion is located near the boundary of two massif-type anorthosites: Vanel and
427 Mattawa, whose ages are similar to those obtained in our study for the border and core of the intrusion,
428 respectively. Furthermore, OAGN can form at various stages in the evolution of a particular massif anorthosite
429 complex and represent mainly cumulate segregation from jotunite/ferrodiorite liquids, with the proportion of
430 oxide-apatite-pyroxene reflecting a cotectic assemblage (Owens & Dymek, 1992). According to these authors,
431 OAGN host more evolved mineral compositions than anorthosites and massive nelsonite/oxide layers, indicating
432 generation from more evolved magmas, i.e., in latter stage of fractionation after massive oxide/plagioclase
433 crystallization, from which jotunite liquids would form (Vander Auwera & Longhi, 1994; Vander Auwera et al.
434 1998). In the Lac à l'Orignal deposit, in contrast to most of the hemo-ilmenite dominated OAGN occurrences

435   described above, there is a lack of massive oxide and or massive nelsonite layers at the base of the main

436   mineralized body. Also, cumulus apatite and magnetite are present throughout the intrusion, in addition to hemo-

437   ilmenite, thus suggesting a more evolved character for these cumulates in relation to other Fe-Ti-(P) occurrences

438   in the Grenville Province (e.g., Grader intrusion, Charlier et al. 2008; Lac Tio, Charlier et al. 2010; Saint-Urbain

439   Anorthosite, Morisset et al. 2009) which contain less magnetite.

440   **Parental magma**

441

442   Apatite is an important phase in the late-stage evolution of layered intrusions and massif-type anorthosite

443   complexes where it crystallizes, along with Fe-Ti oxides, from an evolved magma, enriched in Fe, Ti and P (Toplis

444   et al. 1994) and can accumulate to form, in some cases, Fe-Ti-P mineralization (McLelland et al. 1994; Dymek &

445   Owens, 2001; Tollari et al. 2008; Charlier et al. 2008; Namur et al. 2010; 2012). Evolved magmas, such as

446   ferrodiorite and/or jotunite, are commonly interpreted as liquids associated with massif-type anorthosites and have

447   been shown to be co-genetically related to the Fe-Ti-P mineralization either as a parental or residual magma

448   (Owens et al. 1993; Vander Auwera et al. 1998). These melts are unusually enriched in Fe_2O_{3t} (13.2-21.9 %),

449   TiO_2 (3.1-6.0%) and P_2O_5 (0.8-3.9%) (ESM1). High concentrations of P_2O_5 in evolved magmas leads to the

450   formation of silicate melts with much higher Fe contents than is possible for P-poor compositions, allowing for

451   concentration of Fe and Ti at higher levels (Toplis et al. 1994). This is partially because the increasing P_2O_5

452   content decreases the stability field of magnetite whereas the relative abundance of ilmenite remains

453   approximately constant. Thus, the high P_2O_5 content of ferrodioritic or jotunitic liquids associated with anorthosite

454   suites (e.g., Mitchell et al. 1996; Vander Auwera et al. 1998) is responsible for some their characteristics, such as

455   the common early saturation of ilmenite compared to magnetite (Charlier et al. 2015).

456   The fine-grained dykes at Lac à l'Orignal (LO-06 and LO-08: Table 1) are very similar in bulk

457   composition to fine-grained ferrodiorite/jotunite dykes compiled from other Fe-Ti-(P) mineralization and

458   anorthosite massifs, in particular the dykes from the Grader intrusion (ESM1). Moreover, at Lac à l'Orignal these

459   fine-grained lithologies present the same mineralogy and similar geochemistry (whole rock and apatite REE

460   patterns) as the border-OAN cumulates in the mineralization, suggesting they are co-genetic with the

461   mineralization, although dykes present more evolved apatite compositions (higher REE and Y and lower Sr).

462   The relationship between the fine-grained dykes and melt compositions in equilibrium with the

463   cumulates can be evaluated from the composition of cumulus apatite in the intrusion, by inverting the composition

464   of apatite using the equation $CLiq\ REE = \frac{CAp\ REE}{DAp\ REE}$. The REE contents of the ferrodiorite dykes (samples LO-

465   06 and LO-08) are plotted (ESM3) along with REE patterns calculated for liquids in equilibrium with apatite from

466   the OAN cumulates of Lac à l'Orignal, using empirically determined $DAp\ REE$ values (Table 7) obtained from

467   the gabbronorite cumulates of the Bjerkreim–Sokndal layered intrusion (Charlier et al. 2005). This approach was

468   previously applied by Charlier et al. (2008) to the oxide-apatite gabbronorites of the Grader intrusion, Quebec,

469   which has similar mineralogy to the Lac à l'Orignal deposit. The calculated liquids in equilibrium with apatite

470   show similar REE contents and patterns as those of the fine-grained ferrodiorite (OAN) dykes, suggesting that

471   these dykes could represent melts that were in equilibrium with the oxide-apatite-norites, and related apatite-

472   bearing cumulates. However, the calculated liquids have slightly positive Eu anomalies, and do not match the

473   small-negative Eu anomalies observed in both of the fine-grained dykes from Lac à l'Orignal. A similar mismatch

474   for Eu was also observed for the melt composition calculated from apatite of the Grader intrusion compared to

475   their dykes (Charlier et al. 2008). As pointed out by Charlier et al. (2008), the DAp Eu value (3.9) of Charlier *et*
476   *al.* (2005) overestimates the value for the calculated melt of the Grader intrusion, because the DAp Eu is too low.
477   Europium is sensitive to redox conditions. At high fO_2, the relative proportion of Eu^{3+} and Eu^{2+} is also higher in
478   apatite because DAp $Eu3+$ > DAp $Eu2+$ (Roelandts & Duchesne, 1979). Thus, the mismatch in Eu at the
479   Grader intrusion indicated that crystallization of apatite occurred under higher fO$_2$ conditions (between NNO +0.5
480   + & 1.0) at Grader intrusion than that at Bjerkrein-Sokndal layered intrusion. This is supported by higher hematite
481   content in ilmenite in Grader (X$_{hem}$ = 0.20 – 0.32, Charlier *et al.* 2008) compared to that in the Bjerkrein-Sokndal
482   layered intrusion (X$_{hem}$ = 0.03 – 0.19, Duchesne, 1972). At Lac à l'Orignal, the high hematite content of ilmenite
483   in the dykes (Xhem = 0.42 – 0.55) and that preserved in the border of the OAN mineralization (X$_{hem}$ = 0.10 –
484   0.60) also indicates similar or even higher fO_2 conditions of the melt (see below). Higher fO_2 conditions would
485   thus result in a higher ratio of Eu^{3+}/Eu^{2+} in the melt and higher DAp Eu , explaining the mismatch in Eu anomalies
486   observed in ESM3. To avoid possible inconsistences in using partition coefficients determined from Bjerkrein-
487   Sokndal, in particular for DAp Eu , new DAp REE values were determined for this study using whole rock REE
488   and apatite REE values of the fine-grained OAN dykes from Lac à l'Orignal itself, using the equation:
489   DAp REE $= \frac{CAp\ REE}{CLiq\ REE}$ (Table 7).

490   Liquids in equilibrium with apatite from the OAN mineralization were then recalculated applying the
491   new DAp REE values from the least evolved (sample LO-06; Fig.10c) and most evolved (sample LO-08; ESM3)
492   dykes. The REE patterns, including Eu anomalies, and abundance of REE of the calculated liquids perfectly match
493   the fine-grained OAN dykes when applying partition coefficients from the least-evolved dyke (Fig.10c). However,
494   when using partition coefficients from the more evolved dyke, the calculated liquids have lower-REE
495   concentrations in comparison with the fine-grained dykes, due to higher DAp REE obtained from the evolved
496   dyke. These results indicate that the composition of the least-evolved fine-grained dyke (LO-06) better reflects an
497   initial liquid in equilibrium with the OAN cumulates (i.e., parental melt), whereas the dyke LO-08 would represent
498   a more-evolved, residual liquid at further stages of differentiation. Increased polymerization of a more evolved
499   liquid may explain the higher DAp REE calculated for this dyke.

500   **Oxygen fugacity**

501
502   To better constrain the probable high fO$_2$ conditions of the ferrodiorite magma forming the mineralization
503   at Lac à l'Orignal we used the QUILF program of Andersen et al. (1993) and input the mineral compositions of
504   magnetite-hemo-ilmenite pairs from the fine-grained OAN dyke. Given that the dykes cooled faster than the main
505   body, subsolidus modification should be less important and thus these samples are the best estimate for magmatic
506   conditions of the mineralization. Following Charlier et al. (2008), the fO_2 values at equilibrium between oxides
507   were obtained by fixing the liquidus temperatures between 1100 and 1200ºC (Vander Auwera & Longhi, 1994;
508   Vander Auwera et al. 1998), and pressures between 1-5Kbar (Charlier et al. 2008; Lin & Sawyer, 2018). The
509   calculations give values of fO_2 between - 6.97 and –7.85 and Δ log fO_2 (relative to FMQ) values between +0.9
510   and +1.7 (ESM1).

511   Plotting the calculated fO_2 values relative to the Fe content of orthopyroxene, in ESM3, shows that the
512   Lac à l'Orignal deposit falls into the ilm – hm + mt + opx field, which is compatible with the mineralogy present
513   in the OAN cumulates. Furthermore, it illustrates that the crystallization conditions of the Lac à l'Orignal deposit

514 was more oxidizing than the olivine-magnetite-bearing Kiglapait Intrusion of the Nain Plutonic Suite, Labrador
515 (Morse, 1982) but not as oxidizing as the hemo-ilmenite-orthopyroxene-bearing Labrieville Anorthosite (Owens
516 and Dymek, 2001; Frost et al. 2010).

517 In addition, we have determined the oxygen fugacity from the experimental calibration of the Fe–Ti
518 oxide thermo-oxybarometer of Lattard et al. (2005), applying the same range of temperature (1100-1200°C),
519 pressure (1-5Kbar) and the hematite content of ilmenite (Charlier et al. 2008). Applying the ilmenite composition
520 of the fine-grained OAN dykes (X_{Hm} between 0.45-0.56) to this range of values, calculations give FMQ between
521 +1.34 and +1.71 (NNO between +0.57 and +0.95), confirming the values obtained using QUILF. Furthermore,
522 such high-fO_2 values of the parental ferrodiorite liquid at Lac à l'Orignal are compatible with the inference of high
523 fO2 previously suggested above from the Eu* chemistry of apatite. Similar high oxygen fugacity (fO_2) conditions
524 (>+1 FMQ) were reported for the formation of hemo-ilmenite dominated OAGN cumulates at the Grader intrusion
525 (Charlier et al. 2008).

526 For mafic-basaltic systems, experimental studies on the stability fields of Fe–Ti oxides (Snyder et al.
527 1993; Toplis & Carroll, 1995) have shown that at high-fO_2 (>+1 FMQ) the magnetite–ulvöspinel solid solution
528 precedes the appearance of the ilmenite–hematite solid solution, whereas the reverse occurs at low-fO_2 (<+1
529 FMQ). However, according to Toplis & Carroll (1995), the fO_2 only affects the stability field of magnetite,
530 whereas the crystallization of ilmenite as the first oxide is controlled primarily by the TiO_2 content of the melt.
531 The crystallization of hematite-rich ilmenite in the Lac a l'Orignal Fe-Ti-P deposit is thus a reflection of the initial
532 high-TiO_2 content of the parental magma coupled with high-fO_2 conditions, as observed for the Grader intrusion
533 (Charlier et al. 2008; Morisset et al. 2009; 2010).

534
535 **Fractional crystallization**

536 In addition to the An content of plagioclase, trace elements in apatite and Fe-Ti oxides are useful, and
537 sometimes more sensitive, in tracing fractional crystallization processes (Fig. 11 and ESM3) and magma injections
538 (Namur et al. 2010; Tollari et al. 2008; Kieffer et al. 2022). In a magma chamber behaving as a closed system (i.e.
539 one that does not experience successive inputs of magma), elements that are highly compatible into Fe-Ti oxides,
540 such as Cr should be strongly enriched in the most primitive magnetite and ilmenite (associated with Fe-Ti-V
541 deposits). Subsequently crystallizing Fe-Ti oxides (associated with Fe-Ti-P deposits) would continuously
542 decrease (Fig.11) the concentration in highly compatible elements due to their progressive removal from the
543 residual magma (Barnes et al. 2004; Klemme et al. 2006; Tegner et al. 2006; Namur et al. 2010; Dare et al. 2014;
544 Grant, 2020). In more open systems, sharp reversals to higher concentrations of compatible elements are often
545 attributed to reinjections of a more primitive magma (Namur et al. 2010). However, the primary magmatic
546 composition of oxides can be modified, after crystallization, by sub-solidus processes both during cooling of the
547 intrusion and later by metamorphism (Duchesne, 1972; Arguin et al. 2018; Grant, 2020; Dare et al. 2019). In
548 contrast, sub-solidus re-equilibration processes seems to have minor influence on the trace element distribution in
549 apatite (Tollari et al. 2008).

550 Binary diagrams (ESM3) display some trace-element concentrations in plagioclase, apatite and oxides
551 as a function of the An content of plagioclase, used here as a proxy for tracking fractional crystallization. Data
552 from the Grader intrusion (Charlier et al. 2008) are plotted in comparison. Although plagioclase from Lac à

553 l'Orignal varies from An 50 to An 40, only the Or content significantly increases as An content decreases (ESM3),
554 whereas Sr and Ba contents in plagioclase do not vary with increasing degree of fractionation, suggesting a global
555 KD of around 1. This behaviour of K, Sr and Ba in plagioclase is similar to that from Grader, except the latter has
556 higher K and lower Sr concentrations. Similarly, the Sr, and Mn contents, of apatite also do not vary with
557 fractionation (ESM3), whereas the REE content shows a very slight increase with decreasing An content at both
558 Lac à l'Orignal and Grader, however there is significant scatter in REE for the borders of Lac à l'Orignal. Overall,
559 the Lac à l'Orignal deposit is similar to the upper portion of the Grader intrusion (ESM3), suggesting a more
560 evolved character, although the Sr contents of apatite and plagioclase in the former, are higher.

561 Cr and Ni contents in both magnetite and ilmenite of the Lac à l'Orignal deposit decrease together with
562 the An content of plagioclase (ESM3), behaving as compatible elements during fractional crystallization, although
563 there is some scatter. Nb and Zr values in ilmenite (ESM3), as expected, behave incompatibly, slightly increasing
564 with lower An contents. However, the V content of magnetite and ilmenite remains constant, and V has higher
565 concentrations, but more scattered distribution in hemo-ilmenite than in ilmenite. This is probably because $V^{3+, 4+}$
566 substitutes more easily into the Fe^{3+} site of the hematite component of hemo-ilmenite than the Fe^{2+} site of ilmenite,
567 which explains the correlation between V and Xhem content of ilmenite in Fig.11c. Toplis & Corgne (2002),
568 applying experiments on ferrobasalts, showed that V and Cr partitioning into magnetite is strongly dependent on
569 fO_2, resulting in a decrease in both partition coefficients with increasing oxidizing conditions. In phosphorous-
570 bearing systems, such as for the Lac à l'Orignal mineralization, D$mt/liq\ Cr$ decreases from 291 to 27 with
571 increasing oxygen fugacity (from NNO -0.7 to NNO +2.6), whereas D$mt/liq\ V$ decreases from 29 to 2.
572 Consequently, even at high-fO_2, Cr remains compatible during fractional crystallization whereas for the same
573 proportion of magnetite, V could remain unchanged (Duchesne et al. 2006; Charlier et al. 2009). The constant V
574 content in magnetite (V around 0.30 wt.%) in relation to the An content of plagioclase (ESM3) and with Cr in
575 magnetite (Fig.11a), implies a D$bulk/liq\ V$ around 1 in the OAGN cumulates, thus indicating a relatively low-
576 D$mt/liq\ V$. We interpret this to be the result of a relatively high-fO_2 of the magma that formed the Lac à l'Orignal
577 oxide-apatite mineralization. This is due to the high proportion of V^{4+} and V^{5+} in the melt at high-fO_2 which
578 partition less well into magnetite compared to V^{3+} (Toplis & Corgne, 2002). High-fO_2 is also responsible in part
579 for the similarly low and constant V content in magnetite from both Grader OAGN (Fig.11a; Charlier et al. 2008)
580 and the Fe-Ti ores of the Suwalki Anorthosite (Charlier et al. 2009).

581 The high Cr and Ni contents in ilmenite and magnetite as well as the lower Nb and Zr values in ilmenite
582 of the massive oxide sample (within the anorthosite-host, ESM3) indicate that this sample has a more primitive
583 composition in comparison with the main OAN mineralization, as previously noted by Owens & Dymek (1992)
584 in other locations in the Grenville Province. Fractional crystallization from ferrodiorite magmas initially
585 dominated by oxide (settling) + plagioclase (flotation) could explain the presence of massive layers of ilmenite +
586 magnetite within the anorthosite host. In further stages, fractional crystallization of the residual liquid, dominated
587 by Fe-Ti oxides, silicates and apatite would generate the OAN cumulates observed in the main intrusion.

588 The Lac à l'Orignal norite cumulates have a large range of V and Cr variation for ilmenite and magnetite
589 (Fig.11). In comparison, ilmenite in the Grader intrusion has higher Cr, Ni and V values in relation to Lac à
590 l'Orignal. During crystallization, Cr, V and Ni preferentially partition into magnetite over ilmenite (Dare et al.
591 2014; Arguin et al. 2018). The lower abundance of magnetite at Grader could result in higher Cr values for ilmenite

15

592 at this location, as well as a more primitive character (an initial high-Cr value) of its parental magma (s) in relation

593 to Lac à l'Orignal. The An content of Lac à l'Orignal (An50 – 40) is similar to that at Grader (An50-45) but

594 decreases to lower values, suggesting a more evolved magma.

595   Cumulates in Lac à l'Orignal present a higher Cr for both magnetite and ilmenite from the core in relation

596 to the upper border (Figs.9c-d), pointing for a more primitive character to the former in relation to the latter.

597 However, apatite trace element concentrations have a discrete REE enrichment up-section (Fig.9b), with slightly

598 lower Eu/Eu* values at the top border of the succession. The leuco-OAN's in the older border zone are more

599 plagioclase concentrated, which could have an influence on the behavior of certain elements that are controlled

600 by plagioclase, such as Eu and Sr. Moreover, the top border could have been affected by trapped liquid effect, in

601 which could have modified the concentration of REE at this portion, as previously described for the Fedorivka

602 intrusion (Duchesne et al. 2006). The more scatter distribution of REE compositions for the OAN-border, as

603 previously pointed in Figure 9b, corroborates that.

604   The role of liquid immiscibility in forming Fe-Ti-P-rich and Si-rich silicate melts has recently shown to

605 be fairly common in the late stages of fractionation of mafic melts (Namur *et al.* 2010; 2011; Charlier & Groove,

606 2012). Undisputed evidence for this is the presence of melt inclusions in apatite that record the 2 immiscible melts

607 (e.g., Charlier et al. 2008). At Lac a l'Orignal, no melt inclusions occur in apatite. Furthermore, bulk whole-rock

608 compositions of fine-grained OAN dykes, interpreted as liquidus compositions of Fe-Ti-P mineralization, were

609 projected onto ternary diagrams for liquid immiscibility evaluation, as previously applied to the Sept Iles Layered

610 Intrusion (ESM3, modified from Tollari *et al.* 2008; Charlier & Grove, 2012). Overall, the composition of

611 ferrodiorite dykes associated with Fe-Ti-P mineralization at Lac a l'Orignal, Quebec, fall outside of the liquid

612 immiscibility field (ESM2), supporting the model of fractional crystallization of a single magma as the main

613 process in the petrogenesis of these cumulates.

Post-cumulus modification in magnetite and ilmenite

615   The fractionation trends recorded by oxides at Lac à l'Orignal are more scattered than those from the

616 Grader intrusion (Fig.11 & ESM3) which could point to secondary modification of the primary composition of

617 the oxides. Alteration of a primary chemical composition of a mineral can occur through several modes of

618 'diffusive modification', a term used by Tanner et al. (2014) to describe the diffusive interchange occurring either

619 between compositional zones within a mineral, or between a mineral and the adjacent media (i.e., melts, minerals,

620 or volatile-rich fluids) as they attempt to attain equilibrium. In the Bushveld Complex, for example, both the

621 'trapped liquid shift' and subsolidus re-equilibration, during prolonged cooling of the intrusion, have been

622 identified as important modifiers of the trace element concentrations on cumulate minerals (Cawthorn, 2007;

623 Tanner et al. 2014).

624   Fe-Ti oxides can be modified by 3 different processes; 1) re-equilibration between magnetite and ilmenite

625 (inter-oxide re-equilibration), 2) re-equilibration between Fe-oxides and Fe-Mg silicates (oxide-silicate re-

626 equilibration), and 3) re-equilibration between magnetite/ilmenite and internal exsolution phases (intra-oxide re-

627 equilibration), which can directly affect the concentration of elements in these minerals (Frost et al. 1988; Frost

628 1991; Frost & Lindsley 1992; Pang et al. 2007). Therefore, exsolution and/or re-equilibration within magnetite,

629 ilmenite and/or Al-spinel must be considered when interpreting the cryptic layering in these minerals as indicator

630 of magmatic crystallization conditions.

Magnetite and hemo-ilmenite at Lac à l'Orignal have both been affected by subsolidus re-equilibration, similar to that described for the ilmenite cumulates of the Tellnes Deposit (Charlier et al. 2007) and Bjerkrein Sokndal (Duchesne, 1972). At the grain-scale, coronas of Al-spinel (pleonaste) are commonly observed at the contact between ilmenite and magnetite (Fig.5). The Al_2O_3 and MgO content of magnetite and ilmenite vary in the same way indicating an alteration of a primary ilmenite/magnetite chemical composition to generate Al-spinel grains. Also, the proportion of hematite exsolutions in ilmenite is locally reduced when magnetite is present, with the hematite content (Fe_2O_3) of ilmenite decreasing towards the margin with magnetite (Figs.5b & 5f). This is explained by a two-step process: the first step is the exsolution of pleonaste in magnetite most notably at the border of the grains. The exsolutions are incorporated, in a second step, to the ilmenite grain by the formation of new ilmenite at the contact of magnetite-ilmenite. This new ilmenite is formed by oxidation of the ulvöspinel component of magnetite. The oxidation is caused by reaction with the hematite contained in the ilmenite (Buddington & Lindsley, 1964, Duchesne, 1972). Because of this process, Al_2O_3 and MgO from magnetite are incorporated as pleonaste in ilmenite and the TiO_2 content of magnetite and the hematite content of ilmenite both decreases. According to Frost et al. (1988), the smaller proportion of magnetite relative to ilmenite means that this reaction has mainly changes the primary composition of magnetite into a Ti-poor variety, without significantly affecting the composition of the ilmenite.

At Lac à l'Orignal, there is a marked but gradual change in the oxide mineralogy from the border (hemo-ilmenite) towards the core of the intrusion (ilmenite). We attribute this to varying degrees of subsolidus re-equilibration between hemo-ilmenite and magnetite, resulting in the decrease of hematite exsolutions, as previously described, with less re-equilibration at the border and more in the core of the intrusion. Therefore, it is crucial to better understand how much inter-oxide re-equilibration has influenced the concentration/distribution of key trace elements, such as V, Cr and Ni between the different oxide phases.

High resolution element mapping, using LA-TOF-ICP-MS (Fig.12, ESM1), was performed at the contact area between magnetite and hemo-ilmenite, where it is evident that subsolidus, inter-oxide re-equilibration has occurred. In this example, the hemo-ilmenite "core'' portion, which is not in contact with magnetite, preserves more hematite exsolutions than the ilmenite "edge", in contact with magnetite. Also, fine-grained exsolutions of ilmenite (enriched in Ti, Sc, Mn; depleted in Fe and V) and pleonaste (enriched in Al and Co; depleted in V and Sc) in magnetite and at the edge of ilmenite are visible using the TOF mapping technique.

The inter-oxide re-equilibration at the contact of hemo-ilmenite and magnetite causes a depletion of Fe and a relative increase of Ti content of ilmenite at the edge in comparison with ilmenite in the core which is dominated by hematite exsolutions. There is no significant difference (Relative Difference (RD) < 15%, which is within precision of analyses) between the hematite-rich core and the hematite-poor edge for Ni, Co, Mn, Sc and Mg (Fig.12). Although V and Cr concentrations show significant differences, with a strong depletion (RD 20-50%) in ilmenite from the core (e.g., 54 ppm Cr) towards the edge of the grain (e.g., 40 ppm Cr) in contact with magnetite, this difference is relatively small compared to the variation between the different samples shown in Figure 12 (e.g., Cr varies from 200 to 1 ppm). Sub-solidus reequilibration of magnetite at the border with ilmenite had an even less of an effect on the primary composition of magnetite for most elements including Cr, Ni and V (RD<15%) especially in relation with the Ti content that increases from the core to the edge portion. Therefore, inter-oxide reequilibration might have influenced some of the geochemical variation of major and trace elements between ilmenite and magnetite, especially for V concentrations of ilmenite.

A series of binary diagrams comparing the V, Cr and Ni contents of magnetite and ilmenite (Fig.11) should therefore exhibit positively correlated differentiation trends if the cumulates were unmodified by inter-oxide reequilibration as they reflect the evolving composition of the parental magma during differentiation (Charlier et al. 2008; Polivchuk, 2017). This is the case at the Grader intrusion, where the V and Cr contents of ilmenite are well correlated (Fig.11b), with the slope of the trend varying according to their respective partition coefficients (Charlier et al. 2008). The hemo-ilmenite dominated Grader intrusion hosts much less magnetite (< 5% cumulus magnetite) in comparison with Lac à l'Orignal (10 – 15% cumulus magnetite), resulting in negligible inter-oxide reequilibration. However due to the presence of substantial magnetite with hemo-ilmenite at Lac à l'Orignal, inter-oxide reequilibration is probably more important (Fig.12), resulting in larger scatter for some of these differentiation trends (Figs.11 & ESM3). In detail, the V, Cr and Ni contents of magnetite (Fig.11a) are fairly well correlated with relatively low dispersion. In particular, the correlation of V and Cr of magnetite from both border and core of Lac à l'Orignal is similar to that of Grader. The Cr and Ni contents of ilmenite (Fig.11b) also show good correlation and relatively low dispersion. In contrast, the behaviour of V in ilmenite is different to that of magnetite: for hemo-ilmenite the V-Cr trend is similar to that of Grader but with a lot of scatters. However, the V content of Fe-poor ilmenite is much lower and does not vary with Cr. There is a positive correlation between the V content of ilmenite and the hematite component (Xhm), and thus the amount of hematite exsolutions, in ilmenite (Fig.11c). The hematite component provides an Fe^{3+} site in (hemo)-ilmenite into which $V^{(3+, 4+, 5+)}$ can partition into more easily than the Fe^{2+} site in ilmenite. The enrichment of V in hematite exsolutions in ilmenite are visible from the TOF elemental mapping in Figure 12.

Therefore, the hematite component of ilmenite, which is affected by subsolidus re-equilibration, directly controls the V content of ilmenite, thus resulting in large scatter for our samples from Lac à l'Orignal. Finally, the diagram Xhm vs Ilm/Mt ratio (Fig.11c) confirms that the hematite component in ilmenite is related in part to the abundance of, and thus inter-oxide exchange with magnetite: hemo-ilmenite bearing samples at the border of the Lac à l'Orignal mineralized zones have slightly lower magnetite concentrations (higher ilm/mt rations) in comparison with the ilmenite-bearing core, which has more magnetite and lower ilm/mt ratio.

On the diagram XHm vs. V content of ilmenite (Fig.11c), some of the OAN border samples (with larger hematite exsolutions and higher-V contents) plot close to the ilmenite from the fine-grained dykes (fast-cooled rocks) and could represent samples that also suffered a relatively fast-cooling history of crystallization, with negligible re-equilibration. In Figure 9c the higher Xhm content of ilmenite occurs at the very edges of the older borders of the intrusion (samples LO-01, 05, 55 & 57). It is known that sub-solidus re-equilibration processes are higher during long-cooling rates (Tanner et al. 2014). So, the hemo-ilmenite border samples with high-V contents probably suffered lower amounts of inter-oxide modification due to a faster cooling-rate and also a lower content of magnetite. Otherwise, the younger core of the intrusion, due to slower-cooling rates and/or higher amounts of magnetite, observed higher amounts of sub-solidus re-equilibration, consuming the hematite exsolutions and leading to a higher cationic exchange between magnetite and ilmenite. This difference in the cooling rates could be associated to different volume of magmas, the size of the different dykes/intrusions or even the difference of temperature between the new magma injection and the host-rocks (anorthosite and or/mineralized norites).

Insights on the petrogenesis of the Lac à l'Orignal Fe-Ti-P deposit

711   The Lac à l'Orignal deposit presents a complex history of evolution, being formed by at least two
712   different injections of similar ferrodiorite compositions but with different ages (border: 1069 ± 12 Ma and core:
713   993 ± 13 Ma). These cumulates were formed through fractional crystallization of a residual high-Ti-P magma
714   with oxide settling generating oxide-apatite norite cumulates, with occasional small nelsonite layers, and
715   plagioclase flotation generating apatite-bearing anorthosite layers (Fig.13). The oxide chemistry of the massive
716   oxides, hosted in andesine-anorthosite, has a more primitive signature. We thus suggest that the ferrodiorite
717   magmas, that formed the oxide-apatite norite cumulates were residual (evolved) liquids after extensive plagioclase
718   + oxide crystallization that formed the host anorthosites and massive oxides, respectively (Fig.13). A similar
719   petrogenetic model was applied for the two other Fe-Ti-(P) occurrences previously studied in the Grenville
720   Province: the Grader intrusion (OAGN and massive hemo-ilmenite) and the Lac Tio hemo-ilmenite deposit
721   (Charlier et al. 2008; 2010). However, in contrast, the Lac à l'Orignal deposit does not contain extensive massive
722   oxide cumulates within the mineralized zone as is the case for the Grader intrusion.

723   In detail, Figure 13 illustrates a schematic petrogenetic model for the formation of Fe-Ti-P mineralization
724   at Lac à l'orignal to illustrate the occurrence of multiple diapiric intrusions of different ages, each with their
725   respective residual Fe-Ti-P rich melts. Firstly, the Vanel Anorthosite (1080 ± 2 Ma) was emplaced and the residual
726   Fe-Ti-P-rich liquid (ferrodiorite) drained/filterpressed (Scoates et al. 2010; Charlier et al. 2015) into zones of
727   lower pressure (margins and or fractures) in the semi-consolidated anorthosite (plagioclase-rich mush diapir).
728   Fractional crystallization of plagioclase, orthopyroxene, hemo-ilmenite, magnetite and apatite, as cumulus phases
729   from the ferrodiorite liquid, formed the oxide-apatite norite (OAN) mineralization (1069 ± 12 Ma), nelsonite
730   (oxide + apatite settling) and apatite-bearing anorthosite (flotation of plagioclase-rich accumulation with
731   intergranular apatite) layers. Around 70Ma later, the younger Mattawa Anorthosite (1016 ± 2 Ma) was emplaced
732   nearby, probably using the same deep-crustal shear zones (e.g., Saint Fulgence Detachment Zone) that allowed
733   the Vanel Anorthosite diapirs to ascend. Similar processes of segregation and accumulation of ferrodiorite liquid
734   and emplacement of a younger OAN intrusion (993 ± 13 Ma) occurred forming the cumulates at the core of Lac
735   à l'Orignal, intruding the previous cumulates associated to Vanel Anorthosite. The younger cumulates in the core
736   (OAN and anorthosite-layers) evolved through similar fractionation processes, generating different cumulates due
737   to crystal settling/flotation. The higher amount of magnetite in the core (Fig. 13) probably led to a higher degree
738   of inter-oxide reequilibration (Fig.12) between the oxides in the core, resulting in ilmenite rather than hemo-
739   ilmenite that are dominant in the older borders.

740   Although Lac à l'Orignal shares some similarities with the Grader intrusion, the former contains higher
741   amounts of cumulus magnetite Along with the range of An content (extending to lower An) in plagioclase, higher
742   REE content in apatite as well as similar to lower Cr, Ni and V concentrations in the Lac à l'Orignal in comparison
743   to the Grader intrusion and Lac Tio (Figs.11 & ESM3), this denotes a more evolved character for the OAN
744   mineralization at Lac à l'Orignal. To illustrate this, whole rock Ti and Fe contents are plotted in Figure 11d and
745   show that overall, the Lac à l'Orignal cumulates have a lower Ti/Fe ratio (up to 12 wt.% TiO_2 in massive oxides),
746   in comparison with Lac Tio and the base of the Grader intrusion (up to 30 - 40 wt.% TiO_2 in massive oxides).
747   However, the OAGN of Grader plots between the two trends. The Ti/Fe reflects the relative proportion of their
748   main cumulate phases (hemo-ilmenite, ilmenite and magnetite), with a minor contribution of Fe coming from
749   orthopyroxene (low-abundance). The low-Ti/Fe trend of Lac à l'Orignal is due to lower proportions of ilmenite

and higher magnetite, whereas Lac Tio and Grader intrusion form a high-Ti/Fe trend with hemo-ilmenite-rich cumulates containing much lower proportions of magnetite. Using Cr in ilmenite to trace the degree of differentiation in Figure 11e, it is clear that the Ti/Fe ratio decreases from high-Ti/Fe systems (dominated by hemo-ilmenite only) to low-Ti/Fe systems (hemo-ilmenite and magnetite) with fractional crystallization, i.e., that Ti behaves as a compatible element due to the extensive crystallization of hemo-ilmenite from the Ti-rich melt. Petrogenetically, Lac Tio and the base of the Grader intrusion could be part of a high-Ti system in the Grenville Province (Fig.11d), forming from a more primitive melt, with high Ti/Fe ratio and high-Cr-V in ilmenite, dominated by massive ilmenite and ilmenite-rich norite cumulates, with low-magnetite concentrations and absence of apatite-bearing cumulates. The Grader intrusion would correspond to a transition from the high-Ti/Fe to the low-Ti/Fe system during continued fractional crystallization in response to decreasing Ti/Fe ratio, with the appearance of cumulus apatite forming massive nelsonite layers as well as minor cumulus magnetite generating oxide-apatite norite cumulates at the top part of the succession (Charlier et al. 2008). The OAN-dominated Lac à l'Orignal deposit, part of a low-Ti/Fe system, with the lowest Ti/Fe ratios, represents the most evolved, oxide-apatite norite cumulates, due to the presence of hemo-ilmenite + magnetite + apatite as first liquidus phases, in the late stages of differentiation of ferrodiorite/jotunite magmas. Similar features are also observed in the uppermost megacyclic units of the Bjerkreim-Sokndal Layered Intrusion (Duchesne & Charlier, 2005), where a progressive upward evolution is present from ilmenite-bearing cumulates to ilmenite-magnetite-bearing cumulates, being the appearance of cumulus magnetite due to fractional crystallization.

Conclusions

The Lac à l'Orignal Fe-Ti-P deposit is a multi-stage intrusion dominated by oxide-apatite norite cumulates where the marked feature is the change in the oxide mineralogy from hemo-ilmenite (+ minor magnetite) at the older border (1069 ± 12 Ma) to Fe-poor ilmenite + magnetite towards the younger core (993 ± 12 Ma). Although core and border have different ages, their range of ages are coeval with those previously described for the two youngest AMCG magmatic events in the region, and both cumulates have been generated under similar high-fO_2 conditions. Both intrusions were derived from high-Ti-P ferrodiorite magmas with similar REE compositions that evolved through extensive crystallization of hemo-ilmenite, magnetite and apatite. Petrogenetically, the Lac à l'Orignal Fe-Ti-P deposit corresponds to an evolved part of a low-Ti/Fe system in the Grenville Province, evolved through extensive crystallization of ilmenite, and further magnetite, in the late stages of differentiation of ferrodiorite/jotunite magmas.

The variation and spatial distribution of hemo-ilmenite (Xhem) between the border and core of Lac à l'Orignal must account for higher amounts of magnetite at the core of the intrusion (more evolved) in relation to border (more primitive). Border and core have had variable degrees of subsolidus inter-oxide re-equilibration, which had influence on the compositional evolution of the analyzed cumulates, especially within the core portion, modifying its original composition.

The variation of trace-elements in oxides and apatite as well as new U-Pb ages for Fe-Ti-rich mineralized rocks at Lac à l'Orignal, indicate the complex petrogenesis of oxide-apatite mineralization related to anorthosite-massifs in the Central Grenville Province. Understanding the petrogenesis of Fe-Ti-P mineralization and their relationship to the host AMCG suite is essential for helping to predict the occurrence of similar deposits in nearby locations, which can guide exploration efforts, saving time and resources.

References

Andersen, D.J., Lindsley, D.H., Davidson, P.M., 1993. QUIlF: a PASCAL program to assess equilibria among Fe–Mg–Ti oxides, pyroxenes, olivine, and quartz. Computers & Geosciences 19, 1333–1350.

Arguin J-P, Pagé P, Barnes S-J, Girard R, Duran C. 2018. An Integrated Model for Ilmenite, Al-Spinel, and Corundum Exsolutions in Titanomagnetite from Oxide-Rich Layers of the Lac Doré Complex (Québec, Canada). Minerals. 2018; 8(11):476.

Ashwal, LD., 1993. Anorthosites. Springer, Heidelberg.

Ashwal, L. D. 2010. The temporality of anorthosites. The Canadian Mineralogist, 48(4), 711-728.

Barnes, S. J., Maier, W. D., & Ashwal, L. D. 2004. Platinum-group element distribution in the main zone and upper zone of the Bushveld Complex, South Africa. Chemical Geology, 208(1-4), 293-317.

Barnes, S. J., Mansur, E. T., Pagé, P., Meric, J., & Arguin, J. P. 2020. Major and trace element compositions of chromites from the Stillwater, Bushveld and Great Dyke intrusions compared with chromites from komatiites, boninites and large igneous provinces.

Buddington, A. F., & Lindsley, D. H. 1964. Iron-titanium oxide minerals and synthetic equivalents. Journal of petrology, 5(2), 310-357.

Bybee, G. M., & Ashwal, L. D. 2015. Isotopic disequilibrium and lower crustal contamination in slowly ascending magmas: Insights from Proterozoic anorthosites. Geochimica et Cosmochimica Acta, 167, 286-300.

Cawthorn, R. G. 2007. Cr and Sr: Keys to parental magmas and processes in the Bushveld Complex, South Africa. Lithos, 95(3-4), 381-398.

Charlier, B., Grove, T.L., 2012. Experiments on liquid immiscibility along tholeiitic liquid lines ofdescent Contrib. Mineral. Petrol. 164 (1), 27-44

Charlier, B., Vander Auwera, J., & Duchesne, J. C. 2005. Geochemistry of cumulates from the Bjerkreim–Sokndal layered intrusion (S. Norway): Part II. REE and the trapped liquid fraction. Lithos, 83(3-4), 255-276.

Charlier, B., Duchesne, J.-C., Vander Auwera, J., 2006. Magma chamber processes in the Tellnes ilmenite deposit (Rogaland Anorthosite Province, SW Norway) and the formation of Fe–Ti ores in massif-type anorthosites. Chemical Geology 234, 264–290.

Charlier, B., Skar, O., Korneliussen, A., Duchesne, J.-C., Vander Auwera, J., 2007. Ilmenite composition in the Tellnes Fe–Ti deposit, SW Norway: fractional crystallization, postcumulus evolution and ilmenite–zircon relation. Contributions to Mineralogy and Petrology 154, 119–134.

Charlier, B., Sakoma, E., Sauve, M., Stanaway, K., Vander Auwera, J., Duchesne, J.-C., 2008. The Grader layered intrusion (Havre-Saint-Pierre Anorthosite, Quebec) and genesis of nelsonite and other Fe–Ti–P ores. Lithos 101, 359–378.

Charlier, B., Namur, O., Duchesne, J.-C., Wiszniewska, J., Parecki, A., Vander Auwera, J., 2009. Cumulate origin and polybaric crystallization of Fe–Ti oxide ores in the Suwalki anorthosite, Northeastern Poland. Economic Geology 104, 205–221.

Charlier, B., Namur, O., Malpas, S., de Marneffe, C., Duchesne, j.C., Vander Auwera, J., Bolle, O, 2010b. Origin ofthe giant Allard Lake ilmenite ore deposit (Canada) by fractional crystallization, multiple magma pulses and mixing. Lithos 117, 119-134.

Charlier B, Namur O, Bolle O, et al 2015. Fe-Ti-V-P ore deposits associated with Proterozoic massif type anorthosites and related rocks. Earth Science Reviews, 141:56–81. doi: 10.1016/j.earscirev.2014.11.005.

Chen, W., Zhou, M.-F., Zhao, T.-P., 2013. Differentiation of nelsonitic magmas in the formation of the - 1.74 Ga Damiao Fe-Ti-P ore deposit, North China. Contrib. Mineral. Petrol. 165, 1341-1362.

Coint, N., Keiding, J. K., & Ihlen, P. M. 2020. Evidence for silicate–liquid immiscibility in monzonites and petrogenesis of associated Fe–Ti–P-rich rocks: example from the Raftsund intrusion, Lofoten, Northern Norway. Journal of Petrology, 61(4).

Corriveau, L., Perreault, S., Davidson, A., 2007. Prospective metallogenic settings of the Grenville Province. In: Goodfellow, W.D. (Ed.), Mineral Deposits of Canada: a Synthesis of Major Deposit-types, District Metallogeny, the Evolution of Geological Provinces, and Exploration Methods: Geological Survey of Canada, Mineral Deposits Division, Special Publication, pp. 819–847.

Dare S.A, Barnes S-J, Beaudoin G, et al 2014. Trace elements in magnetite as petrogenetic indicators. Mineralium Deposita, 49:785–796.

Dare, S., Bethell, E., & Barnes, S. J. 2019. Constraining the formation of Fe-Ti-VP deposits using trace elements in Fe-Ti oxides: insights from the chemostratigraphic variation of magnetite and ilmenite in the Upper Zone of the Bushveld Igneous Complex. GAC-MAC-IAH Québec 2019.

Duchesne, J.C. 1972. Iron-titanium oxide minerais in the Bjerkrem-Sogndal Massif, South-western Norway. J. Petrol. 13, 57-81 .

Duchesne, J.C., Charlier, B., 2005. Geochemistry of cumulares from the Bjerkreim-Sokndal layered intrusion (S. Norway). Part 1: constraints from major elements on the mechanism of cumulate formation and on the jotunite liquid line of descent. Lithos, 83, 229-254.

Duchesne, J.C., Shumlyanskyy , L, Charlier, B., 2006. The Fedorivka layered intrusion (Korosten Pluton, Ukraine) : an example ofhighly differentiated ferrobasaltic evolution. Lithos 89, 353-376.

Dymek, R.F., Owens, B.E., 2001. Petrogenesis of apatite-rich rocks (nelsonites and oxide apatite gabbronorites) associated with massif anorthosites. Economic Geology 96, 797–815.

Emslie, R.F., 1985. Proterozoic anorthosite massifs. In: Tobi, A.C., Touret, J.L.R. (Eds.), The Deep Proterozoic Crust in the North Atlantic Provinces. Reidel, Dordrecht, pp. 39–60.

Frost, B. R. & Lindsley, D. H. 1992. Equilibria among Fe-Ti oxides, pyroxenes, olivine, and quartz: Part I. Theory. American Mineralogist, 77(9-10), 987-1003.

Frost, B. R. (1991). Magnetic petrology: factors that control the occurrence of magnetite in crustal rocks. Reviews in Mineralogy and Geochemistry, 25(1), 489-509.

Frost, B.R., Lindsley, D.H., Andersen, D.J, 1988. Fe-Ti oxide-silicate equilibria: assemblages with fayalitic olivine. Am. Mineral. 73, 727-740.

Frost, C. D., Frost, B. R., Lindsley, D. H., Chamberlain, K. R., Swapp, S. M., & Scoates, J. S. 2010. Chemical and isotopic evolution of the anorthositic plutons of the Laramie Anorthosite Complex: Explanations for variations in silica activity and oxygen fugacity of massif anorthosites. The Canadian Mineralogist, 48(4), 925-946.

Gobeil, A., Brisebois, D., Clark, T., Verpaelst, P., Madore, L., Wodicka, N., Cheve, S., 2003. Geologie de la moyenne Cote-Nord. In: Brisebois, D., Clark, T. (Eds.), Geologie et ressources minerales de la partie est de la Province de Grenville. Ministere des Ressources naturelles, de la Faune et des Parcs, Quebec, pp. 9–58. DV 2002-03.

Grant, M. 2020. Formation of magmatic Fe-Ti-V-P deposits within the Lac St. Jean area Saguenay, Québec, Canada: Insights from trace element composition of Fe-oxides and apatite. (Unpublished masters thesis). University of Ottawa, Ontario, Canada, pp. 343.

Hebert, C., Cadieux, A.-M., Van Breemen, O., 2005. Temporal evolution and nature of Ti– Fe–P mineralization in the anorthosite–mangerite–charnockite–granite (AMCG) suites of the South–central Grenville Province, Saguenay – Lac St. Jean area, Quebec, Canada. Canadian Journal of Earth Sciences 42, 1865–1880.

Hébert, C., Van Breemen, O., & Cadieux, A. 2009. Région du reservoir Pipmuacan, (SNRC 22E): Synthese Geologique. RG 2009-01. Ministère des ressources naturelles et de la faune, Gouvernement du Québec.

Higgins, M. D., & Van Breemen, O. 1992. The age of the Lac-Saint-Jean anorthosite complex and associated mafic rocks, Grenville Province, Canada. Canadian Journal of Earth Sciences, 29(7), 1412-1423.

Higgins, M.D., Van Breemen, O., 1996. Three generations of Anorthosite–Mangerite– Charnockite–Granite magmatism, contact metamorphism and tectonism in the Saguenay – Lac–St-Jean region, Grenville Province, Canada. Precambrian Research
79, 347–362.

Higgins, M. D., Ider, M., & Breemen, O. V. 2002. U-Pb ages of plutonism, wollastonite formation, and deformation in the central part of the Lac-Saint-Jean anorthosite suite. Canadian Journal of Earth Sciences, 39(7), 1093-1105.

Hou, T., Charlier, B., Holtz, F., Veksler, I., Zhang, Z., Thomas, R., & Namur, O. (2018). Immiscible hydrous Fe–Ca–P melt and the origin of iron oxide-apatite ore deposits. Nature communications, 9(1), 1-8.

Irvine, T.N., 1982. Terminology for layered intrusions. Journal of Petrology 23 (2), 127–162.

Jensen, J. C., Nielsen, F. M., Duchesne, J. C., Demaiffe, D., & Wilson, J. R. 1993. Magma influx and mixing in the Bjerkreim-Sokndal layered intrusion, South Norway: evidence from the boundary between two megacyclic units at Storeknuten. Lithos, 29(3-4), 311-325.

Klemme, S., Gunther, D., Hametner, K., Prowatke, S., Zack, T., 2006. The partitioning of trace elements between ilmenite, ulvospinel, armalcolite and silicate melts with implications for the early differentiation of the moon. Chemical Geology 234, 251–263.

Kieffer, M. A., Dare, S. A., & Namur, O. (2022). The use of trace elements in apatite to trace differentiation of a ferrobasaltic melt in the Sept-Iles Intrusive Suite, Quebec, Canada: Implications for provenance discrimination. *Geochimica et Cosmochimica Acta*.

Lattard, D., Sauerzapf, U., Kasemann, M., 2005. New calibration data for the Fe-Ti oxide thermo-oxybarometers from experiments in the Fe-Ti-O system at 1 bar, 1,000- 1,300 ºC and a large range of oxygen fugacities . Contrib . Mineral. Petrol. 149, 735-754.

Laverdière, G. 2013. Rapport de travaux d'exploration. Propriété Lac Orignal, Région du Saguenay-Lac Saint Jean. Glen Eagle Resources Inc.

Laverdiere, G. 2016. Rapport de travaux d'exploration. Propriete Lac Original, Region du Saguneay-Lac Saint Jean. Glen Eagle Resources Inc.

Leeman, W. P., Ma, M. S., Murali, A. V., & Schmitt, R. A. 1978. Empirical estimation of magnetite/liquid distribution coefficients for some transition elements. Contributions to mineralogy and petrology, 65(3), 269-272.

Lin, L & Sawyer, E. 2019. Microstructure and compsotional changes across biotite-rich reaction selvedges around mafic schollen in a semppelitic diatexite migmatite. Journal of Metamorphic Geology, 37:539-566.

McLelland,J., Ashwal, L, Moore, L, 1994. Composition and petrogenesis of oxide-, apatiterich gabbronorites assoeiated with Proterozoic anorthosite massifs: examples from the Adirondack Mountains, New York. Contrib. Mineral. Petrol. 116, 225-238.

Mitchell, j.N., Scoates, j.S., Frost, C.D., Kolker, A., 1996 . The geochemical evolution of anorthosite residual magmas in the Laramie Anorthosite Complex, Wyoming.j. Petrol. 37, 637-660.

Morisset, C.-E., Scoates, J.S., Weis, D., Friedman, R.M., 2009. U–Pb and 40Ar/39Ar geochronology of the Saint-Urbain and Lac Allard (Havre-Saint-Pierre) anorthosites and their associated Fe–Ti oxide ores, Quebec: evidence for emplacement and slow cooling during the collisional Ottawan orogeny in the Grenville Province. Precambrian Research 174, 95–116.

Morisset, C.-E., Scoates,J.S., Weis, D., Sauve, M., Stanaway, K.J., 2010. Rutile-bearing ilmenite deposits associated with the Proterozoic Saint-Urbain and Lac Allard anorthosite massifs, Grenville Province, Québec. Can. Mineral. 48, 821-849.

Morse, S. A. 1982. A partisan review of Proterozoic anorthosites. American Mineralogist, 67(11-12), 1087-1100.

Namur, O., Charlier, B., Toplis, M. J., Higgins, M. D., Liégeois, J. P., & Vander Auwera, J. 2010. Crystallization sequence and magma chamber processes in the ferrobasaltic Sept Iles layered intrusion, Canada. Journal of Petrology, 51(6), 1203-1236.

Namur, O., Charlier, B., Holness, M.B., 2012. Dual origin of Fe-Ti-P gabbros by immiscibility and fractional crystallization of evolved tholeiitic basalts in the Sept Iles layered intrusion. Lithos 154, 100-114.

Owens, B.E., Dymek, R.F., 1992. Fe-Ti-P-rich rocks and massif anorthosite: problems of interpretation illustrated from the Labrieville and St-Urbain plutons, Quebec. Can. Mineral. 30, 163-190

Owens, B.E., Dymek, R.F., 2005. Rediscovery of the Mattawa anorthosite massif, Grenville Province, Quebec. Canadian Journal of Earth Sciences 42, 1699–1718.

Owens, B.E., Rockow, M.W., Dymek, R.F., 1993. Jotunites from the Grenville Province, Quebec: petrological characteristics and implications for massif anorthosite petrogenesis. Lithos 30, 57–80.

Pang, K.-N., Li, C., Zhou, M.-F., Ripley, E.M., 2007. Abundant Fe–Ti oxide inclusions in olivine from the Panzhihua and Hongge layered intrusions, SW China: evidence for early saturation of Fe–Ti oxides in ferrobasaltic magma. Contributions to Mineralogy and Petrology 156, 307–321.

Perrot, M., Tremblay, A., & David, J. (2017). Detrital zircon U-Pb geochronology of the Magog Group, southern Quebec–stratigraphic and tectonic implications for the Quebec Appalachians. American Journal of Science, 317(10), 1049-1094.

Philpotts, A.R., 1967. Origin of certain iron-titanium oxide and apatite roeks. Econ. Geol. 62, 303-315.

Philpotts, A.R., 1982. Compositions of immiscible liquids in volcanic roeks. Contrib. Mineral. Petrol. 80, 201-218.

Polivchuk, M., & Dare, S. A. S. (2017). The formation of vanadium deposits of the Archean Bell River Complex, Quebec, Canada: Insights from Fe Ti oxide chemistry.

Rivers, T., 1997. Lithotectonic elements of the Grenville Province: review and tectonic implications. Precambrian Research 86, 117–154.

Scoates, J.S., Lindsley, D.H., Frost, B.R., 2010. Magmatic and structural evolution of an anorthositic magma chamber: the Poe Mountain intrusion, Laramie Anorthosite complex, Wyoming. Can. Mineral. 48, 851-885.

Slagstad, T., Henderson, I. H., Roberts, N. M., Kulakov, E. V., Ganerød, M., Kirkland, C. L. & Coint, N. 2022. Anorthosite formation and emplacement coupled with differential tectonic exhumation of ultrahigh-temperature rocks in a Sveconorwegian continental back-arc setting. *Precambrian research*, *376*, 106695.

Snyder, D., Carmichael, l.S.E., Wiebe, RA., 1993. Experimental study of liquid evolution in an Fe-rich, layered mafic intrusion: constrains of Fe-Ti oxide precipitation on the T-}02 and T-p paths of tholeiitic magmas. Contrib. Mineral. Petrol. 113, 73-86.

Tanner, D., Mavrogenes, J. A., Arculus, R. J., & Jenner, F. E. 2014. Trace element stratigraphy of the Bellevue Core, Northern Bushveld: multiple magma injections obscured by diffusive processes. Journal of Petrology, 55(5), 859-882.

Tegner, C., Cawthorn, R. G., & Kruger, F. J. 2006. Cyclicity in the Main and Upper Zones of the Bushveld Complex, South Africa: crystallization from a zoned magma sheet. Journal of Petrology, 47(11), 2257-2279.

Tollari, N., Barnes, S. J., Cox, R. A., & Nabil, H. 2008. Trace element concentrations in apatites from the Sept-Îles Intrusive Suite, Canada—implications for the genesis of nelsonites. Chemical Geology, 252(3-4), 180-190.

Toplis, MJ., Dingwell, D., Libourel, G., 1994a. The effect of phosphorous on the iron redox ratio, viscosity, and density of an evolved ferrobasalt. Contrib. Mineral. Petrol. 117, 293-304 .

Toplis, M. J., Libourel, G., & Carroll, M. R. 1994b. The role of phosphorus in crystallisation processes of basalt: an experimental study. Geochimica et Cosmochimica Acta, 58(2), 797-810.

Toplis, MJ, Carroll, M.R., 1995. An experimental study of the influence of oxygen fugacity on Fe-Ti oxide stability, phase relations, and mineral-melt equilibria in ferro-basaltic systems. J. Petrol. 36, 1137-1170.

Toplis, M., Corgne, A., 2002. An experimental study of element partitioning between magnetite, clinopyroxene and iron-bearing silicate liquids with particular emphasis on vanadium Contrib. Mineral. Petrol. 144, 22-37.

Toplis, M. J., & Dingwell, D. B. (1996). The variable influence of P2O5 on the viscosity of melts of differing alkali/aluminium ratio: Implications for the structural role of phosphorus in silicate melts. Geochimica et Cosmochimica Acta, 60(21), 4107-4121.

1069 Vander Auwera, J., Longhi, J., 1994. Experimental study of a jotunite (hypersthene monzodiorite) : constraints
1070 on the parent magma composition and crystallization conditions (P, T,JO,) of the Bjerkreim-Sokndal layered
1071 intrusion (Norway) . Contrib. Mineral. Petrol. 118, 60-78.

1073 Vander Auwera, J., Longhi, J, Duchesne, J.C., 1998. A liquid line of descent of the jotunite (hypersthene
1074 monzodiorite) suite. J. Petrol. 39, 439-468.

1076 Vander Auwera, J., Weis, D., Duchesne,j.C., 2006. Marginal mafic intrusions as indicators of downslope draining
1077 of dense residual melts in anorthositic diapirs? Lithos 89, 329-352.

1079 Wilson, J. R., Robins, B., Nielsen, F. M., Duchesne, J. C., & Vander Auwera, J. (1996). The Bjerkreim-Sokndal
1080 layered intrusion, Southwest Norway. In Developments in Petrology (Vol. 15, pp. 231-255). Elsevi

1082 Yassa, A. 2022. Technical report and initial mineral resource estimate of the Lac Orignal phosphate property,
1083 Saguenay-Lac-Saint-Jean region, Northern Québec. First Phosphate Corp.

1086 **FIGURE CAPTIONS**

1088 Fig. 1 **a** Location of the Grenville Province in Quebec, Canada. Red square represents the Central Grenville shown
1089 in "b". **b** Regional geological map of the AMCG suites in the Central Grenville Province, Quebec with the location
1090 of the Fe-Ti-(P) deposits and regional deformation zones (DZ). **c** Close up of the AMCG suites and Fe-Ti-(P)
1091 mineral deposits in the Lac à l'Orignal area. Red dotted lines indicate the inferred limit between core (CZ) and
1092 border (BZ) of the Mattawa Anorthosite Massif, according to Owens & Dymek (2005), based on geochemical
1093 criteria. Geological maps modified from SIGEOM (Quebec System of Geomining Information). **d-e** Schematic
1094 geology sections of the Lac à l'Orignal Fe-Ti-P deposit: **d** N-S section showing the oxide-apatite mineralized zone
1095 (average P_2O_5 around 5 wt.%) hosted by anorthosite and leuconorite. Cut-off grade is 3 wt.%. (Laverdière, 2013;
1096 2016). **e** Schematic W-E section showing the approximate lens-shape of the mineralized zone, dipping around 30°
1097 to the north. The large thickness of the LO-14-21 drillcore was chosen for this study.

1099 Fig. 2 Photographs of representative lithologies of the Lac à l'Orignal Fe-Ti-P deposit from surface and drillcore.
1100 **a** Coarse-grained oxide-apatite-norite (OAN) (sample 20PM02). **b** Oxide-apatite-norite (LO-24, 28m). **c**
1101 Pegmatitic OAN (LO-41, 71m). **d** Layering of OAN with plagioclase-rich (anorthosite) layers. **e** Massive apatite
1102 layer within pink-anorthosite layers (LO-03, 5m). **f** Massive oxides (ilmenite + magnetite) containing blocks of
1103 the host-anorthosite (sample 20PM03). Mineral abbreviations: pl = plagioclase; opx = orthopyroxene; ox = oxides;
1104 ilm = ilmenite; ap = apatite.

1106 Fig. 3 Stratigraphic subdivision of the Lac à l'Orignal intrusion based on the distribution of different cumulus
1107 phases from the borders to the core. Modal proportion of oxides and apatite (left). Cryptic variation in plagioclase
1108 of anorthite (An) content (An=100 [Ca/ (Ca+Na)]) and TiO_2 and P_2O_5 values of whole-rock analysis are shown.
1109 Cumulus (-C) assemblages follow the nomenclature of Irvine (1982). Mineral abbreviations: p = plagioclase (pl);
1110 i = ilmenite (ilm); a = apatite (ap); h = orthopyroxene (opx); m = magnetite (mt); hm-ilm = hemo-ilmenite. Error
1111 bars = 1 standard deviation of the average value and represents the natural variation within the thin section.

1113 Fig. 4 Photomicrographs of the main lithologies of the Lac à l'Orignal Fe-Ti-P mineralized zone. **a** Medium-
1114 grained oxide-apatite-norite (OAN) (LO-24, 28m). **b** Pegmatitic coarse-grained OAN. Note the appearance of
1115 centimetric-scale orthopyroxene (LO-41, 71m). **c** Orthopyroxene megacrystal with rutile exsolution lamellae (LO-
1116 41, 71m). **d** Contact between medium-grained OAN and massive nelsonitic layer (LO-21, 20.8m). **e-f**
1117 Accumulation of apatite crystals within anorthosite layer (apatite-bearing anorthosite, LO-38, 62m) containing
1118 plagioclase with exsolutions of K-rich phase. (LO-38, 62m). **g** Massive apatite layer (LO-02, 4.7m). **h** Fine-
1119 grained OAN dyke (LO-06, 6.7m). **i** Coarse-grained host-anorthosite lacking apatite and exsolutions in plagioclase
1120 (LO-58, 105.3m). Mineral abbreviations: pl = plagioclase; opx = orthopyroxene; bt = biotite; hm-ilm = hemo-
1121 ilmenite; ilm = ilmenite; mt = magnetite; rt = rutile; ap = apatite; spl = Al-spinel; sulph = sulfides.

1122 Fig. 5 **a-d** μXRF-maps, combining P (white), Ti (blue) and Fe (green), showing the different proportions of oxides
1123 and apatite from the Lac à l'Orignal Fe-Ti-P mineralized zone. Ilmenite is blue, where as hematite-rich part of
1124 ilmenite is cyan. Magnetite is bright green. Orthopyroxene/biotite is dark green. **a** Medium grained-OAN
1125 dominated by hemo-ilmenite containing coarse exsolution lamellae of hematite, and minor magnetite (top border
1126 zone, LO-01, 3.7m). **b** Coarse grained-OAN dominated by hemo-ilmenite containing thin exsolution lamellae of
1127 hematite, and magnetite (transition zone, LO-22, 21.5m). **c** Medium grained-OAN dominated by magnetite and
1128 ilmenite (Hemo-ilmenite is absent) from core zone (LO-43, 75.7m). **d** Medium grained-OAN dominated by hemo-
1129 ilmenite, containing coarse exsolution lamellae of hematite, and minor magnetite, from the bottom border zone
1130 (LO-57, 102.1m). Note the higher presence of apatite near the oxide crystals. **e-h** Photomicrographs (reflected
1131 light) of the oxide assemblages. **e** Medium grained oxide-apatite norite (OAN) dominated by hemo-ilmenite
1132 containing coarse exsolution lamellae of hematite (pale) and ilmenite (dark) and minor magnetite (border zone,
1133 LO-10, 10.5m). **f** Medium grained-OAN dominated by hemo-ilmenite, with fine exsolutions of hematite, and
1134 ilmenite (exsolution-free) close to magnetite (transition zone, sample LO-24, 28m). **g** Medium grained-OAN
1135 dominated by magnetite, ilmenite and Al-spinel exsolutions. Hemo-ilmenite is absent (core zone, LO-32, 48.5m).
1136 **h** Evidence of sub-solidus re-equilibration between magnetite and ilmenite, with depletion of hematite exsolutions
1137 in ilmenite towards the border with magnetite. Note the higher presence of Al-spinel exsolutions at the contact
1138 between magnetite and ilmenite grains (LO-29, 42m). Mineral abbreviations: pl = plagioclase; opx =
1139 orthopyroxene; hm-ilm = hemo-ilmenite; ilm = ilmenite; mt = magnetite; ap = apatite; spl = Al-spinel; sulph =
1140 sulfides; bt = biotite.
1141
1142 Fig. 6 **a** Concordia diagrams for in situ LA-ICP-MS U–Pb data from analyzed zircons in the Lac à l'Orignal Fe-
1143 Ti-P mineralization. Each ellipse represents the result of the analysis of a single grain, as identified in Table 1,
1144 and corresponds to the associated 2σ uncertainties. **b** Representative cathodoluminescence images from detrital
1145 magmatic grains of zircon of the Lac à l'Orignal Fe-Ti-P mineralization in the Central Grenville Province, Quebec.
1146 Red circles show the location of the 50 μm beam for U–Pb microanalysis.
1147
1148 Fig. 7 Whole-rock variation diagrams for the Lac à l'Orignal Fe-Ti-P deposit with the major mineral compositions
1149 plotted from electron microprobe and SEM data. Mineral abbreviations: pl = plagioclase; opx = orthopyroxene;
1150 bt = biotite; hm-ilm = hemo-ilmenite; ilm = ilmenite; mt = magnetite; ap = apatite; spl = Al-spinel; hbl =
1151 hornblende. OAN = oxide-apatite-norite; Msv.oxides = massive oxides; Fine-grain. Dykes = fine-grained
1152 ferrodiorite dykes.
1153
1154 Fig. 8 Chondrite-normalized REE compositions of whole-rock samples (normalized to chondrite; Sun and
1155 McDonough, 1989). **a** Mineralized samples: border and core OAN, massive oxides and fine-grained dykes. **b**
1156 Comparison between anorthosite samples (host and apatite-bearing layers) and the mineralized OAN from Fig.
1157 8b (grey field). Mineral abbreviations: hm-ilm = hemo-ilmenite; ilm = ilmenite; mt = magnetite.
1158 Fig. 9 Stratigraphic variation of plagioclase (**a**), apatite (**b**), ilmenite (**c**) magnetite (**d**) compositions in drillcore
1159 LO-14-21. The grey horizon represents the nelsonite (iap-C) layer. The pink horizons represent the apatite-bearing
1160 anorthosite (pa-C) layers and the brownish horizon the host-anorthosite. Red lines indicate the oxide assemblage
1161 changing from Hm-ilmenite to Fe-poor ilmenite towards the core of the intrusion. Error bars = 1 standard deviation
1162 and represents the natural variation within the thin section. Mineral abbreviations: hm-ilm = hemo-ilmenite; ilm
1163 = ilmenite; mt = magnetite.
1164 Fig. 10 Chondrite-normalized REE compositions (after Sun and McDonough, 1989). **a** Apatite REE-data. **b**
1165 Whole-rock REE data in comparison with apatite (grey field – Fig.10-A) showing the REE behavior controlled
1166 by apatite concentration. **c** Apatite REE patterns for fine-grained OAN dykes (samples LO-06 and LO-08)
1167 compared to calculated liquids from the inversion of apatite compositions of border (orange lines) and core (blue
1168 lines) samples. Calculated liquids applying D*Ap REE* values obtained from bulk and apatite compositions of dyke
1169 sample LO-06.
1170
1171 Fig. 11 Binary diagrams displaying concentrations of compatible elements in magnetite (**a**) and ilmenite (**b**), using
1172 Cr as a proxy for fractional crystallization. **c** Hematite content in ilmenite in relation to the V concentration in

ilmenite (left) and the modal proportion of magnetite (right). Comparison between geochemical data of the Lac à l'Orignal Fe-Ti-P deposit (this work), the Grader intrusion Fe-Ti-P, Quebec (Charlier et al. 2008) and the world-class ilmenite deposit of Lac Tio Fe-Ti, Quebec (Charlier et al. 2010). **d-e** Geochemical comparison of the Lac à l'Orignal Fe-Ti-P deposit (blue field – this study) with the Lac Tio Ti deposit (red field) and the Fe-Ti-P mineralization at Grader intrusion (green field), in the Havre Saint Pierre Anorthosite, Quebec (data from Charlier *at al.* 2010; 2008). **e** Whole-rock Fe_2O_{3t} vs. TiO_2. **e** Ti/Fe whole rock ratio vs. Cr content of ilmenite (in ppm).

Fig. 12 Fully quantified, high resolution element maps, using LA-Time of Flight-ICP-MS, showing the distribution of some major and trace elements at the contact between ilmenite and magnetite crystals (sample LO-24). Any significant relative difference (%) in the element concentrations of selected core and edge areas in ilmenite and magnetite are due to sub-solidus, inter-oxide reequilibration. Red-yellow colors representing higher concentration of an element. Blue-white colors representing lower concentration.

Fig. 13 Schematic simplified model for the generation of Fe-Ti-P mineralization, exemplified by the Lac à l'Orignal Fe-Ti-P deposit in the Central Grenville Province. Fractionation of residual Fe-Ti-P rich ferrodiorite melts generated after anorthosite crystallization. **a** Multi-diapiric emplacement of mafic mantle-derived magmas forming the Pipmuacan AMCG suite (e.g. Vanel Anorthosite) favored by deep-seated shear zones like the Saint Fulgence Detachment Zone. Segregation of ferrodiorite residual liquids filter-pressed into fractures/zones of lower pressure, generating the accumulation of oxide-apatite cumulates in dykes/sill-like structures and/or around the anorthosite-massifs. **b** Emplacement and crystallization of the Valin AMCG suite and segregation of ferrodiorite residual magmas as previously described. Note that the intrusion of the Valin AMCG Suite within the previous Pipmuacan AMCG suite possibly the generation of conduits interconnecting different residual magma accumulation of different ages. **c** Fractionation of evolved Fe-Ti-P melts with apatite as a liquids phase, dominated by (hemo)-ilmenite + magnetite + apatite initially (older border), and subsequently dominated by ilmenite + magnetite + apatite (younger core). Formation of local oxide-apatite-rich layers (nelsonite) by settling; residual oxide-apatite-norite (apatite + apatite + silicates) and apatite-bearing anorthosite (plagioclase + apatite) by relatively flotation.

TABLE CAPTIONS

Table 1. Zircon U–Pb LA-ICP-MS analytical data of samples in hole LO-14-21 from the Lac à l'Orignal Fe-Ti-P deposit

Table 2. Representative LA-ICP-MS Whole-rock major and trace element compositions (by LA-ICP-MS) for samples from hole LO-14-21 I in the Lac à l'Orignal Fe-Ti-P deposit

Table 3. Representative LA-ICP-MS major and trace-elements analyses of plagioclase for samples from hole LO-14-21 in the Lac à l'Orignal Fe-Ti-P deposit

Table 4. Representative major and trace-elements LA-ICP-MS analyses of apatite for samples from the hole LO-14-21 in the Lac à l'Orignal Fe-Ti-P deposit

Table 5. Representative LA-ICP-MS major and trace-elements analyses of ilmenite for samples from hole LO-14-21 in the Lac à l'Orignal Fe-Ti-P deposit

Table 6. Representative LA-ICP-MS major and trace-elements analyses of magnetite for samples from the hole LO-14-21 in the Lac à l'Orignal Fe-Ti-P deposit

Table 7. REE concentrations of the fine-grained OAN dykes and respective calculated partition coefficients between apatite and melt
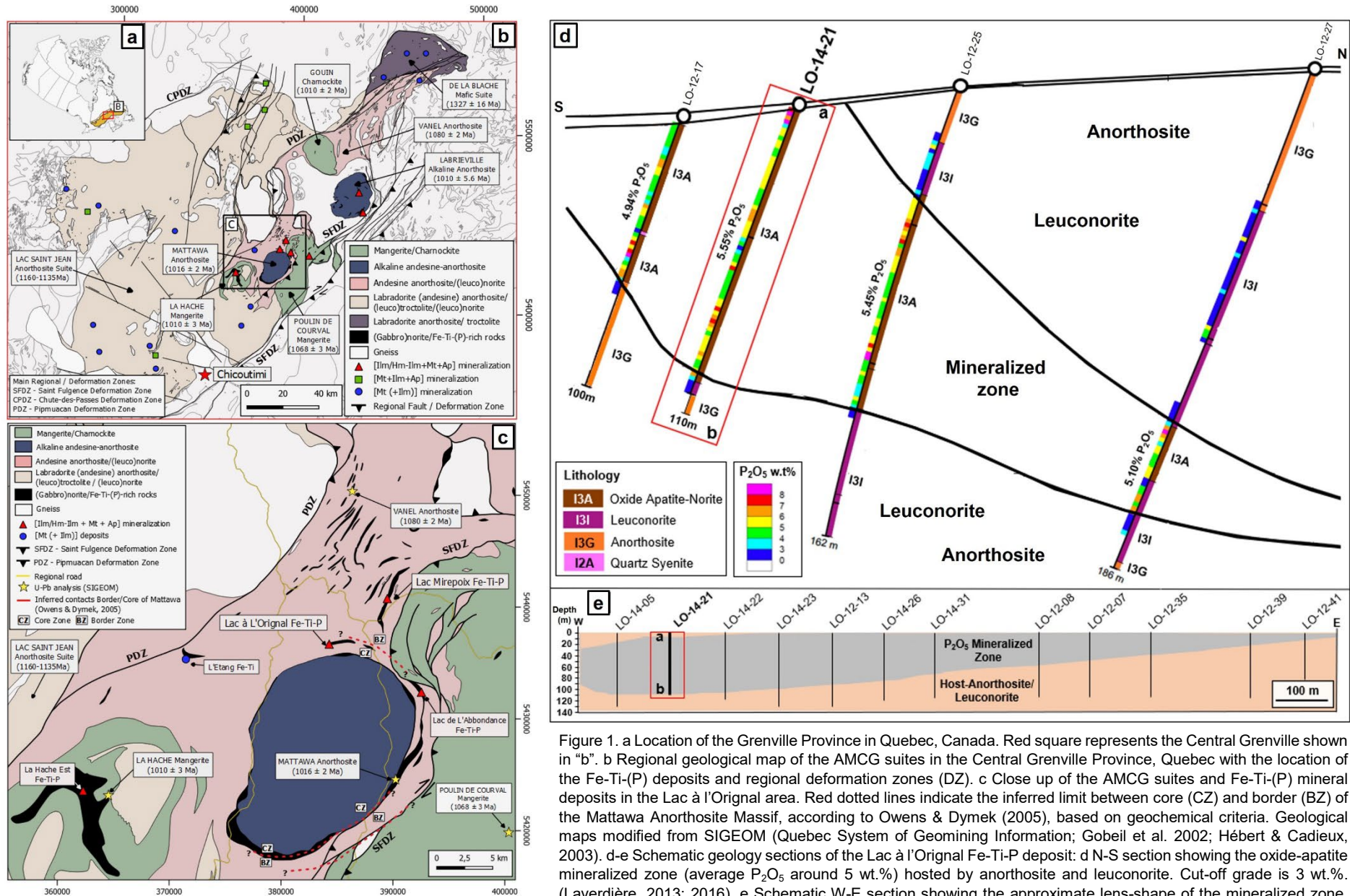
Figure 1. a Location of the Grenville Province in Quebec, Canada. Red square represents the Central Grenville shown in "b". b Regional geological map of the AMCG suites in the Central Grenville Province, Quebec with the location of the Fe-Ti-(P) deposits and regional deformation zones (DZ). c Close up of the AMCG suites and Fe-Ti-(P) mineral deposits in the Lac à l'Orignal area. Red dotted lines indicate the inferred limit between core (CZ) and border (BZ) of the Mattawa Anorthosite Massif, according to Owens & Dymek (2005), based on geochemical criteria. Geological maps modified from SIGEOM (Quebec System of Geomining Information; Gobeil et al. 2002; Hébert & Cadieux, 2003). d-e Schematic geology sections of the Lac à l'Orignal Fe-Ti-P deposit: d N-S section showing the oxide-apatite mineralized zone (average P_2O_5 around 5 wt.%) hosted by anorthosite and leuconorite. Cut-off grade is 3 wt.%. (Laverdière, 2013; 2016). e Schematic W-E section showing the approximate lens-shape of the mineralized zone, dipping around 30° to the north. The large thickness of the LO-14-21 drillcore was chosen for this study.
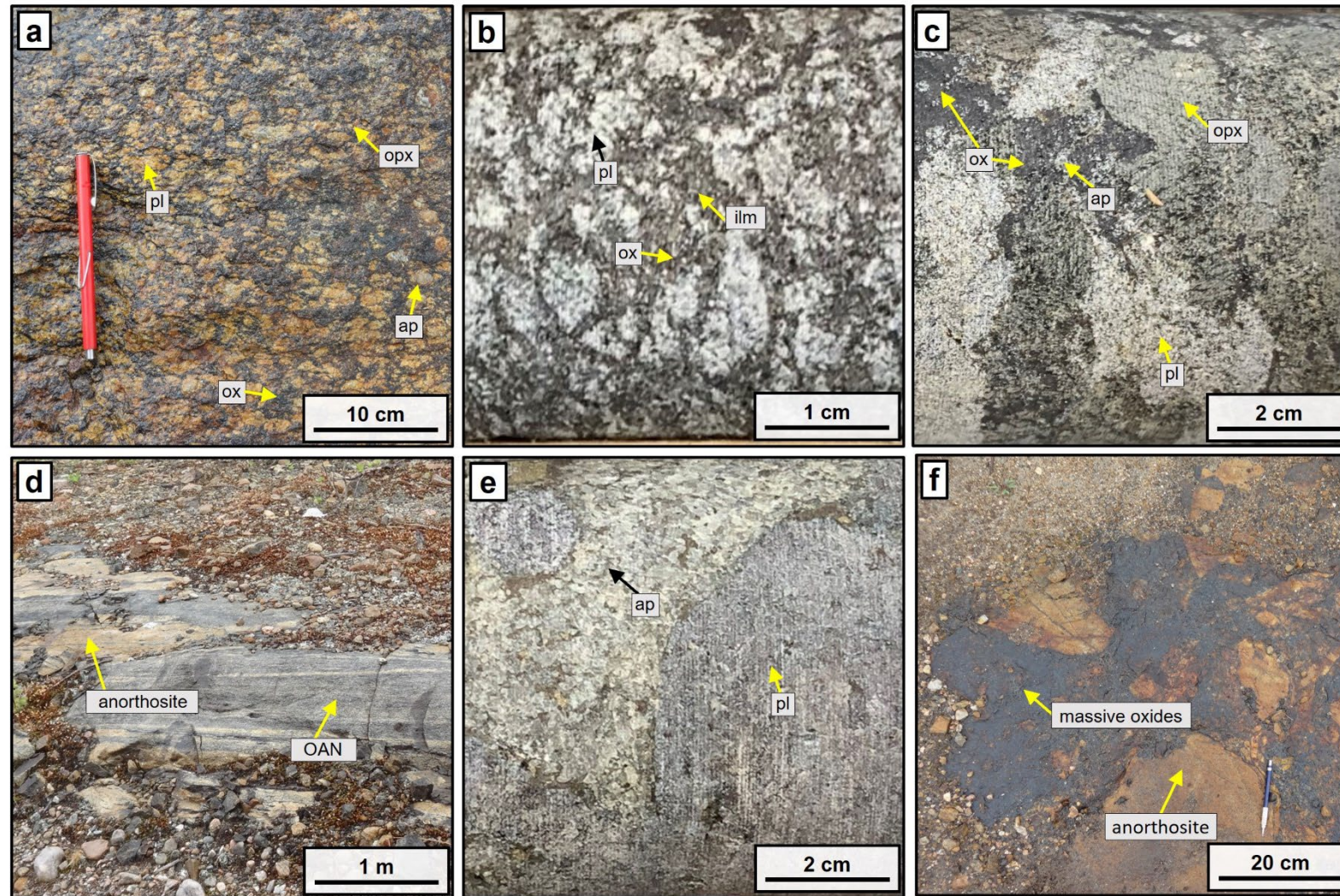
Figure 2. Photographs of representative lithologies of the Lac à l'Orignal Fe-Ti-P deposit from surface and drillcore. a Coarse-grained oxide-apatite-norite (OAN) (sample 20PM02). b Oxide-apatite-norite (LO-24, 28m). c Pegmatitic OAN (LO-41, 71m). d Layering of OAN with plagioclase-rich (anorthosite) layers. e Massive apatite layer within pink-anorthosite layers (LO-03, 5m). f Massive oxides (ilmenite + magnetite) containing blocks of the host anorthosite (sample 20PM03). Mineral abbreviations: pl = plagioclase; opx = orthopyroxene; ox = oxides; ilm = ilmenite; ap = apatite.

2
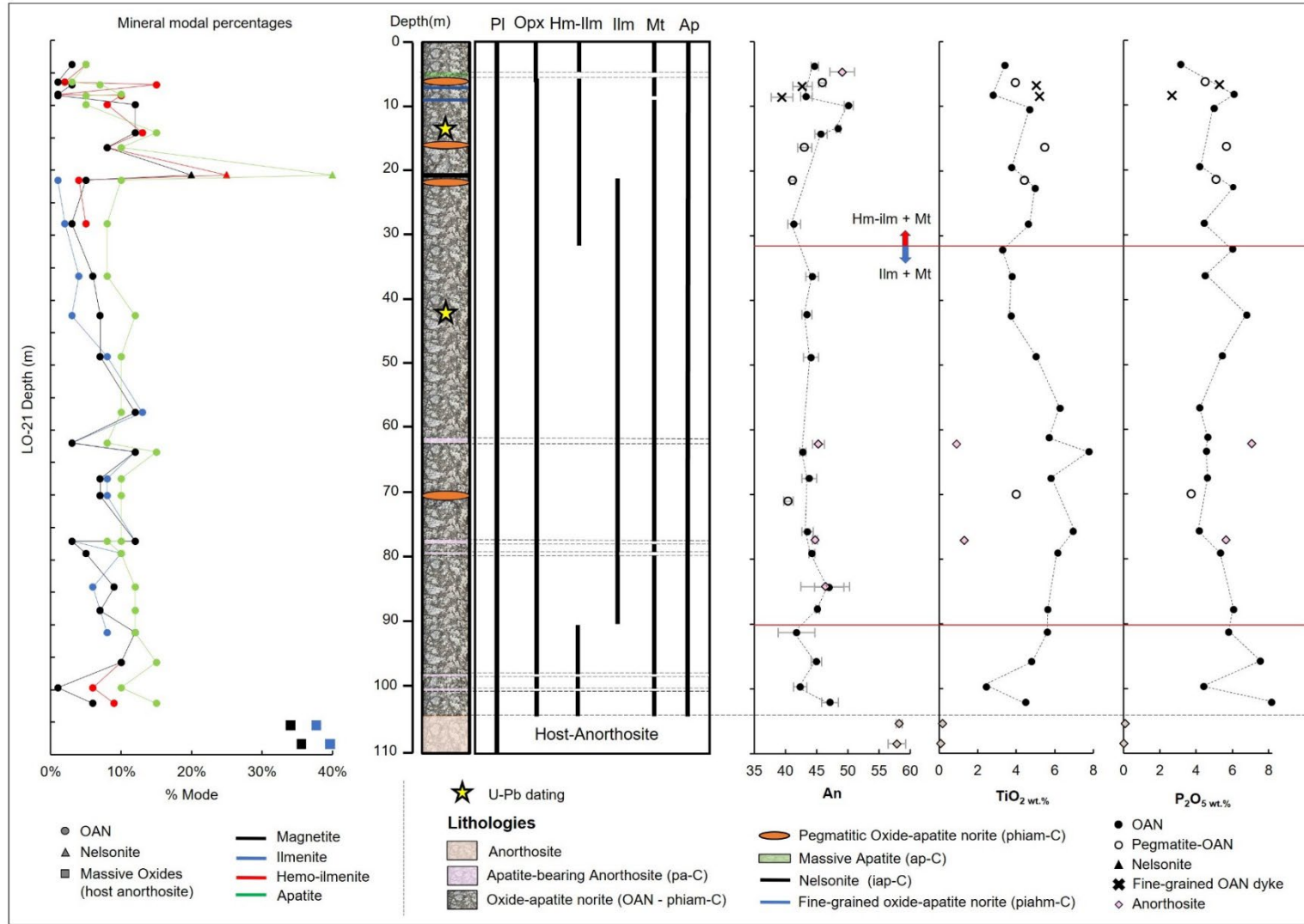
Figure 3. Stratigraphic subdivision of the Lac à l'Orignal intrusion based on the distribution of different cumulus phases from the borders to the core. Modal proportion of oxides and apatite (left). Cryptic variation in plagioclase of anorthite (An) content (An=100 [Ca/ (Ca+Na)]) and TiO$_2$ and P$_2$O$_5$ values of whole-rock analysis are shown. Cumulus (-C) assemblages follow the nomenclature of Irvine (1982). Mineral abbreviations: p = plagioclase (pl); i = ilmenite (ilm); a = apatite (ap); h = orthopyroxene (opx); m = magnetite (mt); hm-ilm = hemo-ilmenite. Error bars = 1 standard deviation of the average value and represents the natural variation within the thin section.

1292
1293
1294
1295
1296
1297
1298
1299
1300
1301
1302
1303
1304
1305
1306
1307
1308
1309
1310
1311
1312
1313
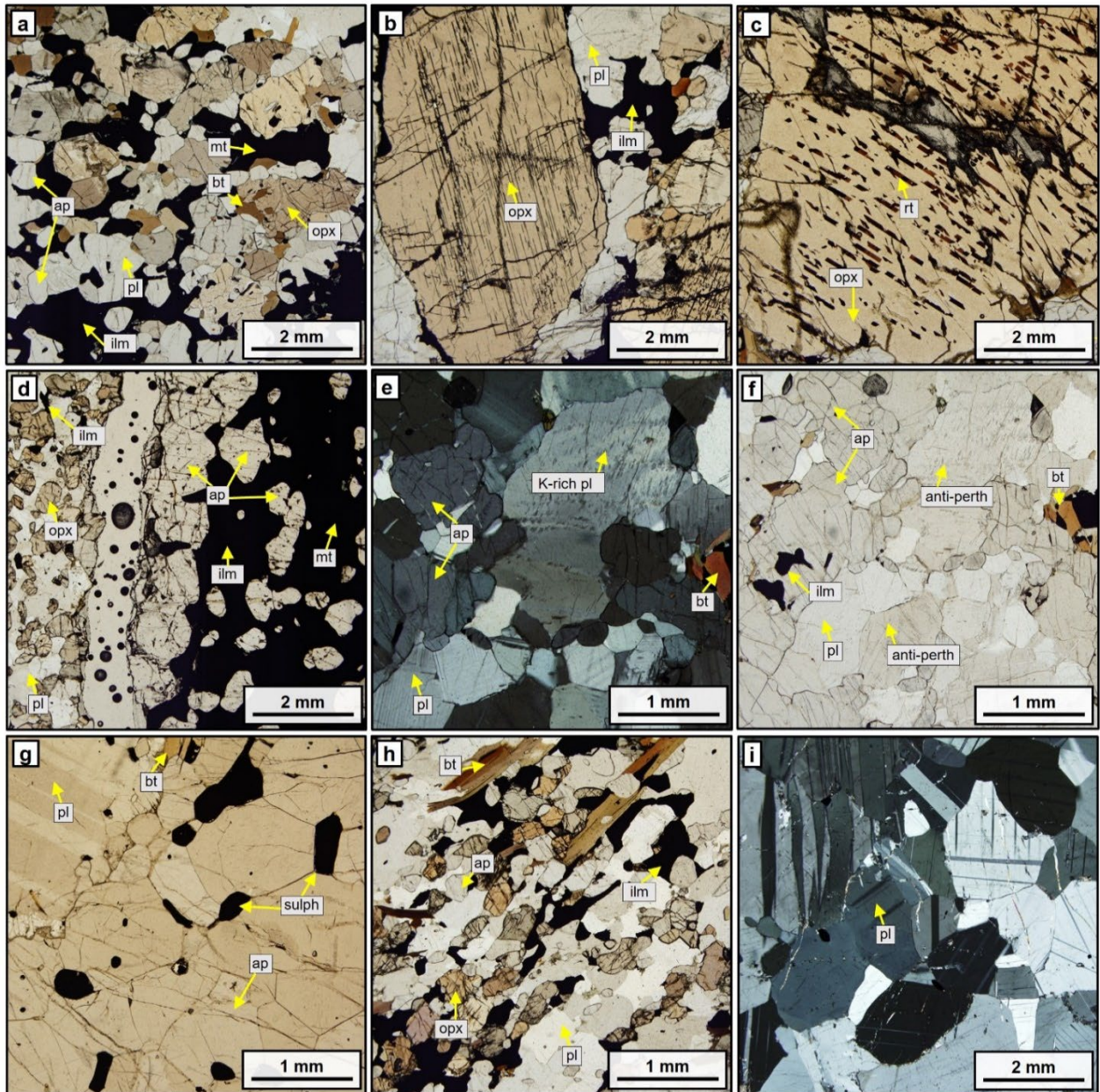
Figure 4. Photomicrographs of the main lithologies of the Lac à l'Orignal Fe-Ti-P mineralized zone. a Medium-grained oxide-apatite-norite (OAN) (LO-24, 28m). b Pegmatitic coarse-grained OAN. Note the appearance of centimetric-scale orthopyroxene (LO-41, 71m). c Orthopyroxene megacrystal with rutile exsolution lamellae (LO-41, 71m). d Contact between medium-grained OAN and massive nelsonitic layer (LO-21, 20.8m). e-f Accumulation of apatite crystals within anorthosite layer (apatite-bearing anorthosite, LO-38, 62m) containing plagioclase with exsolutions of K-rich phase. (LO-38, 62m). g Massive apatite layer (LO-02, 4.7m). h Fine-grained OAN dyke (LO-06, 6.7m). i Coarse-grained host anorthosite lacking apatite and exsolutions in plagioclase (LO-58, 105.3m). Mineral abbreviations: pl = plagioclase; opx = orthopyroxene; bt = biotite; hm-ilm = hemo-ilmenite; ilm = ilmenite; mt = magnetite; rt = rutile; ap = apatite; spl = Al-spinel; sulph = sulfides.

Figure 5. a-d μXRF-maps, combining P (white), Ti (blue) and Fe (green), showing the different proportions of oxides and apatite from the Lac à l'Orignal Fe-Ti-P mineralized zone. Ilmenite is blue, where as hematite-rich part of ilmenite is cyan. Magnetite is bright green. Orthopyroxene/biotite is dark green. a Medium grained-OAN dominated by hemo-ilmenite containing coarse exsolution lamellae of hematite, and minor magnetite (top border zone, LO-01, 3.7m). b Coarse grained-OAN dominated by hemo-ilmenite containing thin exsolution lamellae of hematite, and magnetite (transition zone, LO-22, 21.5m). c Medium grained-OAN dominated by magnetite and ilmenite (Hemo-ilmenite is absent) from core zone (LO-43, 75.7m). d Medium grained-OAN dominated by hemo-ilmenite, containing coarse exsolution lamellae of hematite, and minor magnetite, from the bottom border zone (LO-57, 102.1m). Note the higher presence of apatite near the oxide crystals. e-h Photomicrographs (reflected light) of the oxide assemblages. e Medium grained oxide-apatite norite (OAN) dominated by hemo-ilmenite containing coarse exsolution lamellae of hematite (pale) and ilmenite (dark) and minor magnetite (border zone, LO-10, 10.5m). f Medium grained-OAN dominated by hemo-ilmenite, with fine exsolutions of hematite, and ilmenite (exsolution-free) close to magnetite (transition zone, sample LO-24, 28m). g Medium grained-OAN dominated by magnetite, ilmenite and Al-spinel exsolutions. Hemo-ilmenite is absent (core zone, LO-32, 48.5m). h Evidence of sub-solidus re-equilibration between magnetite and ilmenite, with depletion of hematite exsolutions in ilmenite towards the border with magnetite. Note the higher presence of Al-spinel exsolutions at the contact between magnetite and ilmenite grains (LO-29, 42m). Mineral abbreviations: pl = plagioclase; opx = orthopyroxene; hm-ilm = hemo-ilmenite; ilm = ilmenite; mt = magnetite;
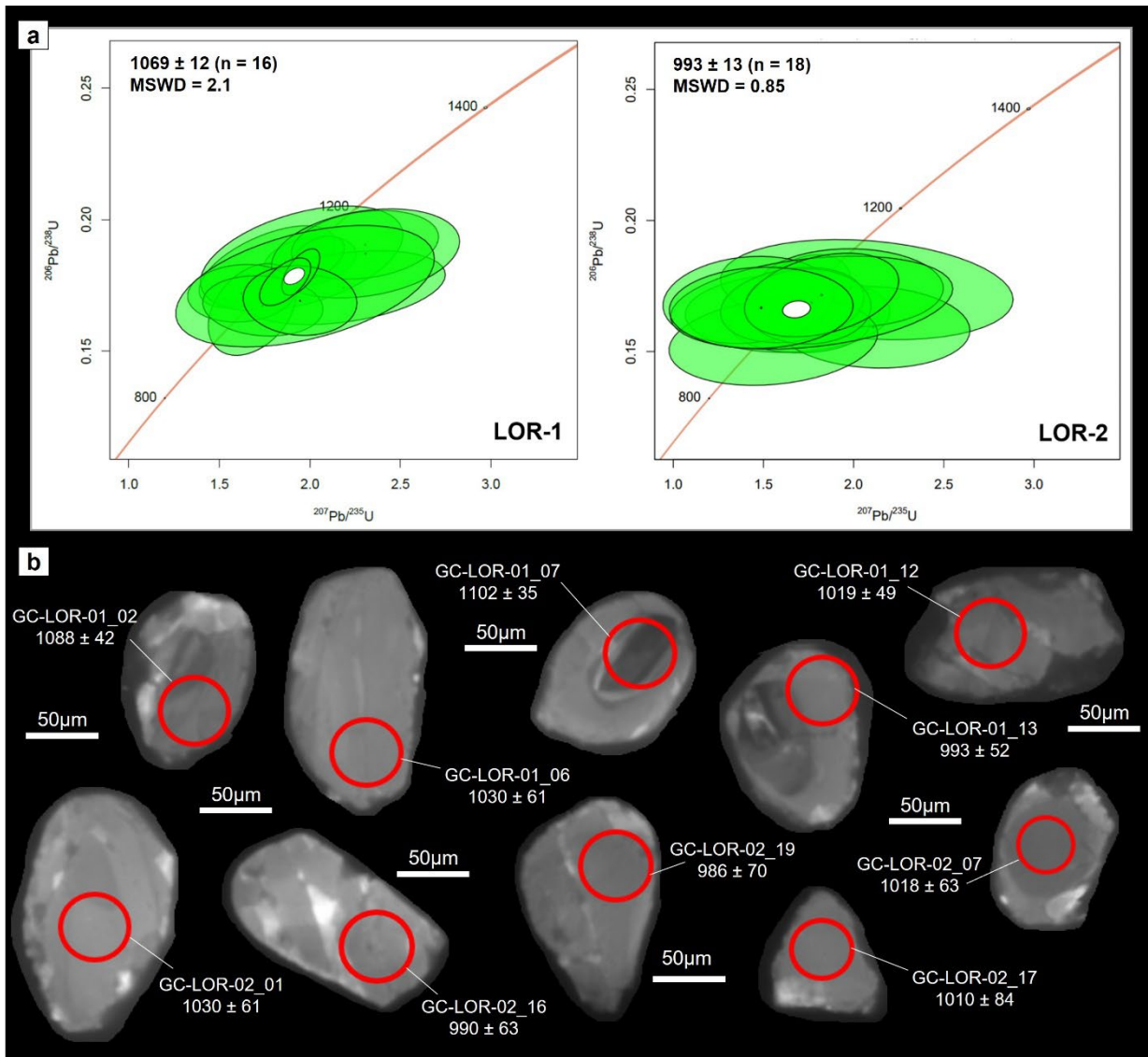
Figure 6. a Concordia diagrams for in situ LA-ICP-MS U–Pb data from analyzed zircons in the Lac à l'Orignal Fe-Ti-P mineralization. Each ellipse represents the result of the analysis of a single grain, as identified in Table 1, and corresponds to the associated 2σ uncertainties. b Representative cathodoluminescence images from detrital magmatic grains of zircon of the Lac à l'Orignal Fe-Ti-P mineralization in the Central Grenville Province, Quebec. Red circles show the location of the 50 μm beam for U–Pb microanalysis.

3
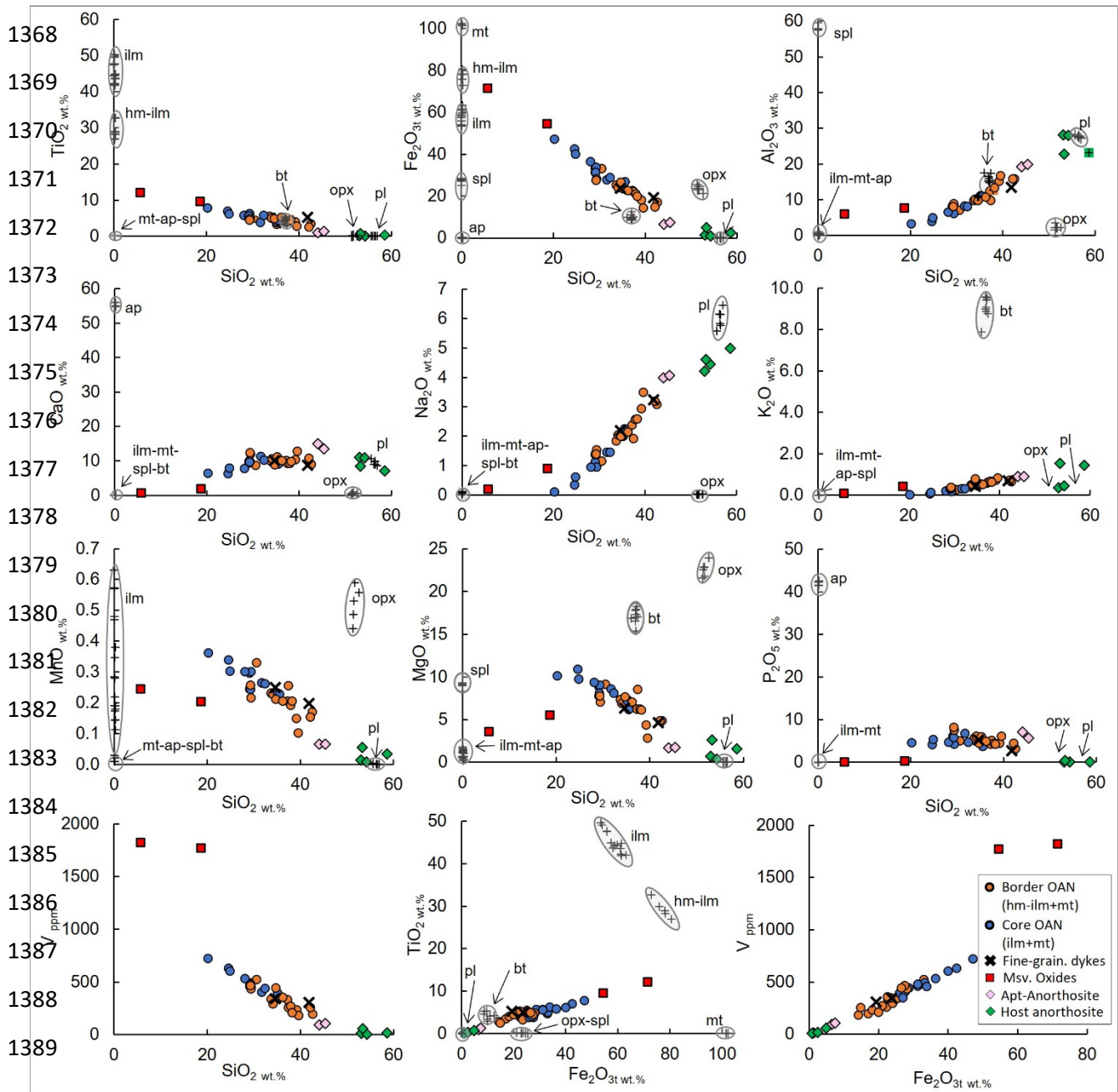
Figure 7. Whole-rock variation diagrams for the Lac à l'Orignal Fe-Ti-P deposit with the major mineral compositions plotted from electron microprobe and SEM data. Mineral abbreviations: pl = plagioclase; opx = orthopyroxene; bt = biotite; hm-ilm = hemo-ilmenite; ilm = ilmenite; mt = magnetite; ap = apatite; spl = Al-spinel; hbl = hornblende. OAN = oxide-apatite-norite; Msv.oxides = massive oxides; Fine-grain. Dykes = fine-grained ferrodiorite dykes.

1396
1397
1398
1399
1400
1401
1402
1403
1404
1405
1406
1407
1408
1409
1410
1411
1412
1413
1414
1415
1416
1417
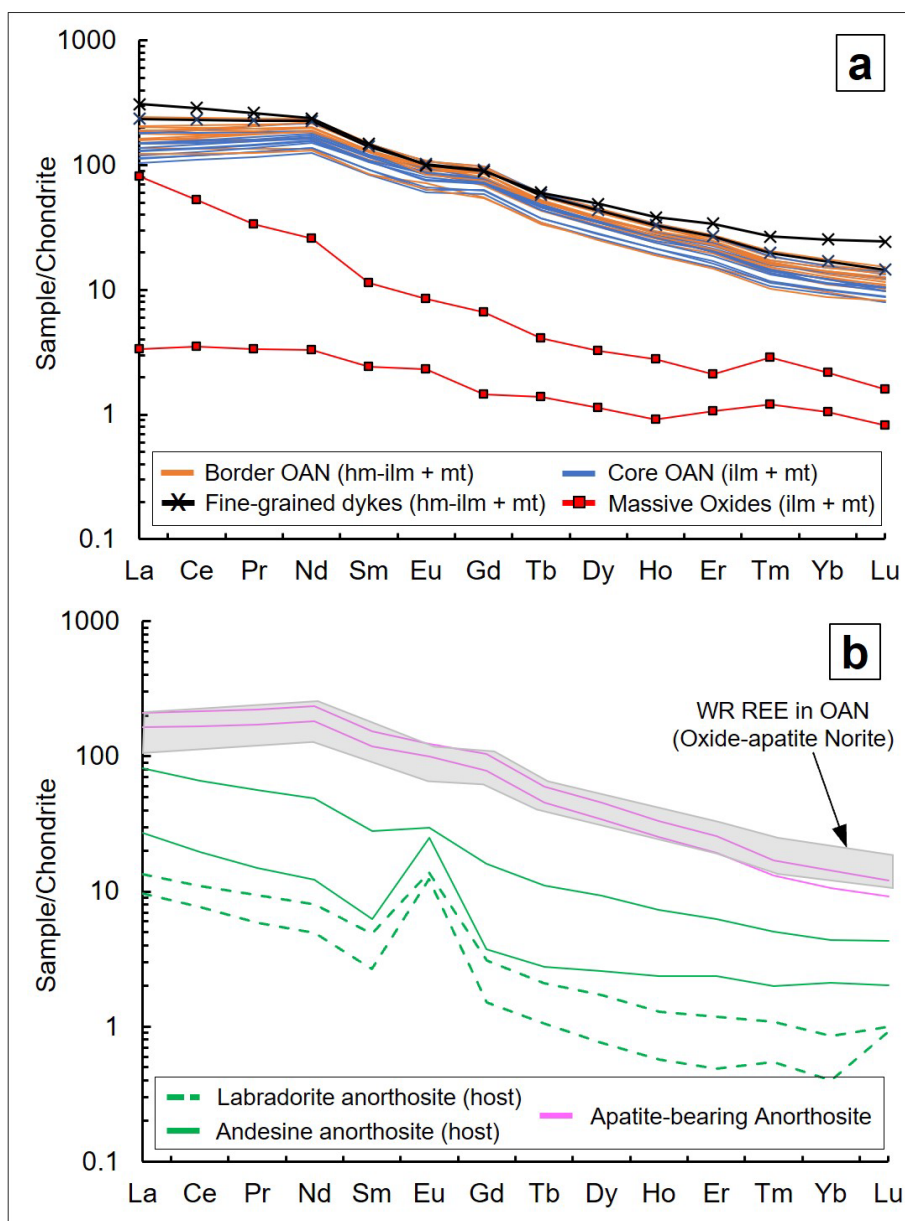
Figure 8. Chondrite-normalized REE compositions of whole-rock samples (normalized to chondrite; Sun and McDonough, 1989). a Mineralized samples: border and core OAN, massive oxides and fine-grained dykes. b Comparison between anorthosite samples (host and apatite-bearing layers) and the mineralized OAN from Fig. 8b (grey field). Mineral abbreviations: hm-ilm = hemo-ilmenite; ilm = ilmenite; mt = magnetite.
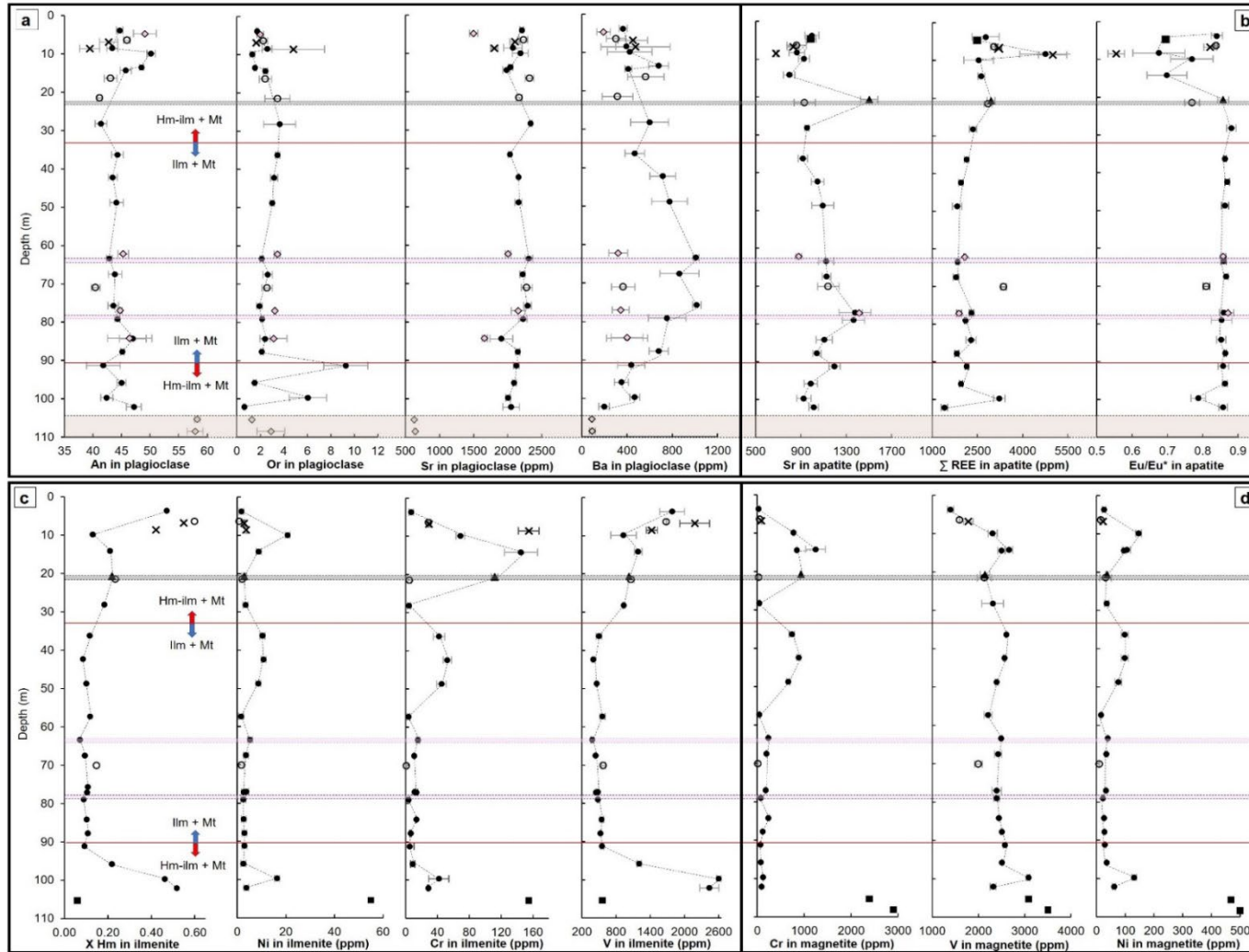
Figure 9. Stratigraphic variation of plagioclase (a), apatite (b), ilmenite (c) magnetite (d) compositions in drillcore LO-14-21. The grey horizon represents the nelsonite (iap-C) layer. The pink horizons represent the apatite-bearing anorthosite (pa-C) layers and the brownish horizon the host anorthosite. Red lines indicate the oxide assemblage changing from Hm-ilmenite to Fe-poor ilmenite towards the core of the intrusion. Error bars = 1 standard deviation and represents the natural variation within the thin section. Mineral abbreviations: hm-ilm = hemo-ilmenite; ilm = ilmenite; mt = magnetite.

1443
1444
1445
1446
1447
1448
1449
1450
1451
1452
1453
1454
1455
1456
1457
1458
1459
1460
1461
1462
1463
1464
1465
1466
1467
1468
1469
1470
1471
1472
1473
1474
1475
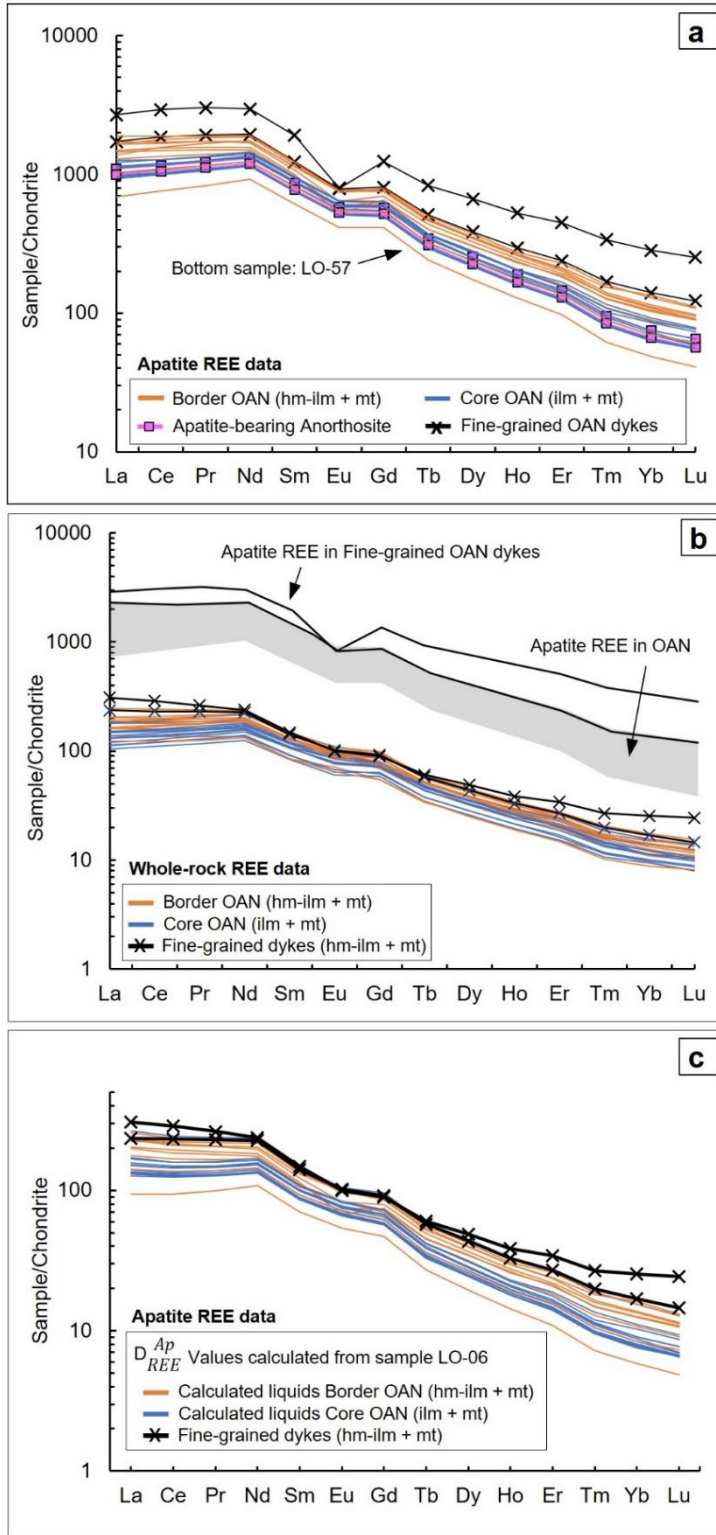
Figure 10. Chondrite-normalized REE compositions (after Sun and McDonough, 1989). a Apatite REE-data. b Whole-rock REE data in comparison with apatite (grey field – Fig.10-A) showing the REE behavior controlled by apatite concentration. c Apatite REE patterns for fine-grained OAN dykes (samples LO-06 and LO-08) compared to calculated liquids from the inversion of apatite compositions of border (orange lines) and core (blue lines) samples. Calculated liquids applying D^{Ap}_{REE} values obtained from bulk and apatite compositions of dyke sample LO-06.

1476

1477

1478

1479

1480

1481

1482

1483

1484

1485

1486

1487

1488

1489

1490

1491

1492

1493

1494

1495

1496

1497

1498

1499

1500

1501

1502

1503
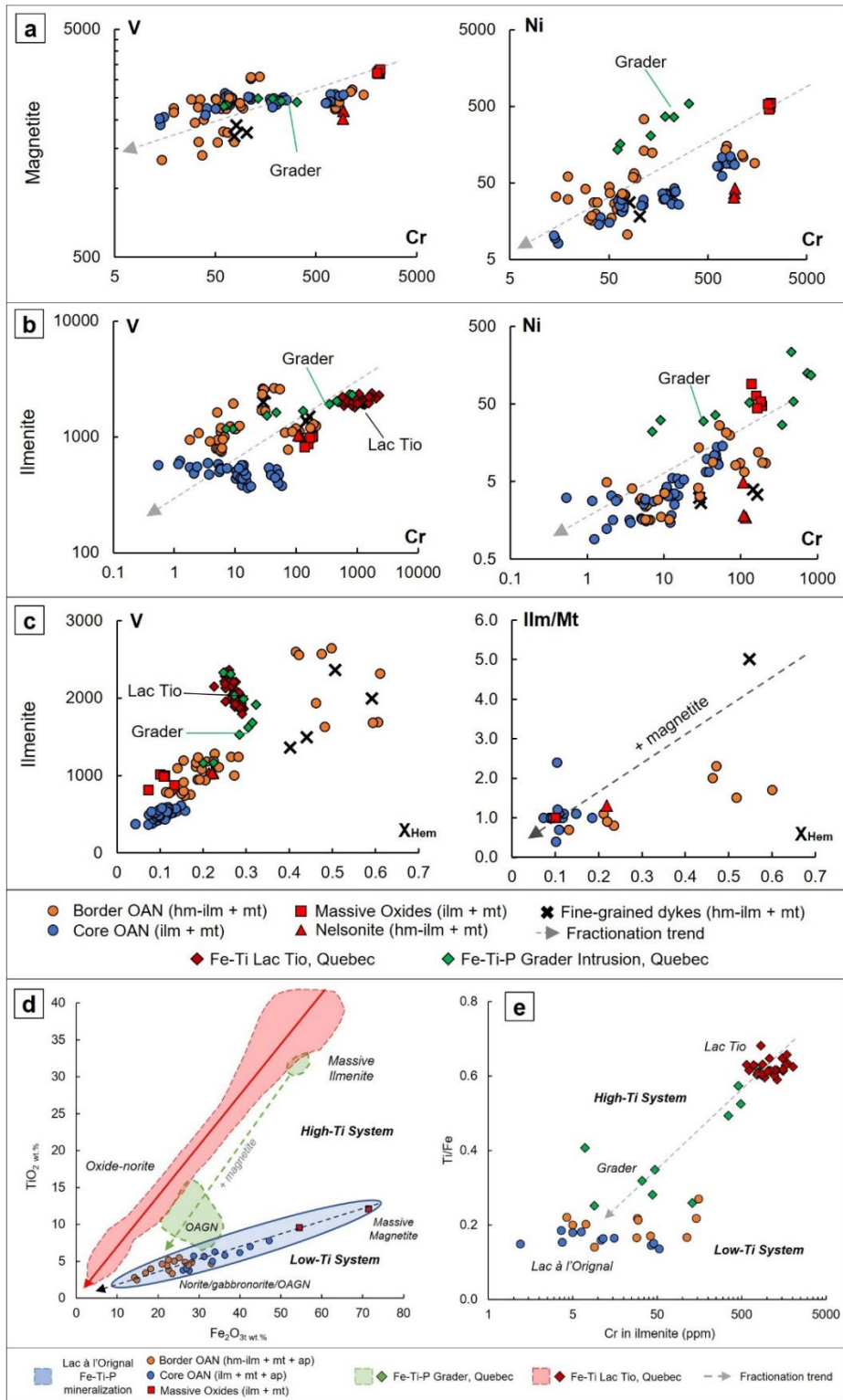
Figure 11. Binary diagrams displaying concentrations of compatible elements in magnetite (a) and ilmenite (b), using Cr as a proxy for fractional crystallization. c Hematite content in ilmenite in relation to the V concentration in ilmenite (left) and the modal proportion of magnetite (right). Comparison between geochemical data of the Lac à l'Orignal Fe-Ti-P deposit (this work), the Grader intrusion Fe-Ti-P, Quebec (Charlier et al. 2008) and the world-class ilmenite deposit of Lac Tio Fe-Ti, Quebec (Charlier et al. 2010). d-e Geochemical comparison of the Lac à l'Orignal Fe-Ti-P deposit (blue field – this study) with the Lac Tio Ti deposit (red field) and the Fe-Ti-P mineralization at Grader intrusion (green field), in the Havre Saint Pierre Anorthosite, Quebec (data from Charlier at al. 2010; 2008). e Whole-rock Fe_2O_{3t} vs. TiO_2. e Ti/Fe whole rock ratio vs. Cr content of ilmenite

Sample	FeOt (%)	TiO$_2$ (%)	Al$_2$O$_3$ (%)	MgO (%)	MnO (%)	Sc ppm	V ppm	Cr ppm	Ni ppm
Ilmenite Core 1	43.29	54.33	0.08	1.63	0.61	103.41	976.17	47.15	15.92
Ilmenite Edge 1	38.43	58.38	0.26	1.87	0.72	120.41	781.38	39.66	15.93
Relative Difference (%)	-12.65	6.94	69.86	12.76	14.80	14.12	-24.93	-18.89	0.07
Ilmenite Core 2	43.40	54.06	0.11	1.62	0.63	110.06	979.87	54.72	14.13
Ilmenite Edge 2	38.33	58.50	0.33	1.85	0.76	132.48	646.20	40.34	15.26
Relative Difference (%)	-13.23	7.59	66.27	12.64	16.65	16.93	-51.64	-35.66	7.38
Magnetite Core	89.59	0.27	1.63	0.50	0.04	5.21	3101.33	87.80	59.33
Magnetite Edge	89.30	0.83	1.91	0.50	0.03	4.82	2656.28	94.54	52.74
Relative Difference (%)	-0.32	67.48	14.68	0.61	-27.63	-8.13	-16.75	7.13	-12.49

Figure 12. Fully quantified, high resolution element maps, using LA-Time of Flight-ICP-MS, showing the distribution of some major and trace element at the contact between ilmenite and magnetite crystals (sample LO-24). Any significant relative difference (%) in the element concentrations of selected core and edge areas in ilmenite and magnetite are due to sub-solidus, inter-oxide reequilibration. Red-yellow colors representing higher concentration of an element. Blue-white colors
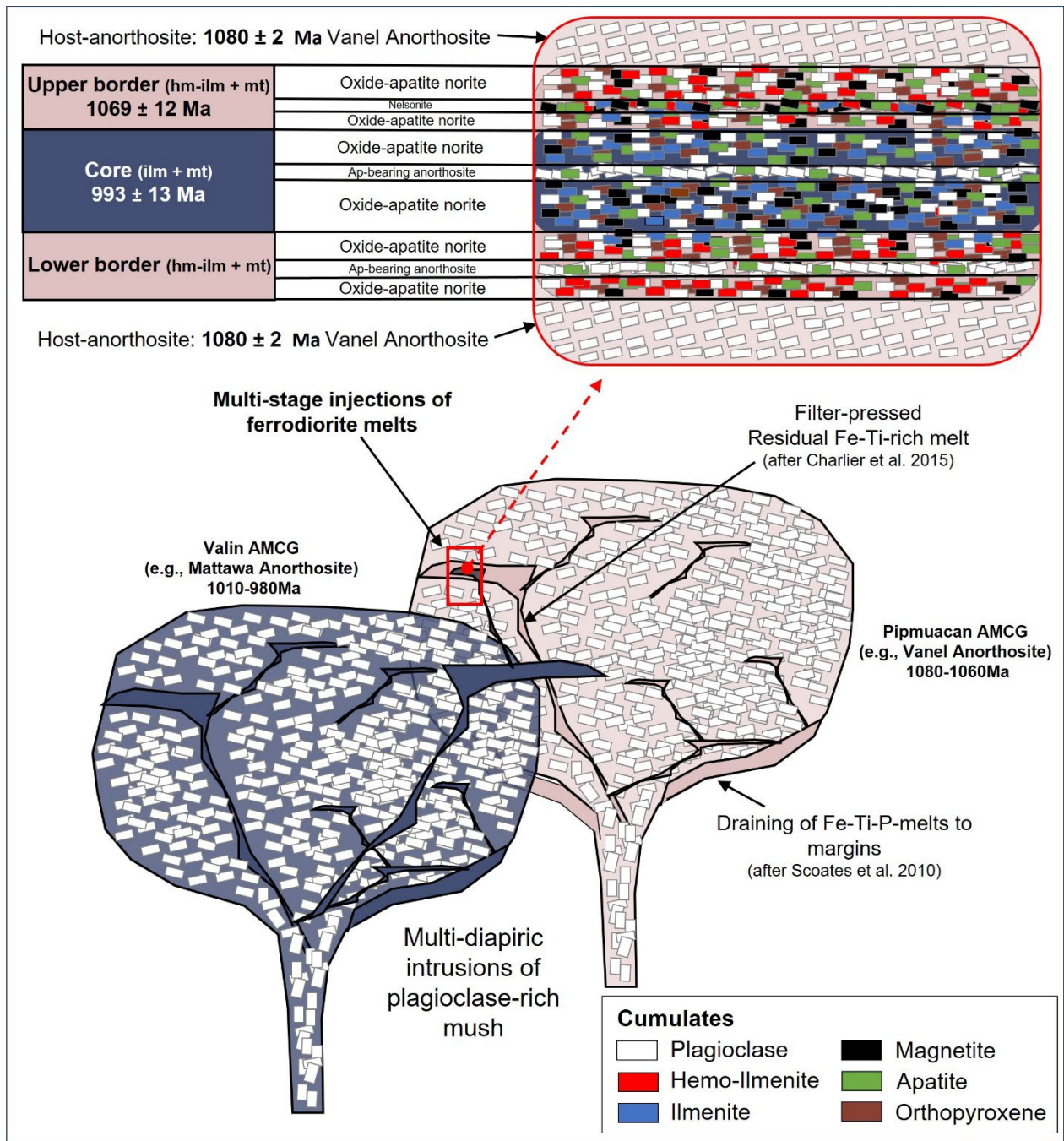
Figure 2.13. Schematic simplified model for the generation of Fe-Ti-P mineralization, exemplified by the Lac à l'Orignal Fe-Ti-P deposit in the Central Grenville Province. Fractionation of residual Fe-Ti-P rich ferrodiorite melts generated after anorthosite crystallization. a Multi-diapiric emplacement of mafic mantle-derived magmas forming the Pipmuacan AMCG suite (e.g. Vanel Anorthosite) favored by deep-seated shear zones like the Saint Fulgence Detachment Zone. Segregation of ferrodiorite residual liquids filter-pressed into fractures/zones of lower pressure, generating the accumulation of oxide-apatite cumulates in dykes/sill-like structures and/or around the anorthosite-massifs. b Emplacement and crystallization of the Valin AMCG suite and segregation of ferrodiorite residual magmas as previously described. Note that the intrusion of the Valin AMCG Suite within the previous Pipmuacan AMCG suite possibly the generation of conduits interconnecting different residual magma accumulation of different ages. c Fractionation of evolved Fe-Ti-P melts with apatite as a liquids phase, dominated by (hemo)-ilmenite + magnetite + apatite initially (older border), and subsequently dominated by ilmenite + magnetite + apatite (younger core). Formation of local oxide-apatite-rich layers (nelsonite) by settling; residual oxide-apatite-norite (apatite + apatite + silicates) and apatite-bearing anorthosite (plagioclase + apatite) by relatively flotation.

4

Table 1. Zircon U–Pb LA-ICP-MS analytical data of samples in hole LO-14-21 from the Lac à l'Orignal Fe-Ti-P deposit

#Analysis	U_ppm	Pb_ppm	Th/U	$^{206}Pb/^{204}Pb$	Isotopic ratios ±1s%			Apparent ages ±2s%			Rho
					$^{206}Pb/^{238}U$	$^{207}Pb/^{235}U$	$^{207}Pb/^{206}Pb$	$^{206}Pb/^{238}U$	$^{207}Pb/^{235}U$	$^{207}Pb/^{206}Pb$	
Oxide-apatite norite (hemo-ilmenite + magnetite bearing) - 14.0 - 16.0m depth											
GC-LOR-01_2	49.1	1814.4	0.9	-180.6	0.18432 ± 2.1	2.00082 ± 5.2	0.07858 ± 4.9	1088 ± 42	1079 ± 75	991 ± 225	0.27242
GC-LOR-01_3	23.8	848.2	0.8	-793.5	0.18209 ± 3.5	1.76384 ± 8.7	0.07136 ± 8.3	1071 ± 69	925 ± 111	465 ± 396	0.57702
GC-LOR-01_5	30.8	1087.1	1.1	189.0	0.18524 ± 4.4	1.9547 ± 11.7	0.08215 ± 9.7	1084 ± 86	1038 ± 148	1179 ± 322	0.45058
GC-LOR-01_6	15.1	505.4	0.5	68.8	0.17415 ± 3.3	2.18625 ± 10.5	0.09371 ± 9.9	1030 ± 61	1030 ± 168	1466 ± 330	0.34580
GC-LOR-01_7	233.2	8207.0	1.4	1113.5	0.15861 ± 1.8	2.04052 ± 3.1	0.07945 ± 2.7	1102 ± 35	1119 ± 42	1098 ± 118	0.45140
GC-LOR-01_10	49.8	1784.2	1.0	170.5	0.19041 ± 2.8	2.30463 ± 7.2	0.08391 ± 7.1	1119 ± 57	1126 ± 99	903 ± 326	0.22514
GC-LOR-01_11	64.5	2279.9	2.3	66.0	0.18714 ± 3.7	2.30761 ± 9.2	0.08902 ± 8.9	1103 ± 73	1166 ± 117	1142 ± 361	0.26715
GC-LOR-01_12	24.8	811.6	1.0	20.8	0.17201 ± 2.6	1.62206 ± 7.5	0.06738 ± 7.5	1019 ± 49	890 ± 110	630 ± 357	0.09702
GC-LOR-01_13	28.5	910.3	0.9	13.2	0.16721 ± 2.8	1.74013 ± 7.8	0.07373 ± 7.3	993 ± 52	934 ± 104	642 ± 357	-0.11120
GC-LOR-01_15	7.4	239.2	0.5	1.7	0.17471 ± 5.4	1.97317 ± 14.8	0.07303 ± 16.8	1021 ± 101	892 ± 253	1991 ± 331	0.45490
GC-LOR-01_16	31.9	1026.7	0.9	6.1	0.16922 ± 3.2	1.94567 ± 6.6	0.08358 ± 6.9	1002 ± 59	1041 ± 95	1089 ± 287	-0.07291
GC-LOR-01_17	484.2	15990.8	0.8	121.8	0.18008 ± 2.1	1.94987 ± 2.2	0.07732 ± 2.1	1065 ± 40	1090 ± 29	1085 ± 82	0.60867
GC-LOR-01_19	6.1	187.8	0.6	2.3	0.16846 ± 5.1	1.66545 ± 17.1	0.08767 ± 17.9	990 ± 91	640 ± 347	2178 ± 324	0.02042
GC-LOR-01_20	444.6	14541.9	0.7	175.2	0.17638 ± 2.1	1.86342 ± 3.1	0.07378 ± 2.5	1044 ± 40	1059 ± 40	998 ± 101	0.59924
Oxide-apatite norite (ilmenite + magnetite bearing) - 41.0 - 43.0m depth											
GC-LOR-02_1	24.0	752.2	2.2	11.6	0.16758 ± 3.1	1.58629 ± 8.3	0.07237 ± 8.2	1000 ± 57	864 ± 125	809 ± 347	0.15626
GC-LOR-02_2	176.5	5446.0	0.4	145.1	0.16328 ± 1.7	1.65135 ± 3.2	0.07164 ± 3.3	968 ± 30	973 ± 41	892 ± 144	0.18780
GC-LOR-02_3	85.5	2745.2	1.4	-7.8	0.16952 ± 2.4	1.69575 ± 4.3	0.07203 ± 4.4	1006 ± 44	986 ± 55	851 ± 193	0.17176
GC-LOR-02_5	8.4	273.2	1.1	3.8	0.16461 ± 3.7	1.63427 ± 14.2	0.07538 ± 15.1	975 ± 68	628 ± 232	1898 ± 323	0.04278
GC-LOR-02_6	6.2	193.5	0.8	3.2	0.16931 ± 5.5	2.16737 ± 18.6	0.14402 ± 20.1	991 ± 102	759 ± 291	2386 ± 408	-0.16299
GC-LOR-02_7	47.9	1466.1	1.3	16.5	0.17219 ± 3.5	1.72061 ± 6.3	0.07098 ± 5.9	1018 ± 63	953 ± 79	687 ± 303	0.31096
GC-LOR-02_8	7.1	226.0	0.6	-0.1	0.17361 ± 4.5	2.07287 ± 16.1	0.09835 ± 16.7	1020 ± 86	710 ± 278	2333 ± 346	-0.20157
GC-LOR-02_9	23.6	695.2	1.1	0.1	0.16049 ± 2.8	1.70196 ± 9.3	0.07683 ± 9.5	956 ± 49	878 ± 134	866 ± 390	0.01493
GC-LOR-02_10	15.8	462.1	1.9	5.3	0.15928 ± 4.1	2.10853 ± 10.4	0.10365 ± 11.6	945 ± 69	953 ± 155	1445 ± 388	-0.08488
GC-LOR-02_12	15.3	474.4	2.3	15.8	0.17428 ± 3.5	1.98305 ± 10.6	0.08587 ± 11.9	1028 ± 67	920 ± 171	1224 ± 384	-0.01054
GC-LOR-02_14	12.8	395.2	0.5	9.1	0.16971 ± 4.1	1.41787 ± 13.7	0.06286 ± 15.6	1020 ± 82	728 ± 195	1163 ± 373	0.12923
GC-LOR-02_15	20.8	597.4	1.0	5.0	0.16774 ± 3.5	1.66007 ± 9.8	0.07706 ± 9.9	993 ± 64	962 ± 142	969 ± 370	0.20728
GC-LOR-02_16	30.0	832.7	1.1	18.0	0.16721 ± 3.5	1.74633 ± 8.2	0.07661 ± 7.9	990 ± 63	903 ± 115	935 ± 339	0.00805
GC-LOR-02_17	7.7	221.7	0.6	5.8	0.16865 ± 4.3	1.76706 ± 18.1	0.07941 ± 18.4	1010 ± 84	683 ± 303	1951 ± 333	0.29674
GC-LOR-02_18	20.7	593.1	1.1	12.1	0.17156 ± 3.8	1.82227 ± 9.6	0.07824 ± 9.3	1013 ± 71	880 ± 154	1173 ± 331	0.33830
GC-LOR-02_19	15.9	433.5	1.7	2.8	0.16671 ± 3.8	1.48753 ± 14.1	0.07406 ± 14.1	986 ± 70	647 ± 207	1380 ± 392	0.05748

1535

1536

1537

1538

1539

1540   Table 2. Representative LA-ICP-MS Whole-rock major and trace element compositions (by LA-ICP-MS)

Sample	Depth (m)	Location	Lithology	Oxides	SiO_2	TiO_2	Al_2O_3	Fe_2O_{3t}	MnO	MgO	CaO	Na_2O	K_2O	P_2O_5	LOI	Total
LO-01	3.70	LO-14-21	Medium-grained OAN	Hm-ilm + Mt	42.6	3.4	15.8	17.0	0.2	4.9	9.1	3.1	0.7	3.1	0.3	100.0
LO-05	6.40	LO-14-21	Coarse-grained OAN	Hm-ilm + Mt	39.2	4.0	15.2	18.2	0.1	4.3	10.4	2.9	0.7	4.5	0.4	100.0
LO-06	6.80	LO-14-21	Fine-grained OAN dyke	Hm-ilm + Mt	34.6	5.1	10.9	23.7	0.2	6.3	10.2	2.2	0.4	5.3	1.1	100.0
LO-07	8.50	LO-14-21	Medium-grained OAN	Hm-ilm + Mt	39.6	2.8	16.8	14.2	0.1	2.8	12.8	3.5	0.8	6.1	0.4	100.0
LO-08	8.60	LO-14-21	Fine-grained-OAN dyke	Hm-ilm	41.8	5.2	13.5	19.3	0.2	4.6	8.8	3.2	0.7	2.7	0.0	100.0
LO-10	10.50	LO-14-21	Medium-grained OAN	Hm-ilm + Mt	30.6	4.7	7.1	33.1	0.3	9.1	8.7	1.1	0.3	5.0	0.0	100.0
LO-16	16.40	LO-14-21	Coarse-grained OAN	Hm-ilm + Mt	33.7	5.5	9.8	25.2	0.2	7.3	10.0	1.8	0.5	5.7	0.2	100.0
LO-18	19.50	LO-14-21	Medium-grained OAN	Hm-ilm + Mt	37.2	3.8	12.4	22.6	0.2	6.2	10.1	2.4	0.6	4.2	0.3	100.0
LO-22	21.50	LO-14-21	Coarse-grained OAN	Hm-ilm + Mt	37.4	4.4	9.8	22.2	0.3	8.5	9.3	1.9	0.6	5.1	0.5	100.0
LO-23	22.70	LO-14-21	Medium-grained OAN	Hm-ilm + Mt	34.1	5.0	10.2	23.9	0.2	6.9	10.6	2.0	0.5	6.1	0.5	100.0
LO-24	28.20	LO-14-21	Medium-grained OAN	Hm-ilm + Mt	37.9	4.6	12.6	21.0	0.2	6.2	9.3	2.6	0.7	4.4	0.4	100.0
LO-25	32.20	LO-14-21	Medium-grained OAN	Ilm + Mt	35.2	3.3	10.9	23.4	0.2	7.3	11.1	2.0	0.4	6.0	0.1	100.0
LO-26	36.30	LO-14-21	Medium-grained OAN	Ilm + Mt	35.2	3.8	11.1	26.0	0.2	7.2	9.5	2.0	0.5	4.5	0.1	100.0
LO-29	42.40	LO-14-21	Medium-grained OAN	Ilm + Mt	31.7	3.8	8.2	27.6	0.3	8.6	11.3	1.5	0.3	6.8	0.0	100.0
LO-32	48.70	LO-14-21	Medium-grained OAN	Ilm + Mt	29.1	5.0	7.2	33.2	0.3	8.9	9.5	1.1	0.3	5.4	0.0	100.0
LO-34	56.70	LO-14-21	Medium-grained OAN	Ilm + Mt	29.4	6.3	6.1	33.8	0.3	9.0	9.8	0.9	0.2	4.2	0.0	100.0
LO-37	61.20	LO-14-21	Medium-grained OAN	Ilm + Mt	32.4	5.7	8.1	28.7	0.3	8.1	10.3	1.4	0.3	4.7	0.0	100.0
LO-38	62.20	LO-14-21	Apatite-bearing Anorthosite	-	44.1	0.9	19.2	6.5	0.1	1.7	15.0	4.0	0.9	7.1	0.6	100.0
LO-39	63.40	LO-14-21	Medium-grained OAN	Ilm + Mt	20.2	7.8	3.3	47.2	0.4	10.1	6.4	0.1	0.0	4.6	0.0	100.0
LO-40	67.50	LO-14-21	Medium-grained OAN	Ilm + Mt	28.1	5.8	6.5	36.3	0.3	9.3	7.8	0.9	0.2	4.6	0.0	100.0
LO-41B	70.10	LO-14-21	Coarse-grained-OAN	Ilm + Mt	35.6	4.0	11.0	26.9	0.2	6.2	9.1	2.3	0.6	3.7	0.4	100.0
LO-43	75.70	LO-14-21	Medium-grained OAN	Ilm + Mt	24.6	7.0	3.9	42.5	0.3	10.9	6.2	0.3	0.1	4.2	0.0	100.0
LO-44-2	77.00	LO-14-21	Apatite-bearing Anorthosite	-	45.4	1.3	19.9	7.4	0.1	1.7	13.5	4.1	0.9	5.6	0.2	100.0
LO-46	79.00	LO-14-21	Medium-grained OAN	Ilm + Mt	24.8	6.2	5.0	40.0	0.3	9.7	7.9	0.6	0.1	5.3	0.0	100.0
LO-49	87.80	LO-14-21	Medium-grained OAN	Ilm + Mt	29.1	5.7	8.3	31.2	0.2	7.8	10.0	1.4	0.3	6.1	0.0	100.0
LO-50	91.20	LO-14-21	Medium-grained OAN	Ilm + Mt	29.2	5.6	8.4	31.2	0.2	8.1	9.6	1.4	0.3	5.8	0.0	100.0
LO-51	95.80	LO-14-21	Medium-grained OAN	Hm-ilm + Mt	29.4	4.8	8.9	28.2	0.2	7.0	12.0	1.5	0.4	7.5	0.0	100.0
LO-55	99.70	LO-14-21	Medium-grained OAN	Hm-ilm + Mt	42.2	2.5	15.8	14.8	0.2	4.8	10.8	3.2	0.7	4.4	0.6	100.0
LO-57	102.10	LO-14-21	Medium-grained OAN	Hm-ilm + Mt	29.3	4.5	8.1	27.5	0.3	7.7	12.4	1.4	0.4	8.2	0.4	100.0
LO-58	105.40	LO-14-21	Anorthosite	-	53.0	0.2	28.1	1.3	0.0	0.7	11.1	4.2	0.4	0.1	1.0	100.0
LO-59	108.50	LO-14-21	Anorthosite	-	54.2	0.1	28.0	0.9	0.0	0.3	10.9	4.4	0.5	0.0	0.6	100.0
20PM02	0.00	Surface	Medium-grained OAN	Hm-ilm + Mt	34.7	4.9	9.8	26.6	0.2	7.7	8.8	2.0	0.8	4.5	-0.1	100.0
20PM03	0.00	Surface	Massive oxides in anorthosite	Ilm + Mt	18.7	9.5	7.6	54.5	0.2	5.5	1.9	0.9	0.4	0.3	-0.4	100.0
20PM03B	0.00	Surface	Anort. hosting massive oxides	-	53.3	0.7	22.7	4.8	0.1	2.6	8.5	4.6	1.5	0.4	0.7	100.0

1541

1542

1543

1544

1545 Table 2. (cont.) Representative LA-ICP-MS Whole-rock major and trace element compositions (by LA-ICP-MS)

Sample	Depth (m)	Location	Lithology	Oxides	V	Cr	Ni	Sr	Y	Zr	La	Ce	Eu/Eu*
LO-01	3.70	LO-14-21	Medium-grained OAN	Hm-ilm + Mt	195	30	29	1296	28	75	33	84	1.0
LO-05	6.40	LO-14-21	Coarse-grained OAN	Hm-ilm + Mt	234	31	50	1320	38	101	42	109	1.0
LO-06	6.80	LO-14-21	Fine-grained OAN dyke	Hm-ilm + Mt	342	31	53	891	48	110	56	142	0.9
LO-07	8.50	LO-14-21	Medium-grained OAN	Hm-ilm + Mt	181	18	42	1514	55	53	62	161	1.0
LO-08	8.60	LO-14-21	Fine-grained-OAN dyke	Hm-ilm	307	44	41	1126	56	412	73	176	0.8
LO-10	10.50	LO-14-21	Medium-grained OAN	Hm-ilm + Mt	522	180	239	542	47	124	37	102	0.7
LO-16	16.40	LO-14-21	Coarse-grained OAN	Hm-ilm + Mt	338	23	39	899	43	72	45	118	0.9
LO-18	19.50	LO-14-21	Medium-grained OAN	Hm-ilm + Mt	333	80	168	1023	37	23	35	93	0.9
LO-22	21.50	LO-14-21	Coarse-grained OAN	Hm-ilm + Mt	259	17	25	811	49	370	58	148	0.8
LO-23	22.70	LO-14-21	Medium-grained OAN	Hm-ilm + Mt	292	15	45	959	46	117	49	128	0.9
LO-24	28.20	LO-14-21	Medium-grained OAN	Hm-ilm + Mt	272	16	41	1164	35	161	38	98	1.0
LO-25	32.20	LO-14-21	Medium-grained OAN	Ilm + Mt	350	137	141	912	41	39	39	105	0.9
LO-26	36.30	LO-14-21	Medium-grained OAN	Ilm + Mt	395	125	115	870	36	90	35	92	0.9
LO-29	42.40	LO-14-21	Medium-grained OAN	Ilm + Mt	405	152	134	721	48	53	43	118	0.9
LO-32	48.70	LO-14-21	Medium-grained OAN	Ilm + Mt	493	161	114	555	38	40	33	90	0.9
LO-34	56.70	LO-14-21	Medium-grained OAN	Ilm + Mt	455	36	42	437	38	66	28	78	0.9
LO-37	61.20	LO-14-21	Medium-grained OAN	Ilm + Mt	441	30	46	621	38	163	31	83	0.9
LO-38	62.20	LO-14-21	Apatite-bearing Anorthosite	-	91	38	16	1617	47	28	50	131	1.0
LO-39	63.40	LO-14-21	Medium-grained OAN	Ilm + Mt	722	146	102	162	31	128	27	73	0.8
LO-40	67.50	LO-14-21	Medium-grained OAN	Ilm + Mt	533	66	58	471	30	70	27	73	0.9
LO-41B	70.10	LO-14-21	Coarse-grained-OAN	Ilm + Mt	350	23	20	947	42	26	44	112	0.9
LO-43	75.70	LO-14-21	Medium-grained OAN	Ilm + Mt	632	70	77	241	28	69	25	68	0.8
LO-44-2	77.00	LO-14-21	Apatite-bearing Anorthosite	-	107	32	23	1626	37	77	39	102	1.0
LO-46	79.00	LO-14-21	Medium-grained OAN	Ilm + Mt	604	34	53	365	34	113	31	85	0.8
LO-49	87.80	LO-14-21	Medium-grained OAN	Ilm + Mt	460	50	61	678	38	95	36	97	0.9
LO-50	91.20	LO-14-21	Medium-grained OAN	Ilm + Mt	478	30	52	688	37	128	35	95	0.9
LO-51	95.80	LO-14-21	Medium-grained OAN	Hm-ilm + Mt	435	35	51	782	47	64	44	121	0.9
LO-55	99.70	LO-14-21	Medium-grained OAN	Hm-ilm + Mt	256	70	72	1231	35	102	41	101	1.0
LO-57	102.10	LO-14-21	Medium-grained OAN	Hm-ilm + Mt	466	30	92	697	40	65	38	102	0.8
LO-58	105.40	LO-14-21	Anorthosite	-	14	22	19	639	2	10	3	7	3.5
LO-59	108.50	LO-14-21	Anorthosite	-	6	16	13	663	1	3	2	5	5.9
20PM02	0.00	Surface	Medium-grained OAN	Hm-ilm + Mt	442	24	21	698	28	110	29	76	0.9
20PM03	0.00	Surface	Massive oxides in anorthosite	Ilm + Mt	1769	943	337	247	4	59	19	32	0.9
20PM03B	0.00	Surface	Anort. hosting massive oxides	-	58	87	56	510	11	134	19	41	1.3

1546 OAN = Oxide-apatite norite; Anort = Anorthosite; Hm-ilm = hemo-ilmenite; Ilm = ilmenite; Mt = magnetite. UTM Coordinates: borehole LO-14-21: 384535E/5437021N; LO-12-10: 384713E/5436961N;
1547 LO-12-25: 384445E/5436975N; LO-12-31: 385824E/5436863N; LO-12-13: 384730E/5436854N; 20PM02: 384943E/5436888N; 20PM03: 386644E/5436738N. Eu/Eu* = (Eu)n/[(Sm)n x (Gd)n]0.5
1548 calculated with Chondrite normalization values of Sun & McDonough (1989).

1549

1550

Table 3. Representative LA-ICP-MS major and trace element analyses of plagioclase for samples the Lac à l'Orignal Fe-Ti-P deposit

Sample	Depth (m)	Lithology	Oxides	# analysis	SiO$_2$	Al$_2$O$_3$	CaO	Na$_2$O	K$_2$O	Total	An	Ab	Or	0.058-0.245 [88]Sr	0.515-0.809 [137]Ba	0.005-0.013 [139]La	0.003-1.838 [140]Ce	0.001-0.023 [153]Eu	Total REE
														Detection Limits (33-55µm)					
LO-01	3.7	Medium-grained OAN	Hm-ilm + Mt	n=5	56.1	28.1	8.7	5.7	0.3	99.0	44.7	53.6	1.7	2209	365	6	9	2	22
LO-02	4.7	Anorthosite	-	n=5	54.8	29.2	9.4	5.2	0.3	99.1	49.1	48.9	2.0	1501	193	7	11	1	25
LO-05	6.4	Coarse-grained OAN	Hm-ilm + Mt	n=5	56.2	28.1	8.8	5.5	0.4	99.2	45.9	51.8	2.3	2233	303	8	11	2	27
LO-06	6.8	Fine-grained OAN dyke	Hm-ilm + Mt	n=5	56.6	28.0	8.3	6.0	0.3	99.3	42.7	55.6	1.7	2106	450	8	11	2	26
LO-07	8.5	Medium-grained OAN	Hm-ilm + Mt	n=5	56.7	27.8	8.4	5.8	0.4	99.2	43.3	54.1	2.6	2078	393	11	16	2	36
LO-08	8.6	Fine-grained-OAN dyke	Hm-ilm		57.7	27.0	7.6	5.9	0.8	99.1	39.4	55.7	4.8	1803	475	16	21	2	46
LO-09	9.9	Medium-grained OAN	Hm-ilm + Mt	n=5	54.6	29.3	9.6	5.2	0.2	99.1	50.1	48.5	1.3	2187	424	7	10	1	23
LO-15-1	14.2	Medium-grained OAN	Hm-ilm + Mt	n=4	55.0	29.0	9.4	5.3	0.3	99.1	48.5	50.0	1.5	2040	680	6	9	1	21
LO-15-2	14.4	Medium-grained OAN	Hm-ilm + Mt	n=5	55.7	28.5	8.8	5.5	0.4	99.1	45.7	51.8	2.4	1985	412	7	11	1	24
LO-16	16.4	Coarse-grained-OAN	Hm-ilm + Mt	n=5	56.8	27.7	8.3	5.8	0.4	99.2	43.1	54.5	2.4	2322	566	6	8	2	19
LO-22	21.5	Coarse-grained OAN	Hm-ilm + Mt	n=5	57.1	27.5	8.0	5.9	0.6	99.2	41.2	55.4	3.5	2171	315	6	9	2	20
LO-24	28.2	Medium-grained OAN	Hm-ilm + Mt	n=4	56.9	27.8	8.0	5.9	0.6	99.3	41.4	55.0	3.6	2337	600	5	8	2	18
LO-26	36.3	Medium-grained OAN	Ilm + Mt	n=5	56.3	28.1	8.5	5.5	0.6	99.2	44.3	52.2	3.5	2035	468	5	7	2	17
LO-29	42.4	Medium-grained OAN	Ilm + Mt	n=5	56.4	28.1	8.4	5.7	0.5	99.2	43.5	53.4	3.2	2158	715	5	8	1	18
LO-32	48.7	Medium-grained OAN	Ilm + Mt	n=6	56.2	28.2	8.5	5.6	0.5	99.2	44.1	52.9	3.0	2159	776	4	7	1	16
LO-38	62.2	Apatite-bearing Anorthosite	-	n=5	56.2	28.4	8.6	5.4	0.6	99.3	45.3	51.3	3.4	2006	322	4	6	2	15
LO-39	63.4	Medium-grained OAN	Ilm + Mt	n=5	56.3	28.1	8.3	5.9	0.3	99.1	42.8	55.1	2.1	2309	1008	4	7	1	15
LO-40	67.5	Medium-grained OAN	Ilm + Mt	n=6	56.1	28.3	8.5	5.7	0.4	99.2	43.8	53.5	2.6	2218	863	4	7	1	15
LO-41B	70.1	Coarse-grained OAN	Ilm + Mt	n=6	57.2	27.6	7.8	6.1	0.4	99.4	40.5	56.9	2.6	2279	366	8	11	2	26
LO-43	75.7	Medium-grained OAN	Ilm + Mt	n=4	56.3	28.2	8.3	5.8	0.3	99.1	43.5	54.5	1.9	2290	1016	4	7	1	15
LO-44-2	77.0	Apatite-bearing Anorthosite	-	n=5	56.6	28.1	8.5	5.5	0.5	99.3	44.7	52.0	3.2	2154	343	4	7	2	12
LO-46	79.0	Medium-grained OAN	Ilm + Mt	n=5	56.5	28.2	8.5	5.7	0.3	99.4	44.3	53.6	2.1	2224	753	4	7	1	16
LO-47-1	84.2	Medium-grained OAN	Ilm + Mt	n=5	55.6	28.7	9.0	5.3	0.4	99.2	47.0	50.6	2.4	1907	402	5	7	1	17
LO-47-2	84.3	Anorthosite	-	n=5	56.0	28.7	8.8	5.3	0.5	99.4	46.4	50.5	3.1	1661	401	7	10	2	23
LO-49	87.8	Medium-grained OAN	Ilm + Mt	n=5	56.2	28.4	8.6	5.6	0.3	99.3	45.2	52.7	2.1	2150	679	4	7	1	15
LO-50	91.2	Medium-grained OAN	Ilm + Mt	n=4	56.5	27.8	8.5	5.7	1.4	99.9	41.8	50.3	7.9	2127	436	4	6	1	12
LO-51	95.8	Medium-grained OAN	Hm-ilm + Mt	n=6	56.4	28.2	8.6	5.7	0.2	99.3	45.0	53.5	1.5	2096	351	4	7	1	15
LO-55	99.7	Medium-grained OAN	Hm-ilm + Mt	n=4	56.5	27.7	8.4	5.6	1.0	99.3	42.4	51.6	6.1	2006	467	7	10	2	21
LO-57	102.1	Medium-grained OAN	Hm-ilm + Mt	n=6	55.4	28.9	9.1	5.6	0.1	99.2	47.1	52.2	0.7	2053	197	4	6	1	13
LO-58	105.4	Anorthosite	-	n=6	52.3	31.2	11.0	4.2	0.2	99.2	58.2	40.5	1.3	631	90	1	3	1	6

LO-59	108.5	Anorthosite	-	n=4	53.4	30.2	11.5	4.3	0.5	100.1	57.9	39.2	2.9	645	93	1	3	Below DL	4
20PM02	0.0	Medium-grained OAN	Hm-ilm + Mt	n=5	56.4	29.3	9.5	5.6	0.4	101.3	47.1	50.7	2.2	2274	414	5	8	2	18
20PM03B	0.0	Massive oxides in anorthosite	Ilm + Mt	n=5	55.6	30.7	10.6	5.4	0.1	102.4	49.7	49.6	0.7	2129	189	13	21	2	46

Major elements in wt.%, An=100 [Ca/(Ca+Na+K)]; Ab=100 [Na/(Ca+Na+K)]; Or=100 [K/(Ca+Na+K)]; trace element in ppm. OAN = Oxide-apatite norite; Hm-ilm = hemo-ilmenite; Ilm = ilmenite; Mt = magnetite.

Table 4. Representative LA-ICP-MS major and trace element analyses of apatite for samples the Lac à l'Orignal Fe-Ti-P deposit

Detection Limits (33-55µm bean size)					0.01-0.07	0.01-0.02	0.003-0.014	0.003-0.012	0.002-0.008	0.012-0.030	0.013-0.021	0.003-0.009	0.015-0.057	0.002-0.004	0.006-0.015	0.002-0.004	0.009-0.027	0.002-0.003
Sample	Depth (m)	Lithology	Oxide Mineralogy	# analysis	^{88}Sr	^{89}Y	^{139}La	^{140}Ce	^{141}Pr	^{146}Nd	^{147}Sm	^{153}Eu	^{157}Gd	^{159}Tb	^{166}Er	^{169}Tm	^{172}Yb	^{175}Lu
LO-01	4	Medium-grained OAN	Hm-ilm + Mt	n=4	997	369	326	957	155	799	168	42	151	17	32	3	17	2
LO-02	5	Massive Apatite	-	n=4	987	268	356	952	140	655	126	25	109	12	24	3	14	2
LO-05	6	Coarse-grained OAN	Hm-ilm + Mt	n=4	862	379	388	1095	171	852	176	44	155	17	33	3	18	2
LO-06	7	Fine-grained OAN dyke	Hm-ilm + Mt	n=4	831	414	408	1140	179	889	183	44	161	18	38	4	23	3
LO-07	9	Medium-grained OAN	Hm-ilm + Mt	n=6	864	609	690	1825	263	1210	237	45	201	24	57	7	37	5
LO-08	9	Fine-grained OAN dyke	Hm-ilm	n=3	679	763	637	1794	281	1351	283	45	247	30	72	8	46	6
LO-09	10	Medium-grained OAN	Hm-ilm + Mt	n=4	928	336	344	911	140	687	143	32	129	14	29	3	17	2
LO-15-1	14	Medium-grained OAN	Hm-ilm + Mt	n=4	796	333	353	955	146	713	148	29	130	15	30	3	17	2
LO-21	21	Medium-grained Nelsonite	Hm-ilm + Mt	n=4	1501	381	404	1052	161	794	170	43	150	17	34	4	22	3
LO-22	22	Coarse-grained-OAN	Hm-ilm + Mt	n=4	933	349	394	1031	160	771	159	36	139	16	31	3	18	2
LO-24	28	Medium-grained OAN	Hm-ilm + Mt	n=4	953	289	307	826	129	655	138	36	122	13	26	3	14	2
LO-26	36	Medium-grained OAN	Ilm + Mt	n=4	917	286	265	720	117	620	132	34	119	13	25	3	14	2
LO-29	42	Medium-grained OAN	Ilm + Mt	n=4	1047	251	241	662	108	566	121	31	109	12	22	2	11	1
LO-32	49	Medium-grained OAN	Ilm + Mt	n=4	1092	234	227	620	100	532	114	29	102	11	20	2	10	1
LO-38	62	Apatite-bearing Anorthosite	-	n=4	881	263	260	708	113	597	128	33	114	12	23	2	12	2
LO-39	63	Medium-grained OAN	Ilm + Mt	n=4	1123	229	232	630	101	532	112	29	101	11	20	2	10	1
LO-40	68	Medium-grained OAN	Ilm + Mt	n=4	1126	227	221	609	99	522	111	29	100	11	20	2	10	1
LO-41B	70	Coarse-grained-OAN	Ilm + Mt	n=4	1141	419	458	1203	186	925	191	46	168	18	37	4	21	3
LO-43	76	Medium-grained OAN	Ilm + Mt	n=4	1377	281	289	785	125	664	142	36	127	13	25	2	14	2
LO-44-2	77	Apatite-bearing anorthosite	-	n=4	1414	238	235	647	104	547	115	30	103	11	21	2	11	1
LO-46	79	Medium-grained OAN	Ilm + Mt	n=4	1364	254	264	714	115	605	129	33	117	12	23	2	12	1
LO-47	84	Medium-grained OAN	Ilm + Mt	n=4	1105	285	298	786	124	641	140	36	127	13	27	3	15	2
LO-49	88	Medium-grained OAN	Ilm + Mt	n=4	1040	228	226	625	101	524	111	29	99	11	20	2	10	1
LO-50	91	Medium-grained OAN	Ilm + Mt	n=3	1196	259	271	734	116	616	131	34	119	13	23	2	12	2

LO-51	96	Medium-grained OAN	Hm-ilm + Mt	n=4	986	249	244	671	108	562	120	31	107	12	22	2	11	2
LO-55	100	Medium-grained OAN	Hm-ilm + Mt	n=4	924	382	447	1159	175	872	180	42	158	18	36	4	21	3
LO-57	102	Medium-grained OAN	Hm-ilm + Mt	n=4	1013	187	163	463	77	423	91	23	82	9	15	2	8	1
20PM02	0	Medium-grained OAN	Hm-ilm + Mt	n=13	872	281	277	766	120	643	136	34	132	14	24	3	13	2

OAN = Oxide-apatite norite; Hm-ilm = hemo-ilmenite; Ilm = ilmenite; Mt = magnetite

Table 5. Representative LA-ICP-MS major and trace element analyses of ilmenite for samples the Lac à l'Orignal Fe-Ti-P deposit

Sample	Depth (m)	Lithology	Oxides	# analysis	TiO$_2$	Fe$_2$O$_3$	FeO	MnO	MgO	Total	X$_{geik}$	X$_{pyr}$	X$_{hem}$	X$_{ilm}$	^{51}V	^{53}Cr	^{60}Ni
			Detection Limits (33-55µm)												0.035-0.296	0.952-3.179	0.551-1.198
LO-01	3.7	Medium-grained OAN	Hm-ilm + Mt	n=4	28.22	50.27	25.17	0.12	0.24	99.27	0.009	0.003	0.472	0.522	1781.3	7.1	1.7
LO-05	6.4	Coarse-grained OAN	Hm-ilm + Mt	n=3	21.53	64.50	19.00	0.20	0.36	99.52	0.013	0.004	0.600	0.389	1683.2	29.0	0.8
LO-06	6.8	Fine-grained OAN dyke	Hm-ilm + Mt	n=4	24.37	59.09	21.85	0.13	0.22	100.00	0.008	0.003	0.549	0.445	2179.9	29.6	2.9
LO-08	8.6	Fine-grained OAN dyke	Hm-ilm	n=4	31.09	45.06	26.57	0.24	0.79	99.43	0.029	0.005	0.421	0.564	1428.3	154.8	3.7
LO-09	9.9	Medium-grained OAN	Hm-ilm + Mt	n=3	46.15	12.71	38.97	0.75	1.59	100.52	0.059	0.016	0.131	0.859	931.9	68.8	20.7
LO-15-1	14.2	Medium-grained OAN	Hm-ilm + Mt	n=4	42.38	22.23	35.06	0.58	1.64	100.10	0.060	0.012	0.211	0.772	1188.2	144.9	8.8
LO-21	20.7	Medium-grained Nelsonite	Hm-ilm + Mt	n=3	41.60	23.22	34.45	0.46	1.49	98.98	0.055	0.010	0.219	0.765	1030.4	111.9	2.8
LO-22	21.5	Coarse-grained-OAN	Hm-ilm + Mt	n=3	40.55	24.70	35.09	0.28	0.75	99.08	0.028	0.006	0.235	0.757	1061.8	5.0	2.0
LO-24	28.2	Medium-grained OAN	Hm-ilm + Mt	n=4	43.72	19.58	36.83	0.51	1.24	100.13	0.046	0.011	0.185	0.804	937.0	4.2	3.4
LO-26	36.3	Medium-grained OAN	Ilm + Mt	n=4	47.26	12.35	38.42	0.87	1.91	99.83	0.071	0.018	0.117	0.871	503.7	42.2	10.4
LO-29	42.4	Medium-grained OAN	Ilm + Mt	n=3	50.97	9.35	41.11	1.00	2.22	104.01	0.079	0.020	0.086	0.904	399.3	52.5	10.9
LO-32	48.7	Medium-grained OAN	Ilm + Mt	n=3	49.36	10.95	39.68	0.98	2.22	102.43	0.080	0.020	0.102	0.887	463.2	45.1	8.6
LO-35	57.3	Medium-grained OAN	Ilm + Mt	n=3	47.17	12.44	38.33	0.78	2.01	99.70	0.074	0.016	0.119	0.869	562.2	3.7	1.6
LO-39	63.4	Medium-grained OAN	Ilm + Mt	n=4	53.34	8.05	42.28	0.99	2.79	106.90	0.096	0.019	0.073	0.918	384.2	15.5	5.2
LO-40	67.5	Medium-grained OAN	Ilm + Mt	n=3	50.08	10.54	40.04	0.87	2.35	102.92	0.084	0.018	0.096	0.893	438.6	10.8	3.6
LO-41B	70.1	Coarse-grained-OAN	Ilm + Mt	n=3	43.15	14.83	36.19	0.64	1.20	94.66	0.047	0.014	0.148	0.842	578.3	1.2	1.7
LO-43	75.7	Medium-grained OAN	Ilm + Mt	n=4	48.02	11.47	39.21	0.83	1.86	100.41	0.068	0.017	0.108	0.882	478.1	11.4	3.7
LO-44-1	77.1	Medium-grained OAN	Ilm + Mt	n=3	48.95	11.37	39.29	1.02	2.15	101.75	0.078	0.021	0.105	0.883	446.2	13.5	2.7
LO-46	79.0	Medium-grained OAN	Ilm + Mt	n=3	50.49	9.76	40.75	0.81	2.27	103.33	0.081	0.016	0.090	0.900	483.9	3.8	2.4
LO-47	84.2	Medium-grained OAN	Ilm + Mt	n=3	47.83	10.96	39.66	0.80	1.50	99.82	0.056	0.017	0.104	0.888	548.6	13.4	2.6
LO-49	87.8	Medium-grained OAN	Ilm + Mt	n=3	48.25	0.00	49.53	0.70	2.08	100.99	0.076	0.015	0.108	0.881	530.1	6.3	2.9
LO-50	91.2	Medium-grained OAN	Ilm + Mt	n=3	49.98	2.19	47.56	0.81	2.19	103.09	0.079	0.017	0.094	0.896	556.7	5.0	2.9
LO-51	95.8	Medium-grained OAN	Hm-ilm + Mt	n=4	41.77	23.34	34.94	0.51	1.29	99.71	0.048	0.011	0.220	0.767	1206.0	9.0	2.4
LO-55	99.7	Medium-grained OAN	Hm-ilm + Mt	n=5	28.94	49.41	25.76	0.12	0.40	100.12	0.015	0.003	0.463	0.529	2603.0	41.7	16.4
LO-57	102.1	Medium-grained OAN	Hm-ilm + Mt	n=5	25.87	55.35	22.61	0.13	0.53	99.19	0.020	0.003	0.518	0.470	2437.6	28.6	3.7
20PM02	0.0	Medium-grained OAN	Hm-ilm + Mt	n=5	44.60	14.99	36.73	0.60	1.62	98.75	0.062	0.013	0.145	0.843	772.5	5.6	2.6
20PM03	0.0	Massive oxides in anorthosite	Ilm + Mt	n=5	46.70	10.72	40.57	0.61	0.55	99.36	0.021	0.013	0.105	0.892	937.6	166.9	60.1

1598 Major elements in wt.%, FeO and Fe2O3 recalculated from FeOt by charge balance equations; molar fractions of geikielite, pyrophanite, hematite and ilmenite (Xgeik, Xpyr, Xhem, Xilm) calculated
1599 following QUILF algorithm (Andersen et al.1993); trace element in ppm. OAN = Oxide-apatite norite; Hm-ilm = hemo-ilmenite; Ilm = ilmenite; Mt = magnetite.
1600

1601   Table 6. Representative LA-ICP-MS major and trace element analyses of magnetite for samples the Lac à l'Orignal Fe-Ti-P deposit

Detection Limits (33-55µm)														0.047-0.242	1.527-9.987	0.719-2.736
Sample	Depth (m)	Lithology	Oxides	# analysis	SiO$_2$	TiO$_2$	Al$_2$O$_3$	FeO$_t$	Fe$_2$O$_3$	FeO	MnO	MgO	Total	[51]V	[53]Cr	[60]Ni
LO-01	3.7	Medium-grained OAN	Hm-ilm + Mt	n=3	0.40	0.06	0.40	91.98	67.47	31.27	0.01	0.06	99.98	1732.9	29.0	26.9
LO-05	6.4	Coarse-grained OAN	Hm-ilm + Mt	n=3	0.64	0.08	0.50	91.98	68.69	30.17	0.03	0.11	100.52	1596.8	54.6	14.6
LO-06	6.8	Fine-grained OAN dyke	Hm-ilm + Mt	n=3	0.20	0.09	0.49	91.98	67.30	31.42	0.01	0.07	99.89	1781.4	86.8	23.0
LO-09	9.9	Medium-grained OAN	Hm-ilm + Mt	n=3	0.41	0.10	0.62	91.98	68.97	29.92	0.02	0.16	100.66	2307.9	769.6	146.5
LO-15-1	14.2	Medium-grained OAN	Hm-ilm + Mt	n=3	0.04	0.09	0.47	91.98	67.70	31.06	0.02	0.14	100.11	2662.0	1243.9	105.4
LO-15-2	14.4	Medium-grained OAN	Hm-ilm + Mt	n=3	0.15	0.09	0.51	91.98	68.12	30.68	0.02	0.20	100.26	2499.7	842.8	95.8
LO-21	20.7	Medium-grained Nelsonite	Hm-ilm + Mt	n=3	0.00	0.09	0.49	91.98	67.39	31.35	0.01	0.14	99.94	2142.9	930.9	37.1
LO-22	21.5	Coarse-grained OAN	Hm-ilm + Mt	n=4	0.35	0.09	0.58	91.98	68.26	30.56	0.02	0.13	100.31	2133.3	28.1	31.8
LO-24	28.2	Medium-grained OAN	Hm-ilm + Mt	n=4	0.53	0.09	0.54	91.98	68.66	30.20	0.02	0.11	100.52	2313.0	39.5	35.4
LO-26	36.3	Medium-grained OAN	Ilm + Mt	n=3	0.04	0.60	1.03	91.98	70.97	28.12	0.05	0.30	101.61	2604.2	735.8	98.5
LO-29	42.4	Medium-grained OAN	Ilm + Mt	n=3	0.26	0.90	1.19	91.98	73.00	26.29	0.06	0.39	102.61	2568.4	886.3	98.6
LO-32	48.7	Medium-grained OAN	Ilm + Mt	n=3	0.16	0.24	0.64	91.98	68.80	30.08	0.03	0.20	100.59	2395.2	657.3	75.4
LO-35	57.3	Medium-grained OAN	Ilm + Mt	n=3	0.23	0.26	0.56	91.98	68.55	30.30	0.02	0.19	100.47	2206.2	43.9	15.7
LO-39	63.4	Medium-grained OAN	Ilm + Mt	n=4	0.27	0.90	1.02	91.98	72.18	27.04	0.06	0.36	102.23	2492.7	232.5	39.4
LO-40	67.5	Medium-grained OAN	Ilm + Mt	n=3	0.08	0.37	0.72	91.98	69.11	29.80	0.04	0.23	100.72	2426.5	194.7	33.8
LO-41B	70.1	Coarse-grained-OAN	Ilm + Mt	n=3	0.18	0.11	0.58	91.98	67.78	30.99	0.02	0.12	100.09	1999.2	14.5	9.3
LO-43	77	Medium-grained OAN	Ilm + Mt	n=3	0.09	0.46	0.76	91.98	69.49	29.45	0.04	0.24	100.91	2394.6	179.1	32.7
LO-44-1	77.1	Medium-grained OAN	Ilm + Mt	n=3	0.13	0.37	0.83	91.98	69.72	29.25	0.04	0.27	100.97	2219.5	200.3	26.7
LO-46	79	Medium-grained OAN	Ilm + Mt	n=3	0.14	0.43	0.86	91.98	70.08	28.92	0.03	0.30	101.14	2394.9	69.4	22.3
LO-47	84.2	Medium-grained OAN	Ilm + Mt	n=3	0.26	0.35	0.82	91.98	69.83	29.15	0.02	0.21	101.06	2444.8	232.1	26.8
LO-49	87.8	Medium-grained OAN	Ilm + Mt	n=3	0.46	0.34	0.88	91.98	70.83	28.25	0.03	0.30	101.48	2508.3	110.0	27.1
LO-50	91.2	Medium-grained OAN	Ilm + Mt	n=3	0.27	0.17	0.81	91.98	70.50	28.54	0.02	0.29	101.39	2575.6	64.1	29.2
LO-51	95.8	Medium-grained OAN	Hm-ilm + Mt	n=3	0.15	0.08	0.48	91.98	67.48	31.26	0.02	0.12	99.97	2510.4	71.3	35.4
LO-55	99.7	Medium-grained OAN	Hm-ilm + Mt	n=3	0.29	0.10	0.49	91.98	68.20	30.61	0.03	0.12	100.33	3080.4	121.2	197.9
LO-57	102.1	Medium-grained OAN	Hm-ilm + Mt	n=3	0.15	0.08	0.51	91.98	67.73	31.03	0.02	0.16	100.06	2318.5	90.5	61.1
20PM02	0.0	Medium-grained OAN	Hm-ilm + Mt	n=5	0.15	0.09	0.46	92.38	68.18	31.04	0.01	0.12	100.04	2254.3	64.1	26.2
20PM03	0.0	Massive oxides in anorthosite	Ilm + Mt	n=5	0.09	0.08	0.49	92.09	68.05	30.85	0.01	0.05	99.63	3041.1	1960.8	470.2

1602   Major elements in wt.%, FeO and Fe2O3 recalculated from FeOt by charge balance equations; trace element in ppm; OAN = Oxide-apatite norite; Hm-ilm = hemo-ilmenite; Ilm = ilmenite; Mt =
1603   magnetite.

1604

Table 7. Representative LA-ICP-MS major and trace element analyses of apatite for samples the Lac à l'Orignal Fe-Ti-P deposit

Element	REE geochemical analysis of fine-grained OAN dykes				Calculated D_{ap} values			Compilation of D_{ap} values		
	Whole-rock REE values			Apatite REE values		Lac à l'Orignal Fe-Ti-P			Bjerkrein Sokndal Layered Intrusion	
	LO-06	LO-08		LO-06	LO-08	D_{ap}[a]	D_{ap}[a]		D_{ap}[c]	D_{ap}[d]	D_{ap}[e]
La	55.82	73.09		408.0	637.3	7.3	8.7		3.9	4.3	12.0
Ce	141.88	176.40		1139.6	1794.3	8.0	10.2		4.7	5.5	15.0
Pr	21.27	24.38		178.5	280.9	8.4	11.5		5.4	-	-
Nd	103.48	108.58		888.8	1350.7	8.6	12.4		6.0	6.9	19.0
Sm	20.88	21.92		182.6	282.7	8.7	12.9		6.6	7.3	20.0
Eu	5.75	5.60		44.4	44.8	7.7	8.0		3.9	7.5	13.0
Gd	18.30	17.85		161.2	247.2	8.8	13.8		6.8	7.9	20.0
Tb	2.08	2.18		18.4	29.9	8.8	13.8		6.1	7.7	19.0
Dy	10.72	12.02		94.9	163.9	8.9	13.6		5.3	-	-
Ho	1.80	2.09		16.2	28.8	9.0	13.8		4.6	6.6	16.8
Er	4.33	5.46		38.0	71.6	8.8	13.1		4.0	-	-
Tm	0.50	0.67		4.2	8.3	8.4	12.4		3.4	-	-
Yb	2.72	4.10		22.6	45.5	8.3	11.1		2.7	4	13.0
Lu	0.36	0.60		3.0	6.2	8.4	10.3		2.2	3.25	10.0

a Calculated partition coefficients between apatite and melt from sample LO-06. b Calculated partition coefficients between apatite and melt from sample LO-08. c Partition coefficients between apatite and melt from Charlier et al.(2005). d Partition coefficients between apatite and melt from Roelandts & Duchesne (1979). e Partition coefficients between apatite and melt from Vander Auwera et al.(1998).

10

Electronic Supplementary Material 2 - Complete methods and analytical procedures

Petrogenesis of Fe-Ti-P mineral deposits associated with Proterozoic anorthosite massifs in the Grenville Province: insights from oxide and apatite trace-element geochemistry at Lac à l'Orignal, Quebec, Canada

Pedro Miloski**

Département de Sciences Appliquées, Université du Québec à Chicoutimi (UQAC), 555 Boulevard de l'Université, Chicoutimi, Québec, Canada, G7H 2B1

Corresponding author - E-mail: miloski.geo@gmail.com

Sarah Dare

Département de Sciences Appliquées, Université du Québec à Chicoutimi (UQAC), 555 Boulevard de l'Université, Chicoutimi, Québec, Canada, G7H 2B1

Caroline-Emmanuelle Morisset

Agence spatiale canadienne, 6767 Rte de l'Aéroport, Saint-Hubert, Québec, Canada, J3Y 8Y9

Joshua H.F.L. Davies

Département des sciences de la Terre et de l'atmosphère/GEOTOP, Université du Québec à Montréal (UQAM), 405 Rue Sainte-Catherine Est, Montréal, Québec, Canada, H2L 2C4

Morgann G. Perrot

Département des sciences de la Terre et de l'atmosphère/GEOTOP, Université du Québec à Montréal (UQAM), 405 Rue Sainte-Catherine Est, Montréal, Québec, Canada, H2L 2C4

Dany Savard

Département de Sciences Appliquées/LabMaTer, Université du Québec à Chicoutimi (UQAC), 555 Boulevard de l'Université, Chicoutimi, Québec, Canada, G7H 2B1

ESM2.1 Whole rock lithogeochemistry by fusion-LA-ICP-MS

Whole-rock major and trace elements analyses were carried out by fusion – LA-ICP-MS at LabMaTer, UQAC, following the protocol of Barnes & Mansur (2020). First, the sample powder was fused into glass disks following a conventional XRF major element fusing technique, using a lithium borate mix as a flux (e.g., Perkins *et al*. 1993; Norman *et al*. 2003). The glass disks of silicate rocks were made in a 1:4 ratio by mixing 0.5g of each sample powder with 2g of pre-mixed LiB flux (49.75% $Li_2B_4O_7$ + 49.75% $LiBO_2$ +

0.5% LiBr) provided by CLAISS and 0.5g of ammonium nitrate (NH_4NO_3) in a 1" platinum crucible mould. For oxide-rich samples, the sample:flux ratio increased from 1:4 to 1:10 to ensure complete fusion. The platinum crucible was then placed in a CLAISSE (LeNeo -Beta Version) and the fusion carried out in four distinctive stages, taking 15 minutes before the glass disks was generated. First, the instrument was preheated to 850°C for 3 minutes, before adjusting the temperature to 1050°C for the next 4 minutes and 20 rotation per minute (rpm). Following an increase to 40 rpm the crucible was tilted at 20° to promote homogenization for 3 minutes. The temperature increased to 1100 °C and 35 rpm for the final 3 minutes. Upon complete fusion, the melting product cooled down for 2 minutes before producing the glass disk. The glass disks were mounted in epoxy mounts and polished for analysis by LA-ICP-MS using an Excimer 193nm Resolution M-50 laser ablation system equipped with a double volume cell S-155 and coupled with an Agilent 7900 mass spectrometer. The LA-ICP-MS analyses of the glass disks were determined using a laser frequency of 10 Hz, a power of 4.5 to 5 mJ/pulse, a dwell time of 7.5 to 10 ms, a rastering speed of 5 to 10 μm/s, and a fluence of 3 J/cm². Line scans ablating the surface of each polished glass disk were made with a beam size of 75μm. The gas blank was measured for 25 to 30s before switching on the laser for at least 40s. The ablated material was carried into the ICP-MS by an Ar–He gas mix at a rate of 0.8–1 L/min for Ar and 350 mL/min for He, and 2mL/min of nitrogen was also added to the mixture. Data reduction was carried out using the Iolite software based on semi-quantitative data reduction scheme normalized to 100% oxides for major elements and including loss on ignition (LOI) (Paton *et al.* 2011). A series of reference materials, international and in-house, (listed in Table A.1) were prepared using the same fusion method to 1) us for calibration (an in-house MIX-KPT-610) and 2) monitor the quality of the results for silicate rocks and glasses (KPT-1, OKUM, LK-NIP, GEOPT-23, GEOPT-25, GEOPT-34, AN-G, GSE, NIST 610), Fe-Ti oxides (BC-28, AMIS-0454, NIST27f) and 3 Fe-Ti-P mineralised rocks, from the study of Grant (2020) previously analysed in commercial labs by XRF, INAA and ICP-MS. A glass disk of NIST-616 was prepared and analysed as an approximation of a procedural blank as this synthetic glass contains sub ppm levels of most trace elements. The results are within the accepted range of working values and the reference materials data and limits of detection (LOD) are reported in Table A.1 and summarised in Fig. A.1.
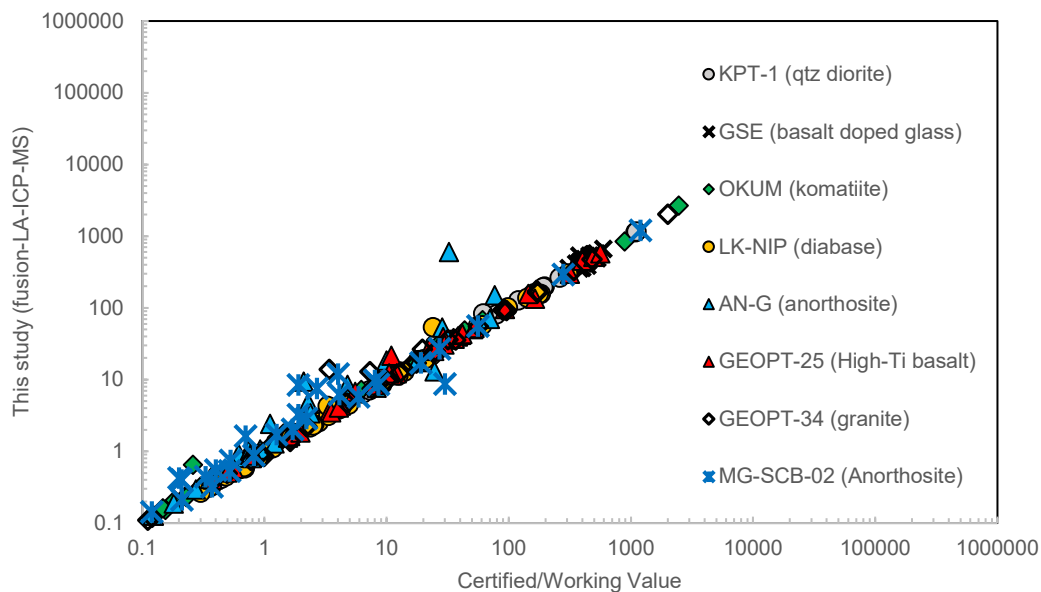
Figure 1. Comparison between certified/working values and the respective values obtained for LA-ICP-MS analysis of reference materials in this study.

ESM2.2 Mineral Chemistry by LA-ICP-MS

Forty-eight trace-element concentrations [Li, Na, Mg, Al, Si, P, Cl, K, Ca, Sc, Ti, V, Cr, Mn, Fe, Co, Ni, Cu, Zn, Ga, Ge, Rb, Sr, Y, Zr, Nb, Cs, Ba, La, Ce, Pr, Nd, Sm, Eu, Gd, Tb, Dy, Ho, Er, Tm, Yb, Lu, Hf, Ta, W, Pb, Th and U] in plagioclase (n=168), magnetite (n=88), ilmenite (n=108) and apatite (n=132) were determined in-situ for 38 samples using an Excimer 193nm Resolution M-50 laser ablation system, equipped with a double volume cell S-155, and coupled with an Agilent 7900 mass spectrometer at LabMaTer, UQAC. The LA-ICP-MS tuning parameters were a laser frequency of 10 Hz, a power of 4.5 to 5 mJ/pulse, a dwell time of 7.5 to 10 ms, a rastering speed of 5 to 10 μm/s, and a fluence of 3 J/cm^2. Line scans across the surface of 3-5 grains (per mineral) per polished thinsection were made with beam sizes ranging from 33-55μm according to the size of the grain. The gas blank was measured for 25 to 30s before switching on the laser for at least 40s. The ablated material was carried into the ICP-MS by an Ar–He gas mix at a rate of 0.8–1 L/min for Ar and 350 mL/min for He, and 2mL/min of nitrogen was also added to the mixture.

Data reduction was carried out using Iolite 4 (Iolite Software, The University of Melbourne), based on semi-quantitative data reduction scheme, normalized to 100% oxides (Paton *et al.* 2011) for plagioclase and ilmenite. Magnetite data was treated using the traditional normalization using a fixed Fe value, close to stoichiometry, obtained by microprobe for a few samples. Due to the low-Ti concentration of magnetite in all samples (< 0.5 wt.%), there is no substantial change in the Fe content which is close to stoichiometry (72 wt.%). In the same way, apatite data was normalized using a fixed Ca value (give value, close to stoichiometry) obtained by microprobe for a few samples. In contrast, a semi-quantitative data reduction scheme (i.e. normalising to 100% of the major elements without fixing an internal standard) was carried out for minerals (plagioclase and ilmenite) that show extensive solid-solution and exsolution lamellae. Due to the difference in beam size and area that sampled between LA-ICP-MS (line of 50um x 300um) and EPMA (5-10 um beam) techniques, exsolutions of K-rich anti-perthite in plagioclase and hematite exsolutions in (hemo)-ilmenite are not similarly sampled during analysis, therefore leading to inaccurate values for internal standardization of LA-ICP-MS data using EMPA results. For the oxide minerals the recalculation of Fe total to FeO and Fe$_2$O$_3$ contents, required to balance the total to 100%, was carried out using charge balance spreadsheet. The Xhem content in ilmenite was calculated using the QUILF program (Anderson et al. 1993). For plagioclase, the molar proportions of An-Ab-Or was calculated using the EPMA spreadsheet for charge balance. Comparison between LA-ICP-MS results and SEM-EMPA results is given below in Section A.4.

International reference materials used for calibration and to monitor the data quality for each mineral protocol are presented in Table A.1. NIST-610 glass was used to calibrate plagioclase and apatite whereas the Fe-rich GSE glass was used to calibrate ilmenite and magnetite. NIST-612, NIST-614, NIST-616, G-PROBE-6 and GSD were used as monitors for plagioclase. NIST-612, NIST-614, NIST-616, G-PROBE-6, GSD, MAPS-4 as well as in-house reference material UQAC-APA (apatite concentrate) were used as monitors for apatite. NIST-612, NIST-614, NIST-616, G-PROBE-6, GSD as well as in-house reference

materials BC-28 (massive magnetite), AMIS-0454 (massive ilmenite) were used as monitors for oxides (Appendix – Table A.2). The results are within an accepted range of working values (<10% Relative difference; <10% RSD) as shown in Fig. A.2.
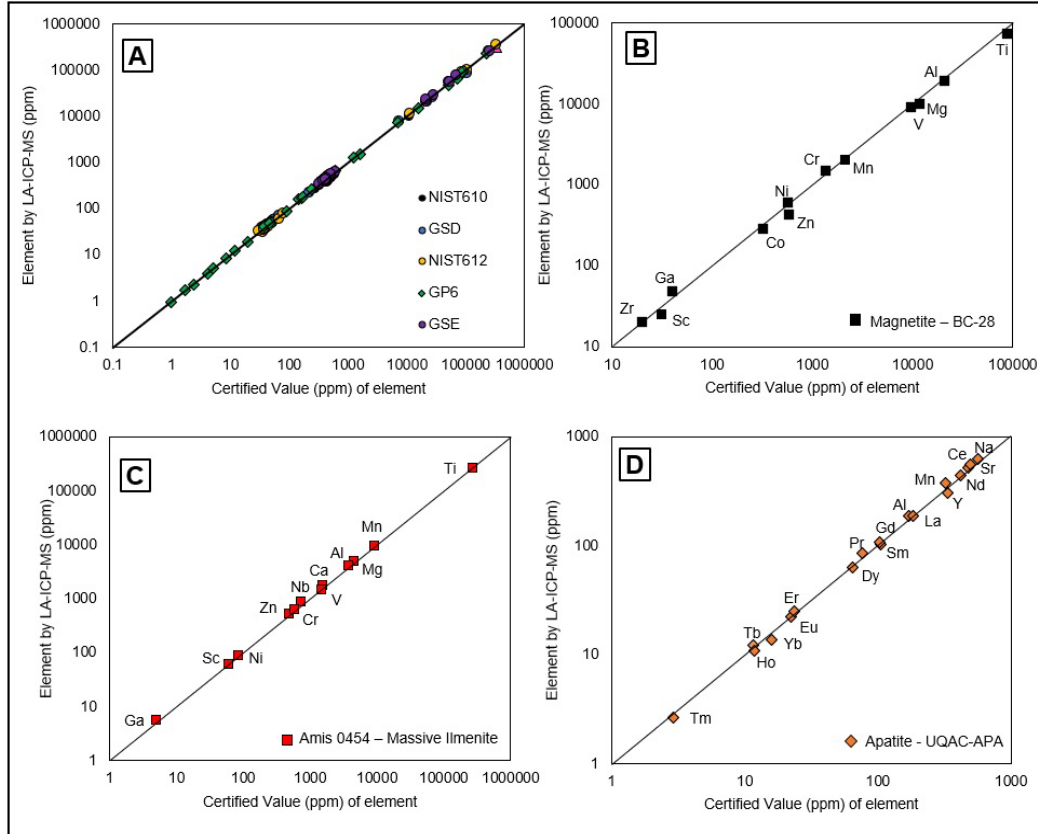

Figure 2. Comparison between LA-ICP-MS results obtained for different reference materials (RM)and their respective certified values. A. International glass reference materials. B. In-house magnetite RM (BC28). C. International ilmenite RM (Amis 0454). D. In-house apatite RM (UQAC-APA). Values are accurate and precise (<10% relative standard deviation and relative difference).

ESM2.3 Trace element mapping of oxides by LA-(TOF) ICP-MS

One mineralized sample was selected for detailed trace-element mapping of Fe-Ti-oxides using a 193nm laser (Applied Spectra, California), equipped with a large double-volume cell (Laurin Technic, Australia), coupled with a time of flight (TOF) ICP-MS (TOFWERK, Switzerland) at LabMaTer, UQAC. The LA-TOF-ICP-MS, developed at LabMaTer, allows a fast and high- resolution mapping (Savard et al. accepted). The LA-ICP-TOF-MS tuning parameters were a laser frequency of 60Hz, a fluence of 6 J/cm^2 and a displacement speed of 100um/s. A beam size of 9 um was used to make a high-resolution map size of 1.3mm x 1.3mm, with 145 lines of analysis of 13 seconds each, for a total acquisition time of 55 minutes. Calibration was done using a mix of different standards: GSD-1g, GSE-1g, UQAC-FeS-1 (sulfide RM) and UQAC-APA-1 (apatite RM), following the protocol of Savard et al. (accepted). 2970 extractions were co-

added which produce extraction cycle of 90ms. Oxides and double-charged interference formation were monitored from $^{248}ThO^+/^{232}Th^+$ and $^{137}Ba^{+2}/^{137}Ba^+$ respectively, and both were <1%. The baseline was subtracted using Tofware software (TOFWERK), and data reduction was completed using IOLITE v4, applying a semi-quantitative scheme with normalization to 100% (Savard et al. accepted).

ESM2.4 Electron microprobe and scanning electron microscope

Analyses of major and minor elements were determined in plagioclase, orthopyroxene, biotite, magnetite, ilmenite, spinel and apatite of 15 samples by electron microprobe analysis at Université Laval (ULaval), Quebec, using a CAMECA SX-100 EPMA, equipped with five wavelength-dispersive spectrometers (WDS). Beam size was 10 μm with a voltage of 15 kV and a current of 20 nA. The defocussed beam was chosen to ensure that any fine grained exsolutions were incorporated into the analysis and also to limit the affect of volatile diffusion during the analysis of apatite. The background was measured for 15–20 s on both sides and a peak counting time of 10 s was carried out. The mix of synthetic and natural materials were used for calibration: Apatite (P, Ca, F), quartz (Si), tugvz (Cl), hematite (Fe), LaPO₄ (La), CePO₄ (Ce), rut (Ti), PrPO₄ (Pr), NdPO₄ (Nd) and chalcopyrite (S). The calculated cationic proportion, the recalculation of Fe^{+2}/Fe^{+3} ratios, and molar proportions of An-Ab-Or contents in plagioclase were done using charge balance spreadsheets provided by the probe operator.

Thirteen samples covering the entire borehole stratigraphy were selected for energy-dispersive micro-X-Ray spectrometry (EDX) analysis at Université Laval (ULaval). Beam size was 10 μm with a voltage of 15 kV and a current of 20 nA, for an acquisition time of 120s. EDX analysis of areas of 500 x 500μm in ilmenite and hemo-ilmenite grains (n=44) were made instead of punctual analysis (used for the other minerals) in a way to obtain an average major composition due to the presence of high-hematite exsolutions, for direct comparison with the LA-ICP-MS data (Fig. A.3).
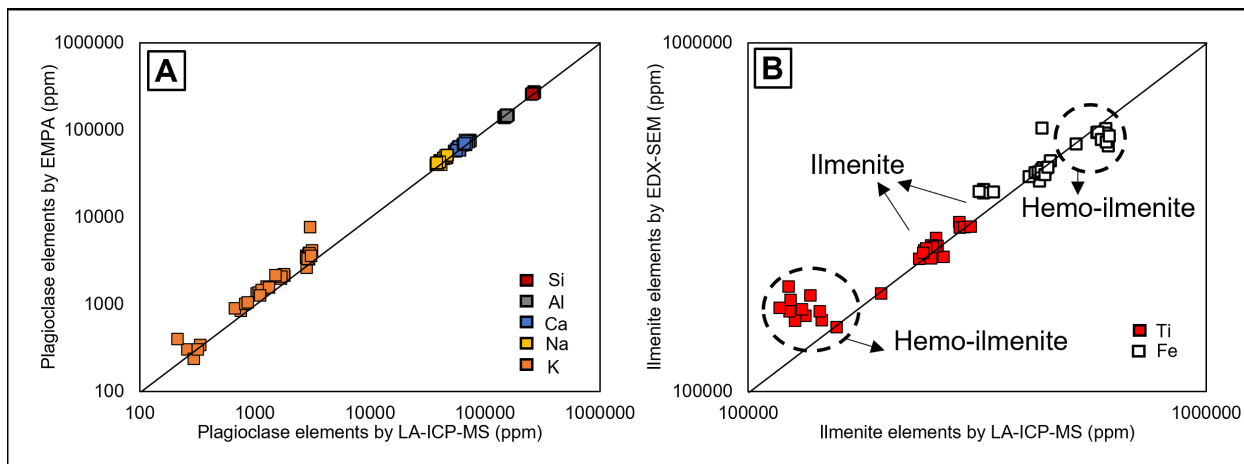
Figure 3. Semi-quantitative LA-ICP-MS results, normalized to 100%, analyses of (A) plagioclase compared to results of electron microprobe (EMPA) and (B) (hemo)-ilmenite compared to results from EDX-SEM for the Lac a L'Orignal samples. Plagioclase and ilmenite are in good agreement (<10% relative standard deviation) with their analysis by EMPA and EDX-SEM, respectively. However, hemo-ilmenite grains with large hematite lamellae are very heterogeneous and there is a lower agreement between SEM and LA-ICP-MS results compared to the other ilmenite grains (<25% relative standard deviation).

ESM2.5. Geochronology

Zircon separation, preparation and U-Pb analysis were conducted in GEOTOP labs at the Université du Québec à Montréal. About 2kg per sample was cleaned and then crushed in a jaw crusher before being sieved to under 250 microns. The resulting rock powder was passed over a Wilfley table using a similar approach to Rocha *et al.* (2020), where the sample is introduced to the Wilfley table one spoonful at a time to ensure that all heavy minerals of all sizes are collected. The zircons were further concentrated using heavy liquids and a Franz isodynamic separator using a current up to 1 ampere. Zircon was then separated from the dense and non-magnetic fraction by hand under a binocular microscope. The selected grains were then annealed in a muffle furnace at 1000 degrees for 48 hours.

Annealed grains were mounted in epoxy and polished before being imaged on a Hitachi S-3400 Variable Pressure SEM at an accelerating voltage of 20 kV using a Centaurus Cathodoluminescence (CL) detector. The acquired CL images were used to guide spot selection for the in-situ analysis. CL images were used to highlight growth zoning, rims overgrowth and inherited cores within individual grains. Most of the samples show zircons with very homogenous textures with oscillatory and sector zoning, however zircons of sample LOR-1, show a bit more complexity with the presence of inherited cores and rims overgrowth. Most of the time, the homogeneous areas of the selected zircons were analysed. We were particularly careful to avoid fractures and inclusions-rich domains within zircon grains. Laser ablation U-Pb analysis was performed using a Nu Attom single collector mass spectrometer attached to a photon machines G2 193nm excimer laser following a procedure adapted from Perrot *et al.* (2017), for details, see table below where metadata are included as recommended by Horstwood *et al.* 2016). Data processing, and down-hole fractionation correction were done using Iolite 4 software, using 91500 (Wiedenbeck *et al.* 1995) as a primary reference material for calibration assuming that the reference material and samples behave identically for laser-induced elemental fractionation correction. Two secondary reference material were analysed: Plešovice and OG1 for quality control and validation purposes. The age obtained for Plešovice was 340 ± 1 (2σ) Ma and of OG1 was $3476 \pm 9(2\sigma)$, which are respectively in good agreement with their known age (Sláma et al., 2008; Bodorkos et al, 2009). Once the raw data were processed, Concordia diagrams and weighted mean ages were plotted and treated through Isoplot R (Vermeesch, 2018) software.

Data reporting table for LA-ICP-MS U-Pb analyses

Laboratory & Sample Preparation	
Laboratory name	Geotop, University of Quebec in Montreal
Sample type/mineral	Detrital zircons
Sample preparation	Conventional mineral separation, 1 inch resin mount, 1µm polish to finish
Imaging	Centaurus, Hitachi S-3400N SEM
Laser ablation system	
Make, Model & type	Photon-machines G2
Ablation cell & volume	Helex, 2-volume cells
Laser wavelength (nm)	193 nm
Pulse width (ns)	4 ns
Fluence (J.cm^{-2})	3.18 J.cm^{-2}
Repetition rate (Hz)	6 Hz
Ablation duration (secs)	30 secs

Ablation pit depth / ablation rate	Not available
Spot diameter (μm)	30 μm
Sampling mode / pattern	Static spot ablation
Carrier gas	100% He in the cell,
Cell carrier gas flow (l/min)	0.7 l/min He in the 1st volume cell
	0.5/min He in the 2nd volume cell

ICP-MS Instrument

Make, Model & type	ICP-MS (Attom, Nu Instruments)
Sample introduction	Ablation aerosol from laser to torch
RF power (W)	1300W
Make-up gas flow (l/min)	0.3 L/min Ar mixed along the sample transport line to the torch
	3 ml/min N2 also added before torch
Detection system	single ion counter
Masses measured	202, 204, 206, 207, 208, 232, 235, 238.
Integration time per peak/dwell times (ms)	500ms for each isotope
Total integration time per output datapoint (secs)	~0.9secs
'Sensitivity' as useful yield (%, element)	0.4% U (NIST610 = 500ppm, #atoms sampled: 500ppm*85um*3Hz*3J/cm^2, #ions detected: >25 mcps)
IC Dead time (ns)	25 ns

Data Processing

Gas blank	15 second on-peak zero subtracted
Calibration strategy	91500 used as primary reference material,
Reference Material info	91500 (Wiedenbeck et al. 1995)
Data processing package used / Correction for LIEF	Iolite4 and IsoplotR softwares. laser-induced elemental fractionation correction assumes reference material and samples behave identically.
Mass discrimination	N/A - Down-hole effect with iolite.
Common-Pb correction, composition and uncertainty	No common-Pb correction applied to the data.
Uncertainty level & propagation	Ages are quoted at 1s absolute, propagation is by quadratic addition. Reproducibility and age uncertainty of reference material are propagated where appropriate.
Quality control / Validation	Plesovice, R33, OG1

References

Bodorkos S, Stern R.A, Kamo S, Corfu F, Hickman AH. 2009. OG1: a natural reference material for quantifying SIMS instrumental mass fractionation of Pb Isotopes during zircon dating. InAGU Fall Meeting Abstracts 2009 Dec (Vol. 2009, pp. V33B-2044).

Barnes, S. J., Mansur, E. T., Pagé, P., Meric, J., & Arguin, J. P. 2020. Major and trace element compositions of chromites from the Stillwater, Bushveld and Great Dyke intrusions compared with chromites from komatiites, boninites and large igneous provinces.

Norman, M., Robinson, P., & Clark, D. 2003. Major-and trace-element analysis of sulfide ores by laser-ablation ICP–MS, solution ICP–MS, and XRF: new data on international reference materials. The Canadian Mineralogist, 41(2), 293-305.

Paton, C., Hellstrom, J., Paul, B., Woodhead, J., & Hergt, J. (2011). Iolite: Freeware for the visualisation and processing of mass spectrometric data. Journal of Analytical Atomic Spectrometry, 26(12), 2508-2518.

Perkins, W. T., Pearce, N. J. G., & Jeffries, T. E. 1993. Laser ablation inductively coupled plasma mass spectrometry: a new technique for the determination of trace and ultra-trace elements in silicates. Geochimica et Cosmochimica Acta, 57(2), 475-482.

Perrot, M., Tremblay, A., David, J., 2017. Detrital zircon U-Pb geochronology of the Magog Group, southern Quebec–stratigraphic and tectonic implications for the Quebec Appalachians. Am. J. Sci. 317 (10), 1049–1094

Rocha, B.C, Davies J.H.F.L., Janasi V.A., Schaltegger U, Nardy A.J.R., Greber N.D, Lucchetti A.C.F,. Polo L.A. 2020. Rapid eruption of silicic magmas from the Paraná magmatic province (Brazil) did not trigger the Valanginian event. Geology; 48 (12): 1174–1178. doi: https://doi.org/10.1130/G47766.1

Sláma J, Košler J, Condon DJ, Crowley JL, Gerdes A, Hanchar JM, Horstwood MS, Morris GA, Nasdala L, Norberg N, Schaltegger U. 2008. Plešovice zircon—a new natural reference material for U–Pb and Hf isotopic microanalysis. Chemical Geology. Mar 30;249(1-2):1-35.

Vermeesch, P., 2018, IsoplotR: a free and open toolbox for geochronology. Geoscience Frontiers, v.9, p.1479-1493, doi:10.1016/j.gsf.2018.04.001.

Electronic Supplementary Material 3 – Supplementary figures

Petrogenesis of Fe-Ti-P mineral deposits associated with Proterozoic anorthosite massifs in the Grenville Province: insights from oxide and apatite trace-element geochemistry at Lac à l'Orignal, Quebec, Canada

Pedro Miloski**

Département de Sciences Appliquées, Université du Québec à Chicoutimi (UQAC), 555 Boulevard de l'Université, Chicoutimi, Québec, Canada, G7H 2B1

Corresponding author - E-mail: miloski.geo@gmail.com

Sarah Dare

Département de Sciences Appliquées, Université du Québec à Chicoutimi (UQAC), 555 Boulevard de l'Université, Chicoutimi, Québec, Canada, G7H 2B1

Caroline-Emmanuelle Morisset

Agence spatiale canadienne, 6767 Rte de l'Aéroport, Saint-Hubert, Québec, Canada, J3Y 8Y9

Joshua H.F.L. Davies

Département des sciences de la Terre et de l'atmosphère/GEOTOP, Université du Québec à Montréal (UQAM), 405 Rue Sainte-Catherine Est, Montréal, Québec, Canada, H2L 2C4

Morgann G. Perrot

Département des sciences de la Terre et de l'atmosphère/GEOTOP, Université du Québec à Montréal (UQAM), 405 Rue Sainte-Catherine Est, Montréal, Québec, Canada, H2L 2C4

Dany Savard

Département de Sciences Appliquées/LabMaTer, Université du Québec à Chicoutimi (UQAC), 555 Boulevard de l'Université, Chicoutimi, Québec, Canada, G7H 2B1

GC-LOR-01
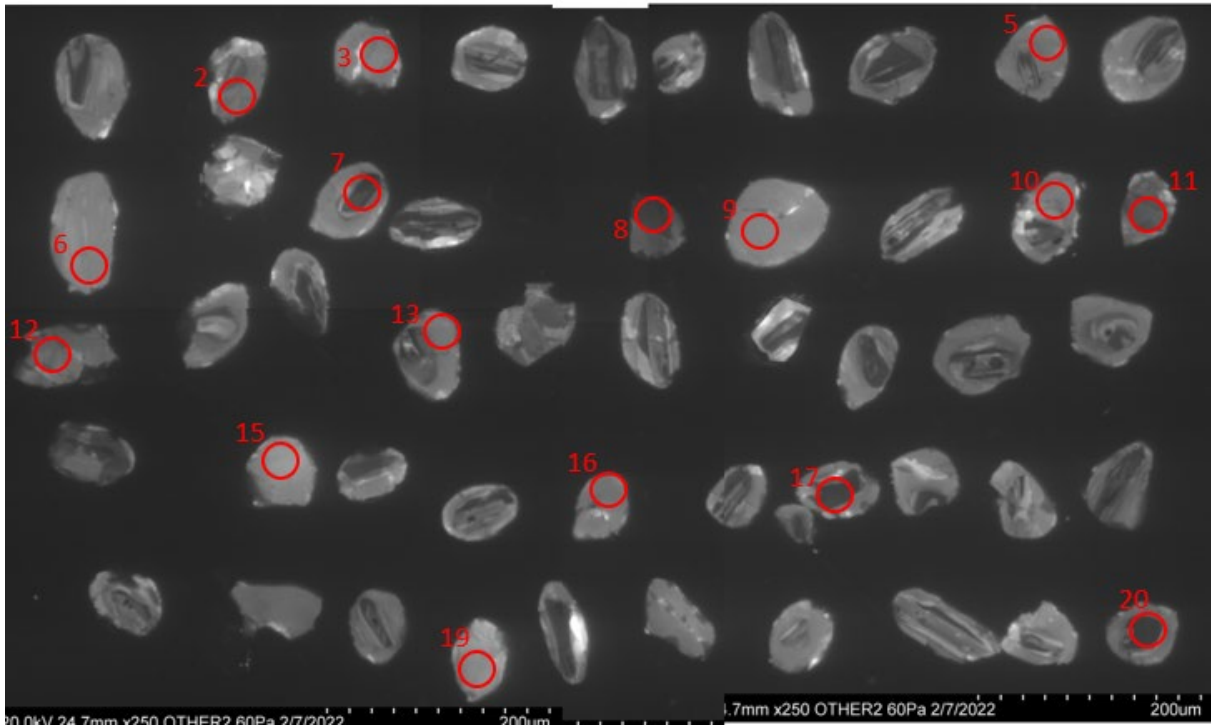
GC-LOR-02
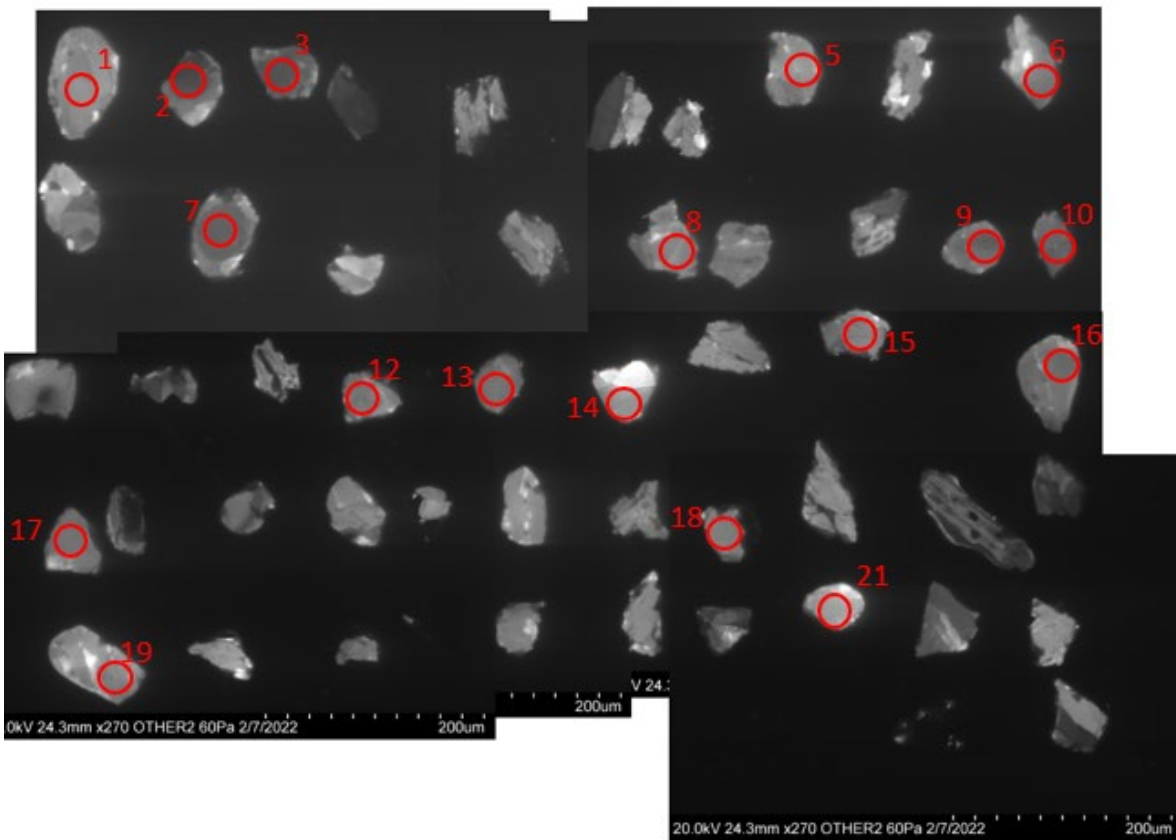
Figure 1. CL Images of selected analyzed zircons.

LOR01
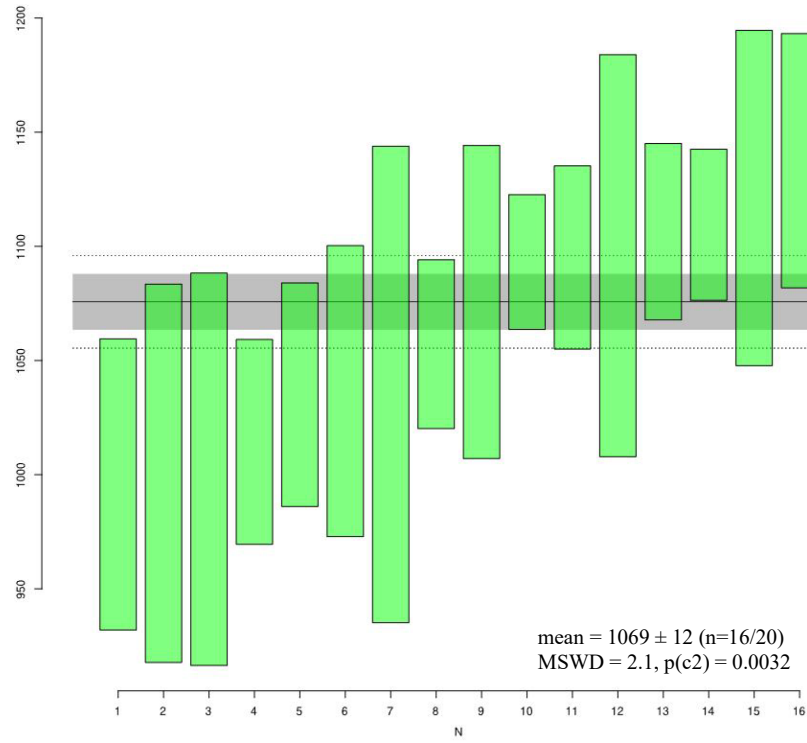
LOR02
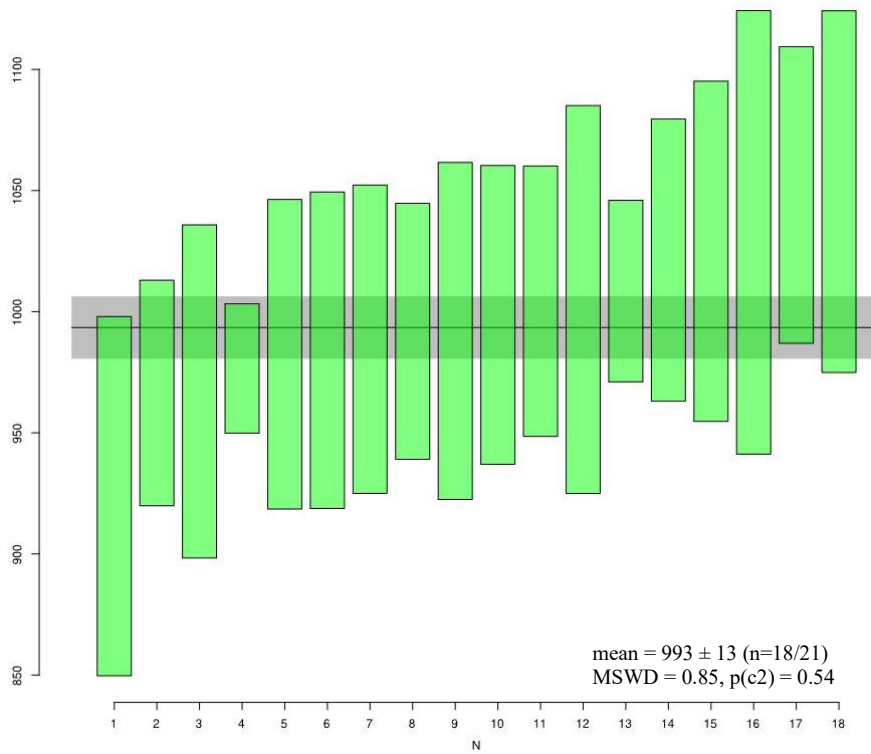
Figure 2. Weighted mean diagrams for LA-ICP-MS U–Pb analysis in zircon Each bar represents the result of the analysis of a single grain.
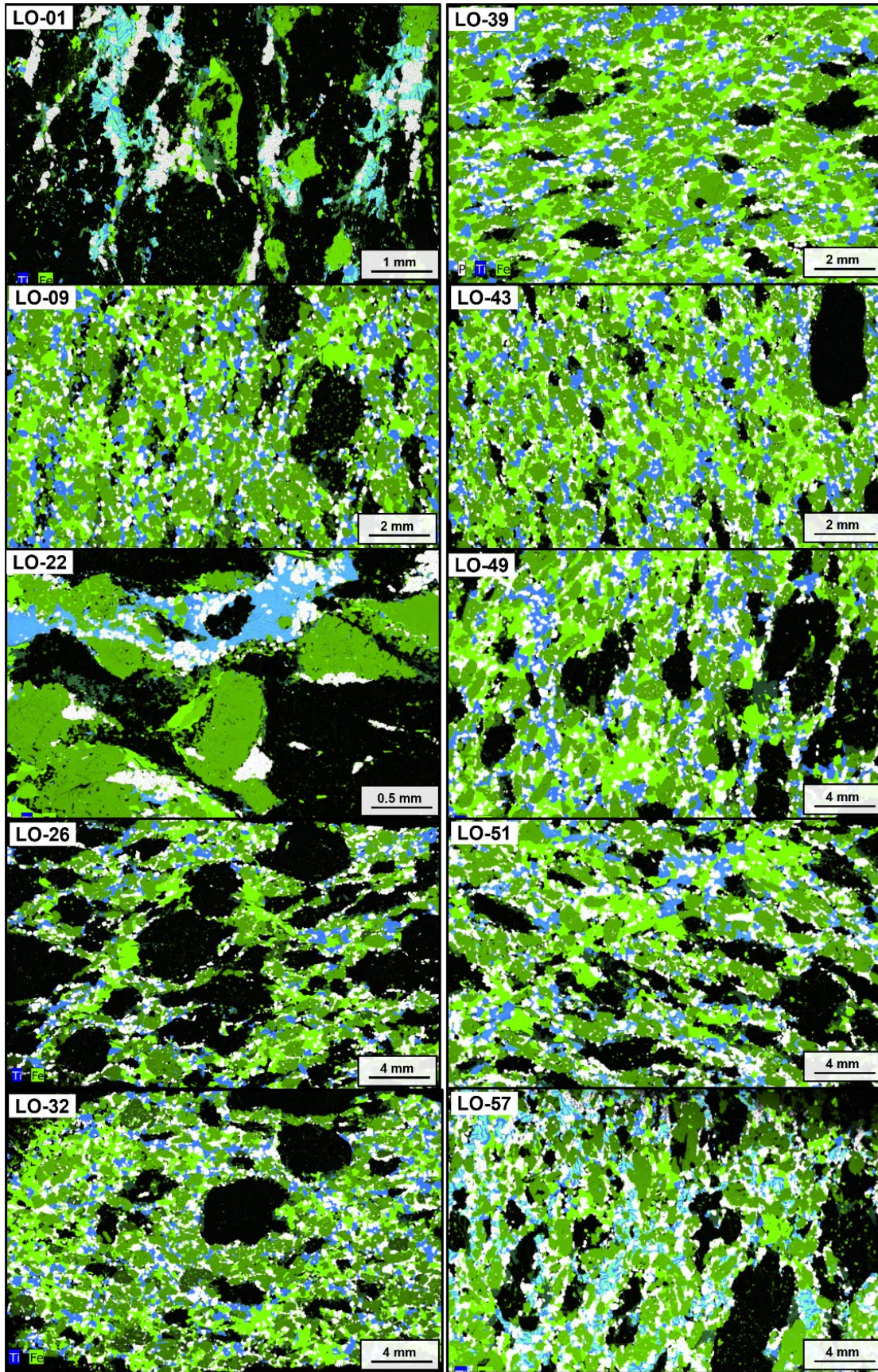
Figure 3. µXRF-maps, combining P (white), Ti (blue) and Fe (green), showing the different proportions of oxides and apatite from the Lac à l'Orignal Fe-Ti-P mineralized zone. Ilmenite is blue, where as hematite-rich part of ilmenite is cyan. Magnetite is bright green. Orthopyroxene/biotite is dark green.
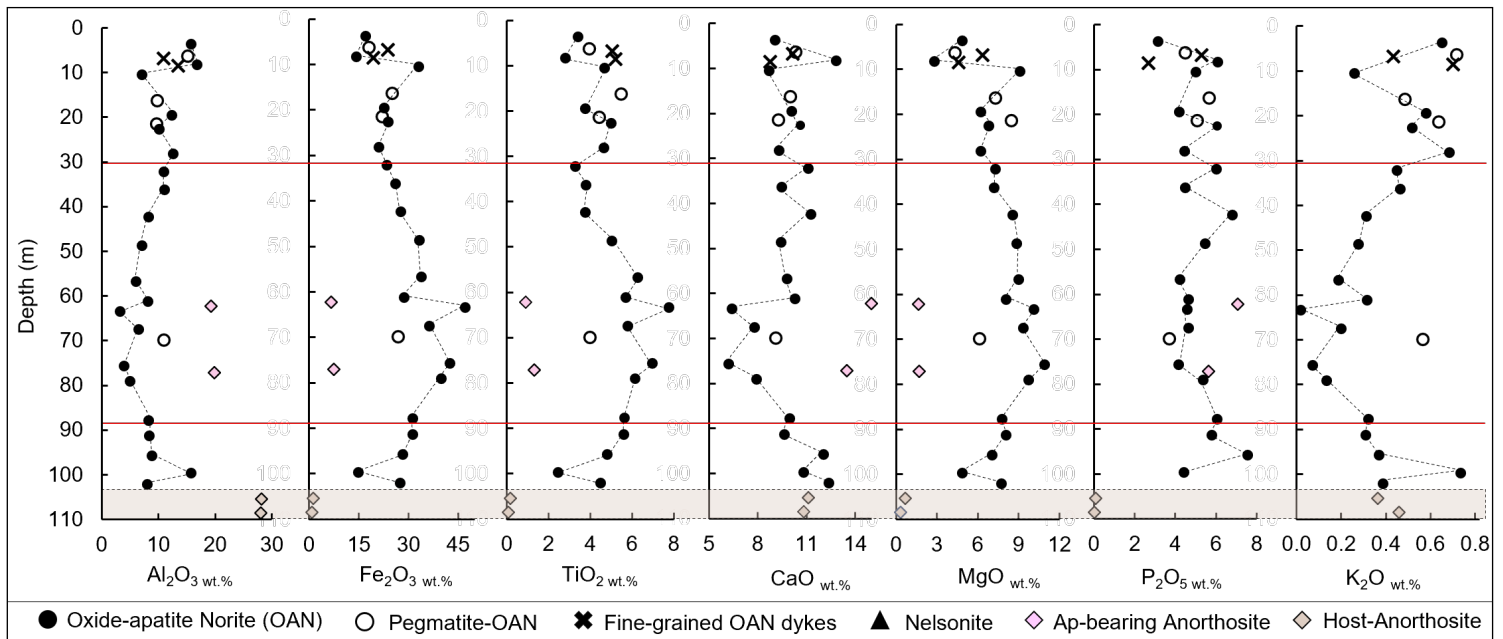
Figure 4. Stratigraphic variation for selected whole-rock major element compositions in hole LO-14-21. The brownish horizon represents the host-anorthosite. Red lines indicating the oxide changing from Hm-ilmenite to Fe-poor ilmenite towards the core of the intrusion. Mineral abbreviations: ap = apatite.
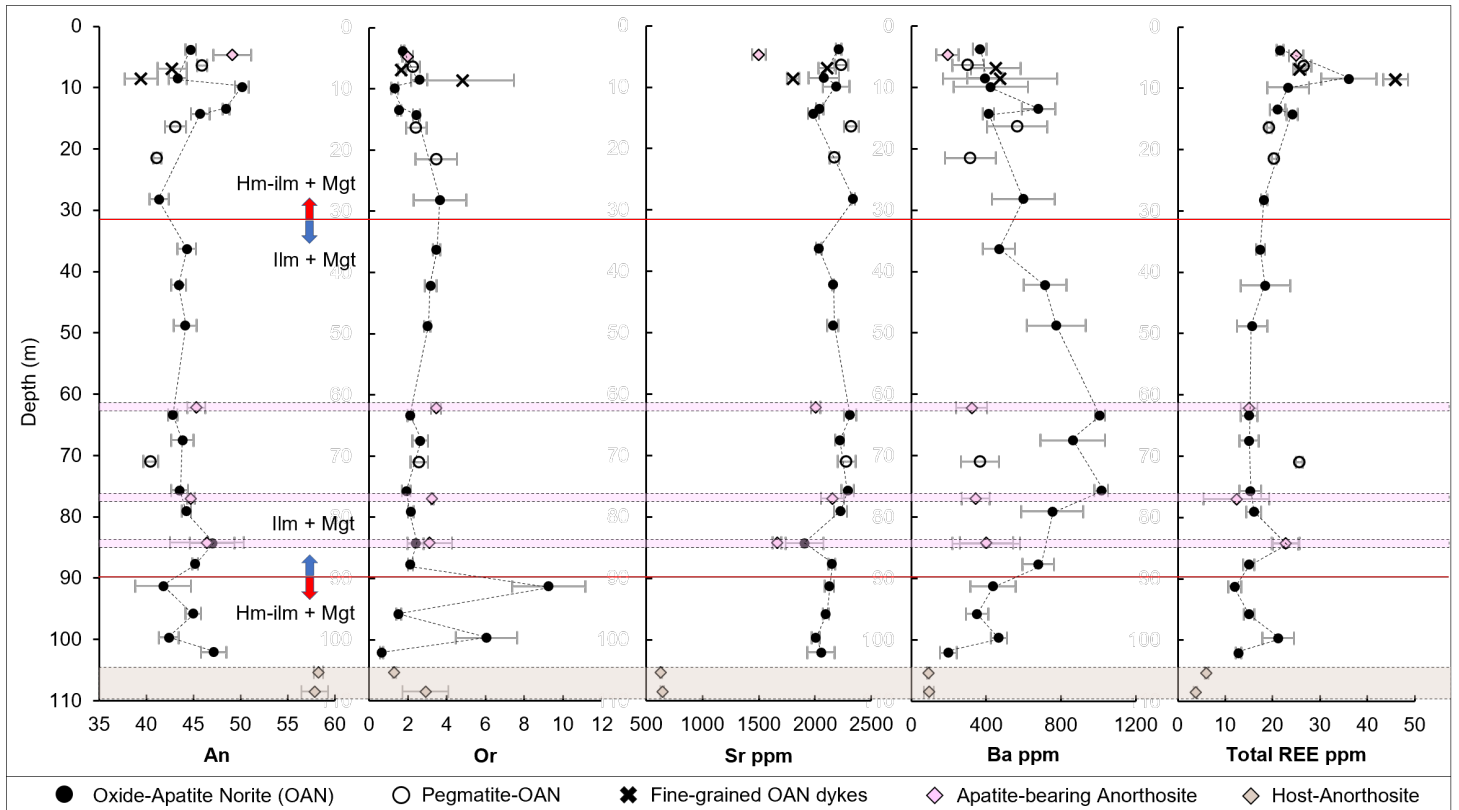
Figure 5. Stratigraphic variation of plagioclase compositions in hole LO-14-21. The pink horizons represent the apatite-bearing anorthosite (pa-C) layers and the brownish horizon the host-anorthosite. Red lines indicating the oxide changing from Hm-ilmenite to Fe-poor ilmenite towards the core of the intrusion. Error bars = 1 standard deviation and represents the natural variation within the thin section.
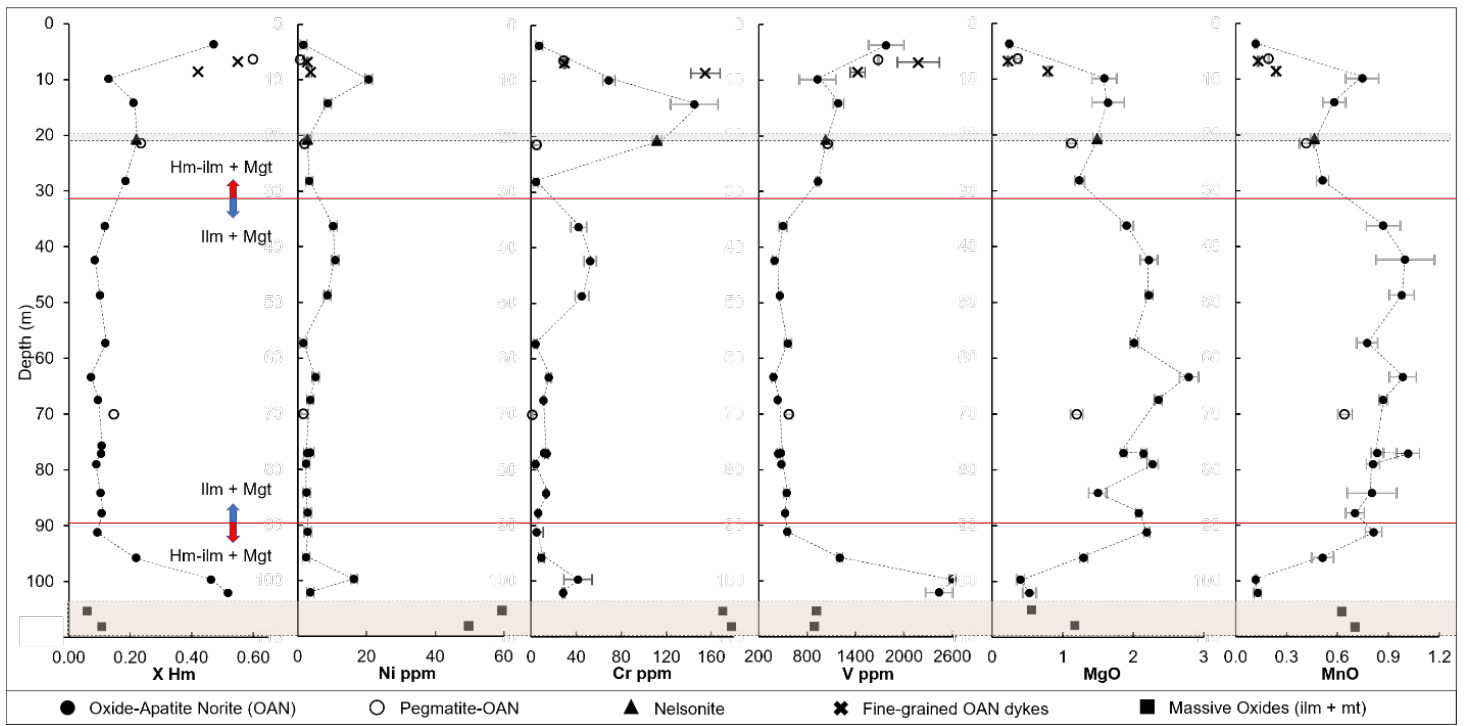
Figure 6. Stratigraphic variation of ilmenite compositions in hole LO-14-21. The grey horizon represents the nelsonite (iap-C) layer. Red lines indicating the oxide changing from Hm-ilmenite to Fe-poor ilmenite towards the core of the intrusion. Error bars = 1 standard deviation and represents the natural variation within the thin section. Mineral abbreviations: ilm = ilmenite; mt = magnetite.
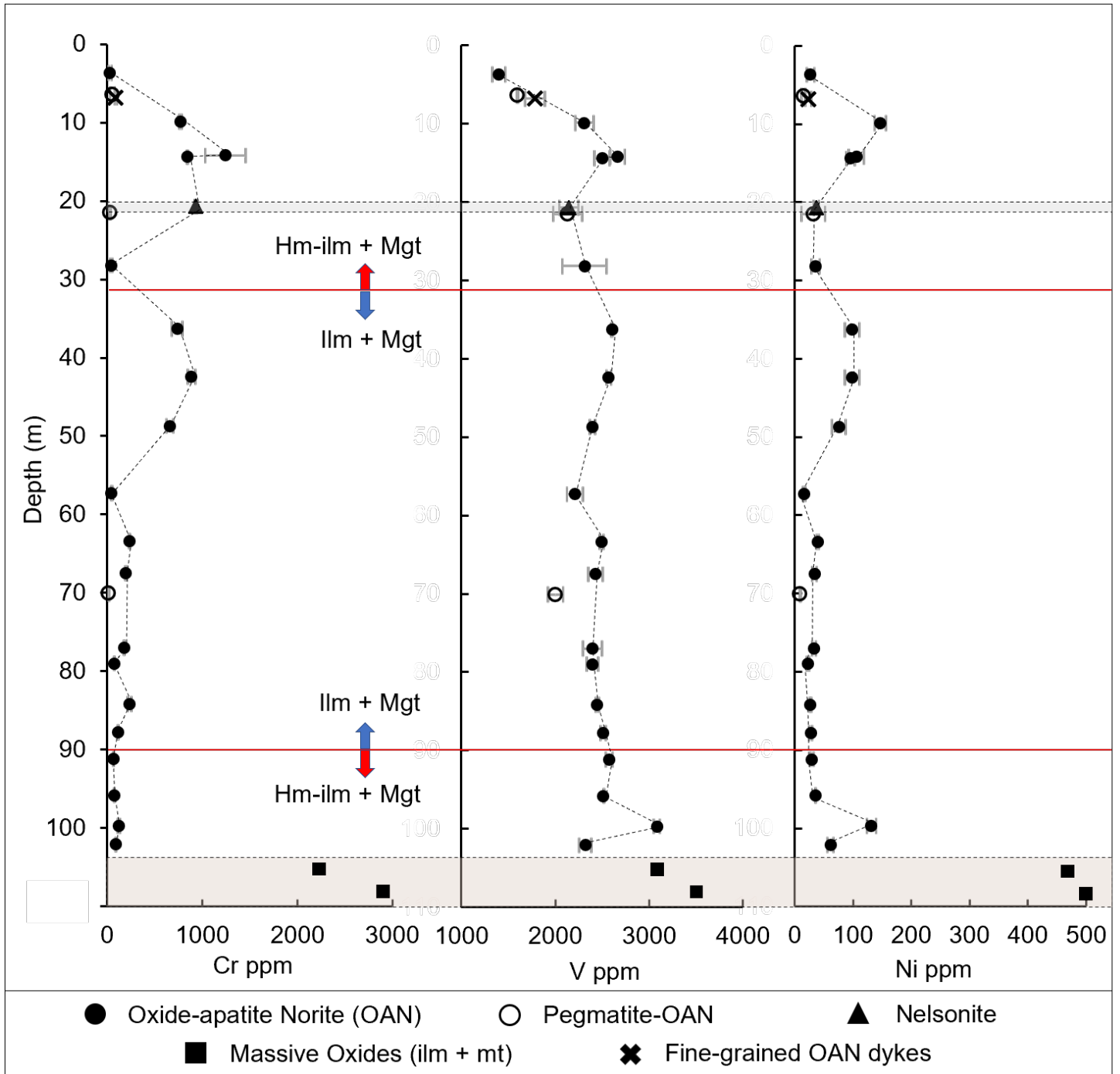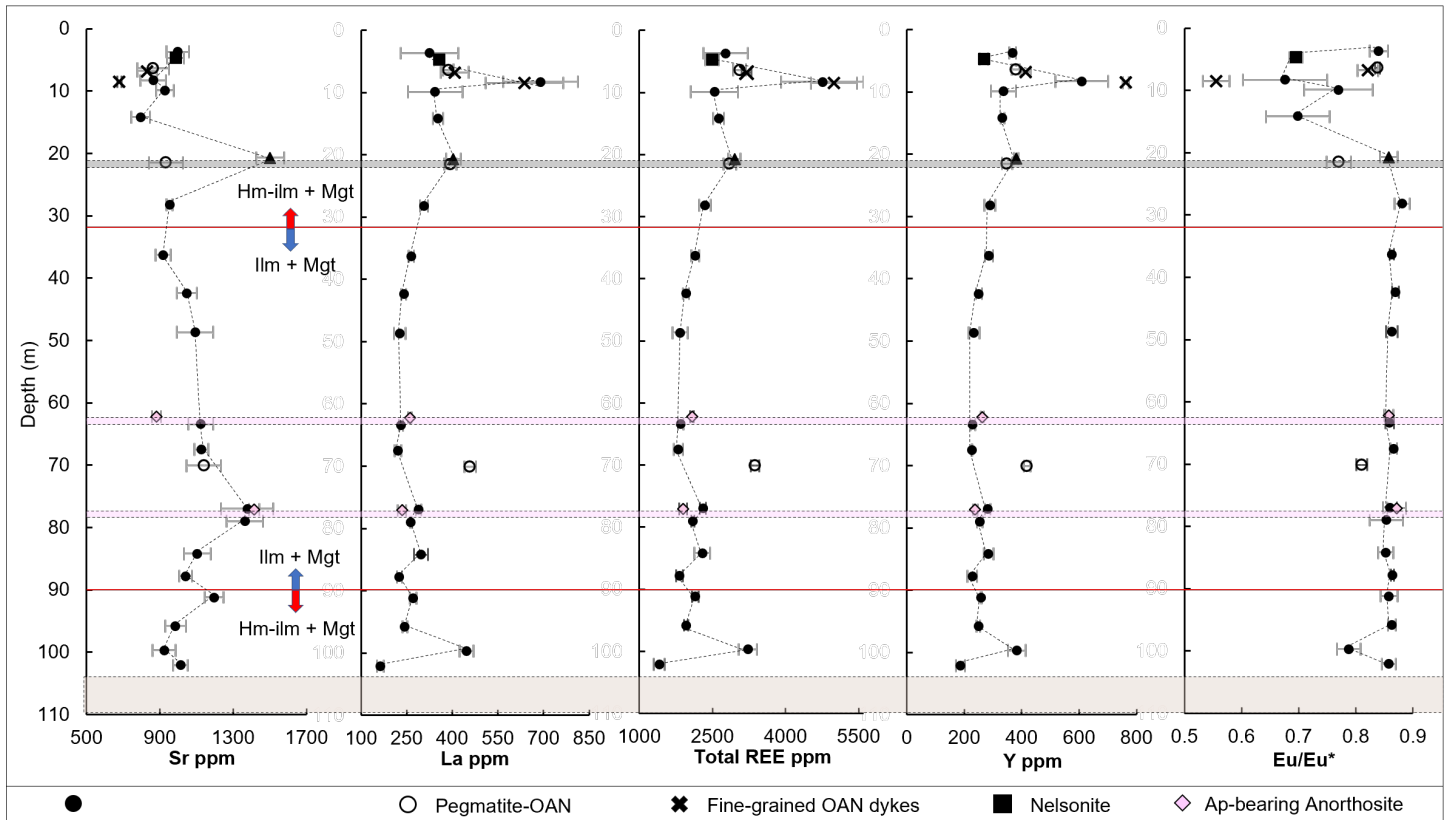
Figure 7. Stratigraphic variation of magnetite compositions in hole LO-14-21. The grey horizon represents the nelsonite (iap-C) layer. Red lines indicating the oxide changing from Hm-ilmenite to Fe-poor ilmenite towards the core of the intrusion. Error bars = 1 standard deviation and represents the natural variation within the thin section. Mineral abbreviations: ilm = ilmenite; mt = magnetite.

Figure 8. Stratigraphic variation of apatite trace-element compositions in hole LO-14-21. The grey horizon represents the nelsonite (iap-C) layer, the pink horizons represent the apatite-bearing anorthosite (pa-C) layers and the brownish horizon the host-anorthosite (apatite-free). Red lines indicating the oxide changing from Hm-ilmenite to Fe-poor ilmenite towards the core of the intrusion. Error bars = 1 standard deviation and represents the natural variation within the thin section. Mineral abbreviations: ap = apatite.
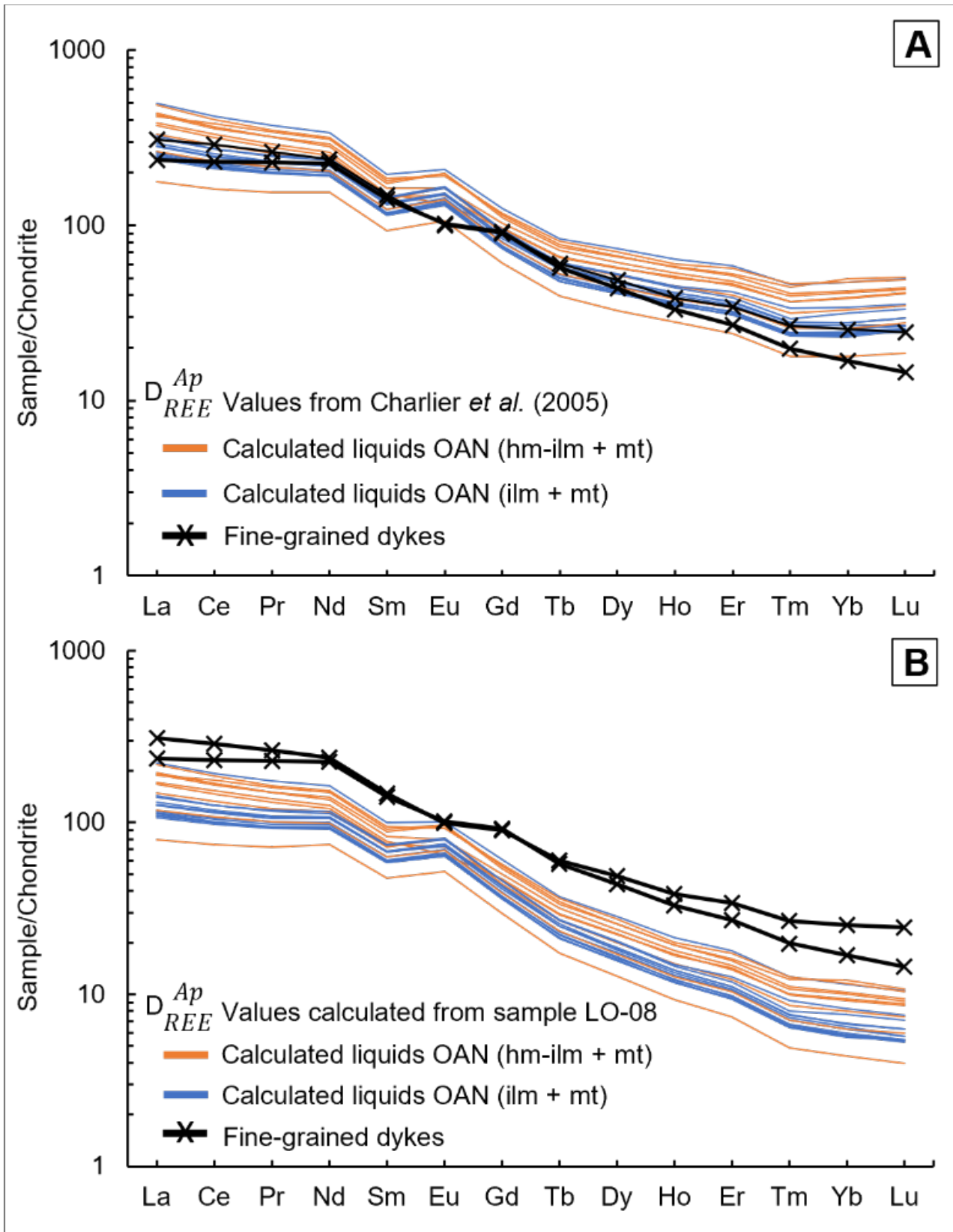
Figure 9. Chondrite-normalized REE patterns (Sun and McDonough,1989) for fine-grained OAN dykes (samples LO-06 and LO-08) compared to calculated liquids from the inversion of apatite compositions of border (orange lines) and core (blue lines) samples. A. Calculated liquids applying partition coefficients for REE between apatite and melt (D_{REE}^{Ap}) from Charlier *et al*. (2005). B. Calculated liquids applying D_{REE}^{Ap} values obtained from the dyke sample LO-08.
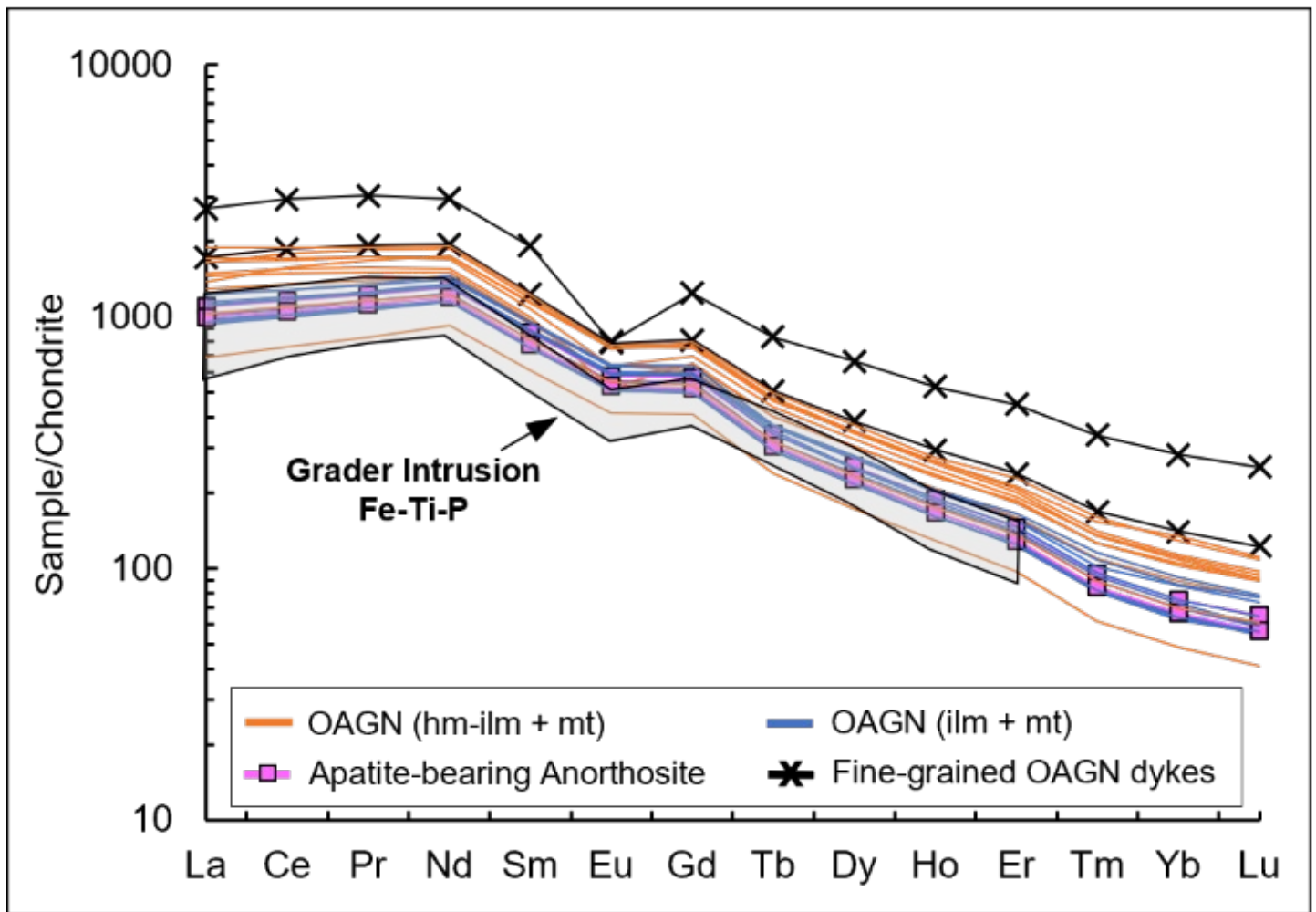
Figure 10. Chondrite-normalized REE compositions of apatites (after Sun and McDonough, 1989) presenting a comparison between the Lac à l'Orignal Fe-Ti-P mineralization (this work) and the Grader Intrusion Fe-Ti-P (grey field) in the Havre Saint Pierre Anorthosite (after Charlier *et al.* 2008).
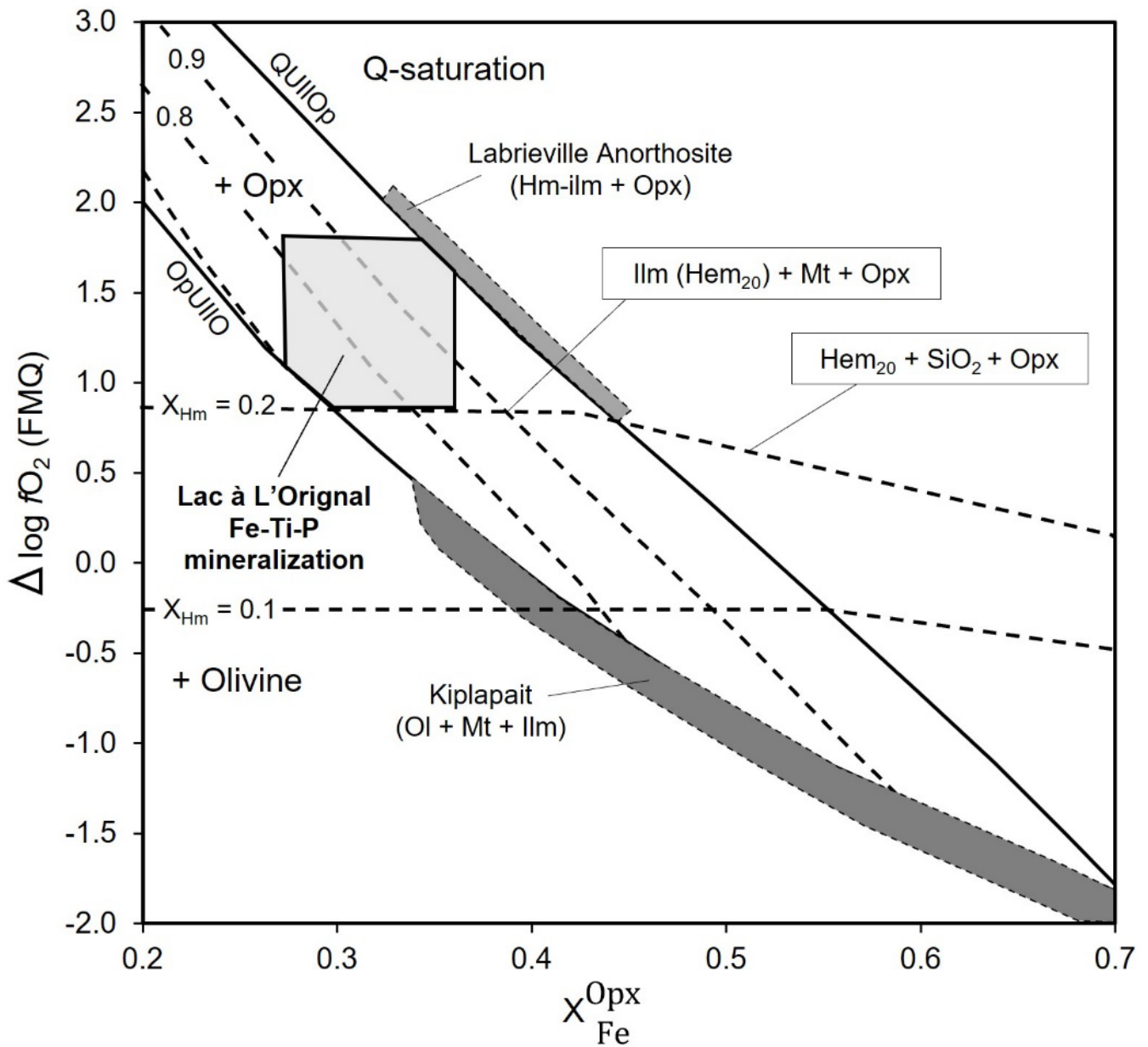
Figure 11. Δ log $f\mathrm{O_2}$ (relative to FMQ) versus $X\mathit{Opx}\,\mathit{Fe}$ diagram (after Frost et al. 2010) showing the crystallization conditions of the fine-grained OAN dykes (probable parental melt) of the Lac à l'Orignal mineralization in comparison with two anorthosite plutons of different silicate/oxide assemblages: the olivine-magnetite-bearing Kiplapait Intrusion (Nain Plutonic Suite, Emslie, 1985) and the hemo-ilmenite-orthopyroxene-bearing Labrieville Anorthosite (Owens & Dymek, 2005). Calculations from the QUILF program of Anderson et al. (1993).
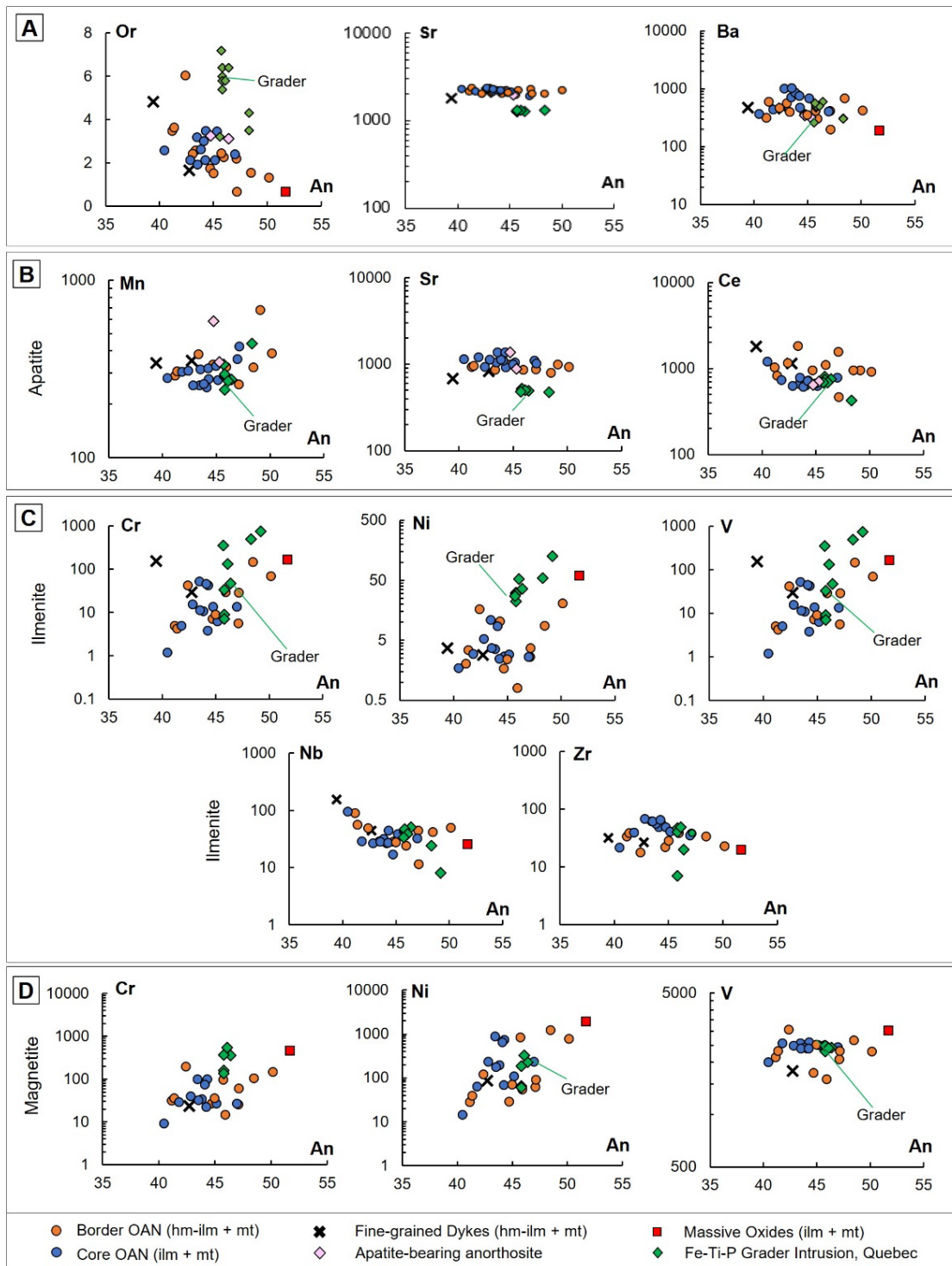
Figure 12. Binary diagrams displaying the An content of plagioclase (as a proxy of fractional crystallization) versus the concentration of major and compatible elements (ppm) in (**A**) plagioclase, (**B**) apatite, (**C**) ilmenite and (**D**) magnetite from Lac à l'Orignal Fe-Ti-P mineralization (this work). Data from the Grader Intrusion Fe-Ti-P, Quebec (Charlier et al. 2008) plotted for comparison. An (mol.%) = 100 [Ca/(Ca+Na+K)] and Or (mol.%) = 100 [K/(Ca+Na+K)]. Mineral abbreviations: hm-ilm = hemo-ilmenite; ilm = ilmenite; mt = magnetite.
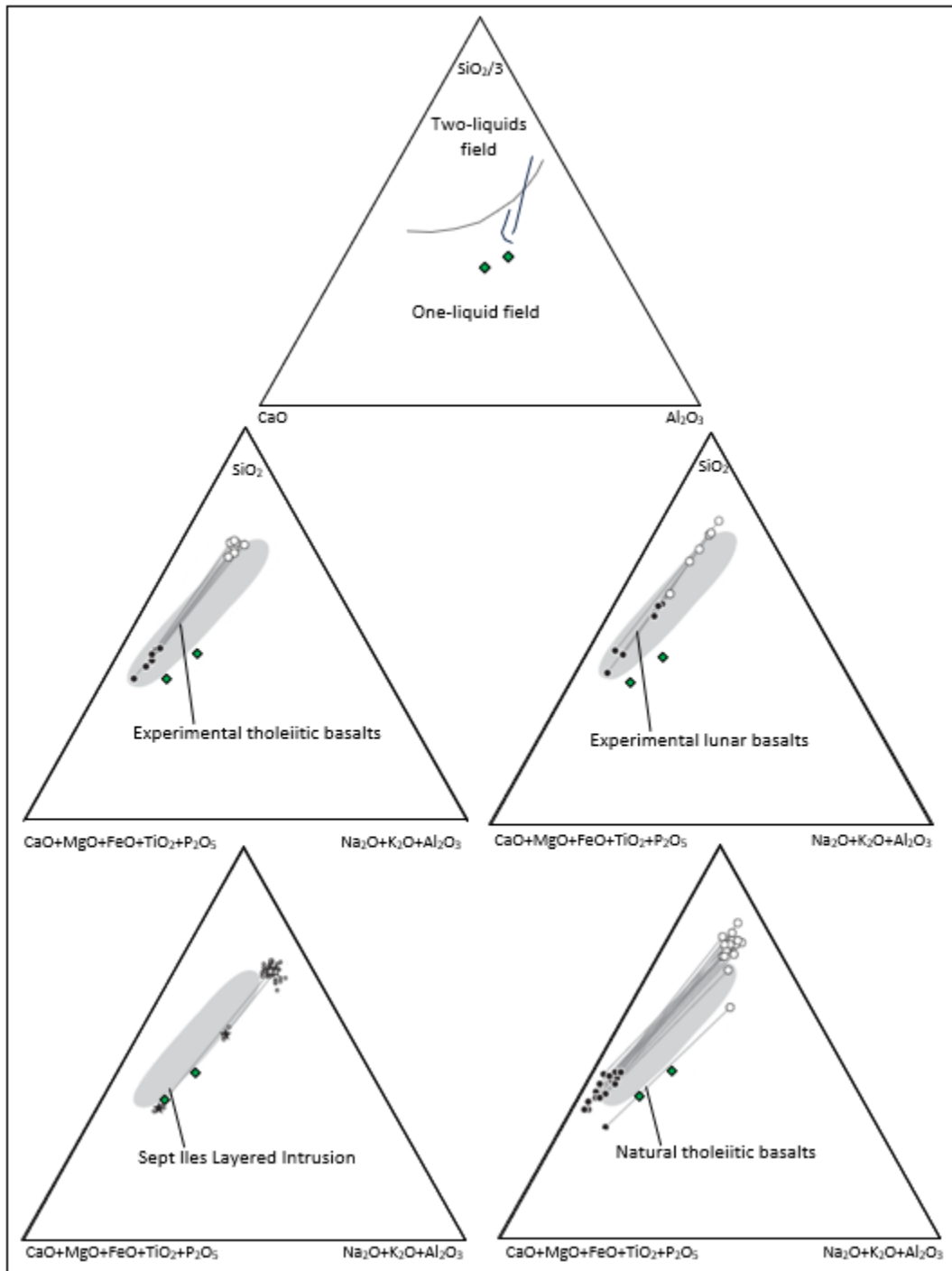
Figure 13. Bulk whole-rock compositions of fine-grained lithologies projected into ternary diagrams for liquid immiscibility evaluation in the Sept Iles Layered Intrusion. A. Composition of the proposed liquid line of descent (after Charlier & Grove, 2012). B-E. Tie lines for various conjugate immiscible melt pairs (after Charlier *et al.* 2011). Grey fields of low-temperature immiscibility field in system leucite-fayalite-SiO2 (Roedder, 1978). B: Immiscible ferrobasalts and granitic liquids obtained from melt inclusion compositions in the Sept Iles layered intrusion (Namur et al. 2010). C: Experimental immiscible pairs in lunar basalts (Longhi, 1990). D: Natural immiscible pairs of glassy globules in tholeiitic basalts (Philpotts,1982). E: Experimental immiscible ferrobasalt and granitic liquids (Dixon and Rutherford, 1979). Grey projection of low-temperature immiscibility field in system leucite-fayalite-SiO2 (Roedder, 1978).